Unveiling the Structure and Reactivity of Rare Earth Oxides and Gold Catalysts Through Density Functional Theory

Dissertation

Zur Erlangung des Doktorgrades der Naturwissenschaften

- Dr. rer. Nat. -

des Fachbereichs 2 (Biologie/Chemie)

vorgelegt von

Shikun Li

Bremen, im Februar 2023

Supervisor: Prof. Dr. Marcus Bäumer

Erstgutachter: Prof. Dr. Tim Neudecker

Zweitgutachterin: Prof. Dr. Lyudmila Moskaleva

Öffentliches Kolloquium am 14.04.2023

Versicherung an Eides Statt

Ich, Shikun Li, Str. Mehlandsdeichweg 1A Bremen, Germany
versichere an Eides Statt durch meine Unterschrift, dass ich die vorstehende Arbeit selbständig und ohne fremde Hilfe angefertigt und alle Stellen, die ich wörtlich dem Sinne nach aus Veröffentlichungen entnommen habe, als solche kenntlich gemacht habe, mich auch keiner anderen als der angegebenen Literatur oder sonstiger Hilfsmittel bedient habe.

Ich versichere an Eides Statt, dass ich die vorgenannten Angaben nach bestem Wissen und Gewissen gemacht habe und dass die Angaben der Wahrheit entsprechen und ich nichts verschwiegen habe.

Die Strafbarkeit einer falschen eidesstattlichen Versicherung ist mir bekannt, namentlich die Strafandrohung gemäß §156 StGB bis zu drei Jahren Freiheitsstrafe oder Geldstrafe bei vorsätzlicher Begehung der Tat bzw. gemäß §161 Abs. 1 StGB bis zu einem Jahr Freiheitsstrafe oder Geldstrafe bei fahrlässiger Begehung.

Bremen, 27.02.2023

_____

Ort, Datum Unterschrift

Acknowledgement

List of Publications

This thesis is based on Papers I, II, and III listed in roman numbers:

[I] **Shikun Li**, Yong Li, Marcus Bäumer, Lyudmila V. Moskaleva, Assessment of PBE+U and HSE06 methods and determination of optimal parameter U for the structural and energetic properties of rare earth oxides. *J. Chem. Phys.* 2020, 153, 164710.

Contribution: I was responsible for designing all theoretical models, carrying out all computations, analyzing data, and contributed significantly to writing the manuscript.

[II] **Shikun Li**, Marcus Bäumer, Lyudmila V. Moskaleva, The impact of electronic structure modification on Lewis acidity-basicity and reducibility of doped La_2O_3. to be submitted.

Contribution: I was responsible for designing all theoretical models, carrying out all computations, analyzing data, and contributed significantly to writing the manuscript.

[III] **Shikun Li**, Okikiola Olaniyan, Lenard L. Carroll, Marcus Bäumer, Lyudmila V. Moskaleva. Catalytic activity of 1D chains of gold oxide on a stepped gold surface from density functional theory. *Phys. Chem. Chem. Phys.* 2022, 24, 28853-28863.

Contribution: I was responsible for designing part of theoretical models, carrying out part of computations, analyzing data, and contributed significantly to writing the manuscript.

Furthermore, I also contributed to the theoretical aspect of other collaborative works, as represented in the following publications, where I was responsible for providing all theoretical interpretation and computation and writing the theoretical part of the manuscript unless otherwise specified:

[IV] Laxman Kankate, Thorben Hamann, **Shikun Li**, Lyudmila V Moskaleva, Armin Gölzhäuser, Andrey Turchanin, and Petra Swiderek, Tracking down the origin of peculiar vibrational spectra of aromatic self-assembled thiolate monolayers. *Phys. Chem. Chem. Phys.*, 2018, 20, 29918-30.

[V] Rongrong Zhao, Zhenchao Zhao, **Shikun Li**, Andrei-Nicolae Parvulescu, Ulrich Müller, and Weiping Zhang, Excellent performances of dealuminated H-Beta zeolites from organotemplate-free synthesis in conversion of biomass-derived 2,5-dimethylfuran to renewable p-xylene. *ChemSusChem*, 2018, 11, 3803-11.

[VI] Zhiquan Lang, Zechao Zhuang, **Shikun Li**, Lixue Xia, Yan Zhao, Yunlong Zhao, Chunhua Han, and Liang Zhou, Mxene surface terminations enable strong metal–support interactions for efficient methanol oxidation on palladium. *ACS Appl. Mater. Interfaces*, 2020, 12, 2400-06.

[VII] Jiexin Zhu, **Shikun Li**, Zechao Zhuang, Shan Gao, Xufeng Hong, Xuelei Pan, Ruohan Yu, Liang Zhou, Lyudmila V. Moskaleva, and Liqiang Mai, Ultrathin metal silicate hydroxide nanosheets with moderate metal–oxygen covalency enables efficient oxygen evolution. *Energy Environ. Mater.*, 2022, 5, 231-237.

[VIII] Yong Li, **Shikun Li**, Marcus Bäumer, Elena A. Ivanova-Shor, and Lyudmila V. Moskaleva, What changes on the inverse catalyst? Insights from CO oxidation on Au-supported ceria nanoparticles using ab initio molecular dynamics. *ACS Catal.*, 2020, 10, 3164-74.

Contribution: I was responsible for the discussion of the results and part of revision.

[IX] Yong Li, **Shikun Li**, Marcus Bäumer, Lyudmila V. Moskaleva, Transient Au–CO complexes promote the activity of an inverse ceria/gold catalyst: an insight from ab initio molecular dynamics. *J. Phys. Chem. C*, 2021, 125(48), 26406-26417.

Contribution: I was responsible for the discussion of the results and part of revision.

[X] Rongrong Zhao, **Shikun Li**, Xunzhen Sun, Lianchao Wu, Qiang Fu, Hongzi Tan, Ming Wang, Hongyou Cui, DFT study of substituent effect on the reaction between furanic compounds and ethylene catalyzed by Brönsted acid. *ChemPhysChem*, 2022, in review.

[XI] Rongrong Zhao, **Shikun Li**, Lixin Bi, Qiang Fu, Hong-Zi Tan, Ming Wang, Hongyou Cui, Enhancement of *p*-xylene selectivity in the reaction between 2,5-

dimethylfuran and ethanol over ammonium fluoride modified ZSM-5 zeolite. *Catal.*

Sci. Technol., 2022, 12, 2248-2256.

Zusammenfassung

Im Bereich der heterogenen Katalyse und der Elektrokatalyse gewinnen Seltenerdoxide (REO) als relativ unerforschte Materialgruppe zunehmend an Aufmerksamkeit, während Goldkatalysatoren im Nanomaßstab ein erhebliches Potenzial für Niedertemperaturanwendungen gezeigt haben. Diese beiden Arten von Katalysatorsystemen können nicht nur separat als aktive Komponenten für die Katalysereaktionen dienen, sondern auch zu einem Metall-Oxid-Hybridsystem kombiniert werden. In Anbetracht der Komplexität gemischter Metall-Oxid-Systeme ist es wichtig, zunächst die Oberflächeneigenschaften und die Reaktivität einzelner Katalysatoren, wie z. B. Seltenerdoxide und nanostrukturiertes Gold, zu untersuchen. Die Dichtefunktionaltheorie (DFT) ermöglicht die Modellierung von REOs und Gold und bietet ein tieferes mikroskopisches Verständnis ihrer katalytischen Eigenschaften. Für die Modellierung ihrer Eigenschaften ist jedoch ein zuverlässiger und universeller Berechnungsansatz erforderlich, insbesondere für REOs, da die Elektronen des f-Orbitals stark korreliert sind und systematische Studien fehlen. Daher bestand der erste Schritt dieser Arbeit darin, die Leistung der derzeit verfügbaren Methoden systematisch zu bewerten, wobei hier PBE+ U und HSE06 zur Beschreibung der Strukturparameter und der energetischen Eigenschaften der ausgewählten hexagonalen Lanthanidsesquioxide und des kubischen Fluorit-Ceriumdioxids verwendet wurden. Es wurden mehrere repräsentative Oberflächen konstruiert, um die Übertragbarkeit des ermittelten optimalen Parameters U für die REOs zu bewerten, um Oberflächeneigenschaften wie die elektronische Struktur und Adsorptionseigenschaften zu simulieren, wobei das PBE+ U-Niveau mit dem hybriden HSE06-Niveau verglichen wurde. Nachdem wir die optimale Methode zur Beschreibung von REOs und Oberflächen bestimmt hatten, wählten wir die $La_2O_3(0001)$-Oberfläche aus, um den Einfluss der ausgewählten s-Block-, d-Block- und f-Block-Heteroatome auf die Lewis-Azidität/Basizität der Oberfläche und die Reduzierbarkeit der Oberfläche durch den Ersatz des Oberflächenmetallatoms durch

die Dotierstoffe zu untersuchen. Schließlich konzentrierten wir uns auf die Goldkatalysatoren und untersuchten die Möglichkeit der Bildung selbstorganisierter Sauerstoffspezies auf der ausgewählten Au(221)-Oberfläche, gefolgt von der Untersuchung der Reaktivität für CO und O_2 auf der Oberfläche. Die wichtigsten Ergebnisse unserer Arbeit lassen sich wie folgt zusammenfassen.

Es hat sich gezeigt, dass das HSE06-Hybridfunktional die Gitterparameter und bestimmte energetische Eigenschaften im Vergleich zu experimentellen Werten genau wiedergibt. Die PBE+ U-Methode kann die Ergebnisse von HSE06 oder experimentelle Werte nur reproduzieren, wenn der U-Parameter aus einem geeigneten Wertebereich ausgewählt wird. Typischerweise müssen die U-Parameterwerte für verschiedene Ln_2O_3 (für Lanthanidensesquioxide) oder CeO_2 angepasst werden, um die verschiedenen Eigenschaften genau zu beschreiben. Die meisten Strukturparameter und Reaktionsenergien von Massenoxiden können durch PBE+ U mit einem relativ kleinen U-Parameter genau beschrieben werden. Zur Simulation der elektronischen Oberflächeneigenschaften von Ln_2O_3 oder CeO_2, wie z. B. der 4*f*-Elektronenlokalisierung, ist jedoch ein größerer U-Wert erforderlich. Für die La_2O_3(0001)-Oberfläche wurde eine deutliche lineare Beziehung zwischen der Oberflächenreduzierbarkeit, gemessen durch die Energie der Sauerstoffleerstellenbildung, und dem Bandzentrum der unbesetzten La5*d*-Zustände oder der besetzten O2*p*-Zustände der La- oder O-Atome an der Oberfläche festgestellt. Es wurde festgestellt, dass die Bildung einer Sauerstoffvakanz die La5*d*- und O2*p*-Bandzentren in Bezug auf den Fermi-Spiegel nach unten verschiebt, was durch *s*-Block- und *d*-Block-Dotierungen (Cu oder Ni) unterschiedlich kompensiert werden kann, aber nicht so sehr durch die hochvalenzen *d*-Block-Dotierungen und *f*-Block-Dotierungen, die La-Atomen chemisch ähnlich sind. Das *d*- oder *p*-Band Zentrum relativ zum Fermi-Niveau ist eher indikativ für die Oberflächenreduzierbarkeit, verglichen mit der Lewis Säure/Basizität gemessen durch Adsorptionsenergien von Molekülen mit Lewis basischen/sauren Eigenschaften. Die Lewis-Säure der

Oberflächen La-Atome ändert sich beim Dotieren nicht signifikant, aber die Lewis-Basizität der O-Atome variiert leicht.

In einer Studie über die Rolle der selbstorganisierten Sauerstoffstruktur auf der Oberfläche von Goldkatalysatoren haben wir eine doppelte Sauerstoff(O)-Kette entlang der Stufenkante auf der Au(221)-Oberfläche konstruiert, mit oder ohne Sauerstoffleerstellen, die sich unter praktischen katalytischen Bedingungen auf goldbasierten Katalysatoren bilden können. Begleitet von einer erhöhten Adsorptionskraft von CO und O_2 an der Sauerstoffkette mit Leerstellen, werden CO und O_2 auch stärker aktiviert. Die Dissoziation von O_2 hat eine um den Faktor zwei niedrigere Aktivierungsenergie im Vergleich zur normalen Au(221)-Oberfläche. Wir haben zwei Arten von Mechanismen für die CO-Oxidation in Betracht gezogen: dissoziative und assoziative. Beide Mechanismen können auf der O-Kette mit zwei benachbarten Leerstellen konkurrieren, je nach den gegebenen thermodynamischen Bedingungen, wenn CO und O_2 gemeinsam an der Kette oder der Stufenkante auf der Au(221)-Oberfläche adsorbieren. Ein günstigerer Weg kann gefunden werden, wenn der anfängliche Co-Adsorptionszustand von CO an einer Terrassenstelle und O_2 an einer leeren Stelle adsorbiert wird.

Abstract

In the field of heterogeneous catalysis and electrocatalysis, rare earth oxides (REOs) are increasingly gaining attention as a relatively unexplored group of materials, while nanoscale gold catalysts have demonstrated significant potential in low-temperature applications. These two kinds of catalyst systems can not only act as the active components for the catalysis reactions separately, but can also be combined into one metal-oxide hybridized system. Considering the complexity of mixed metal-oxide systems, it is essential to first study the surface properties and reactivity of individual components, such as rare earth oxides and nanostructured gold. Density functional theory (DFT) enables the modelling of REOs and gold, and provides a deeper microscopic understanding of their catalytic properties. However, a reliable and universal computational approach is required for modelling their properties, particularly REOs due to the strong correlation of the *f*-orbital electrons and the lack of systematic studies. Therefore, the first step of this work was to systematically assess the performance of the currently-available methods, here applying PBE+U and HSE06 in describing the structural parameters and energetic properties of the selected hexagonal lanthanide sesquioxides and the cubic fluorite-type cerium dioxide. Several representative surfaces were constructed to evaluate the transferability of the obtained optimal parameter U for bulk REOs to simulate surface properties, such as the electronic structure and adsorption properties, comparing the PBE+U level to the hybrid HSE06 level. After determining the optimal method for describing bulk REOs and surfaces, we further selected the $La_2O_3(0001)$ surface to investigate the influence of the selected *s*-block, *d*-block and *f*-block heteroatoms on the surface Lewis acidity/basicity and surface reducibility through replacing the surface La atom by the dopants. Finally, we focused on the gold catalysts and elucidated the possibility of self-organized oxygen species formed on the selected Au(221) surface, followed by the investigation of the reactivity for CO and O_2 on the surface. The main results of our work can be summarized as follows.

The HSE06 hybrid functional has been found to accurately reproduce lattice parameters and certain energetic properties compared to experimental values. The PBE+U method can only reproduce the results of HSE06 or experimental values if the U parameter is selected from an appropriate range of values. Typically, the U parameter values must be adjusted for different Ln_2O_3 (denoting lanthanide sesquioxides) or CeO_2 to accurately describe different properties. Most bulk oxide structural parameters and reaction energies can be accurately described by PBE+U with a relatively small U parameter. However, a larger U value is needed to simulate surface electronic properties of Ln_2O_3 or CeO_2, such as $4f$ electron localization. For the $La_2O_3(0001)$ surface, a distinct linear relationship was found between the surface reducibility, as measured by oxygen vacancy formation energy and the band center of the unoccupied $La5d$ states or the occupied $O2p$ states of the surface La or O atoms. It was noted that the formation of an oxygen vacancy shifts the $La5d$ and $O2p$ band centers downwards with respect to the Fermi level, which can be offset to various degrees by low-valence s-block and d-block dopants (Cu or Ni), but not so much by the high-valence d-block dopants and f-block dopants chemically similar to La atoms. The d- or p-band center relative to the Fermi level is more indicative of the surface reducibility, compared to the Lewis acidity/basicity measured by adsorption energies of molecules with Lewis basic/acidic properties. The Lewis acidity of the surface La atoms does not change significantly upon doping, yet the Lewis basicity of O atoms varies slightly.

In a study of the role of self-organized surface oxygen structures for gold catalysts, we constructed a double oxygen (O) chain along the step edge on the Au(221) surface, with or without oxygen vacancies that may form on gold-based catalysts under practical catalytic conditions. Accompanied by an increased adsorption strength of CO and O_2 on the oxygen chain with vacancies, CO and O_2 also become more activated. The dissociation of O_2 has a factor of two lower activation energy compared to the regular Au(221) surface. We considered two types of mechanisms for CO oxidation: dissociative and associative. Both mechanisms may compete on the O chain with two

adjacent vacancies depending on the given thermodynamic conditions when CO and O_2 co-adsorb on the chain or the step edge on the Au(221) surface. A more favorable pathway can be found with the initial co-adsorption state of CO at a terrace site and O_2 adsorbed at a vacancy site.

Table of Contents

List of Symbols and Abbreviations

AIMD	*ab initio* molecular dynamics
C2	Ethane and ethylene
CBM	Conduction band minimum
CCSD(T)	Coupled cluster single-double-triple
DFT	Density functional theory
DMFT	Dynamical mean-field theory
GGA	Generalized gradient approximation
HF	Hartree-Fock method
HSE	Heyd–Scuseria–Ernzerhof hybrid functional
ICOHP	Integrated crystal orbital Hamilton population
IGM	Independent gradient model
LDA	Local-density approximations
Ln_2O_3/LnF_3	Lanthanide sesquioxide/fluoride
MvK	Mars-van Krevelen mechanism
OCM	Oxidative coupling of methane
OER	Oxygen evolution reaction
ORR	Oxygen reduction reaction
PAW	Projector augmented wave
PBE	Perdew-Burke-Ernzerhof functional
*p*DOS	Partial density of states
REOs	Rare earth oxides
STM	Scanning tunneling microscopy
TPD	Temperature-programmed desorption
VBM	Valence band maximum

Chapter 1 Introduction

1.1 The Performance of PBE+ U and HSE06 Methods on the Structural and Energetic Properties of Bulks or Surfaces of Rare Earth Oxides

Rare earth metal oxides (REOs) have been widely employed as effective luminescent materials, ceramics, magnets, conductors as well as catalysts for many reactions, such as low-temperature carbon monoxide oxidation[1-3], carbon dioxide methanation[4], and oxidative coupling of methane (OCM)[5-9]. As an example, a statistical analysis of a database of previously studied catalytic results revealed that lanthanum oxides doped with Na or alkaline earth metals (Sr, Mg, Ba) were highly active for the OCM reaction.[10] Furthermore, the yield of C2 (ethane and ethylene) from methane conversion was up to 10-12% with undoped La_2O_3, Sm_2O_3 and Nd_2O_3. The yield was further increased to 22% when Li alkali metal was added to Sm_2O_3.[11-12]

At present, DFT provides a valuable tool for understanding the catalytic properties of REOs and gold. Further studies are necessary to gain deeper insight into the properties of these catalysts, which can guide the design of more effective catalysts for specific reactions, with a focus on lanthanum or cerium oxides. For La_2O_3, a series of surface properties including active sites, oxygen vacancy formation and hydrogen abstraction from methane, have been modelled using DFT methods.[13-15] CeO_2, a well-known catalyst, has been theoretically studied in regards to oxygen vacancy formation and methane activation on the surfaces doped by Pd[16-18] or Fe/Co/Ni[19] at the DFT level.

However, conventional functionals, such as LDA and GGA, applied in DFT calculations, suffer from a failure to accurately describe the localization property of $4f$ electrons in REOs, where the spurious self-interactions among the strongly correlated $4f$ electrons become significant due to the electron localization.[20] In order to eliminate or reduce the self-interaction error, a series of advanced DFT-based methods have been

considered, such as GW[21-22], dynamical mean-field theory (DMFT)[23-24], DFT+U using an LDA or GGA functional[25] and DFT with a hybrid functional[26].

DFT methods combining a hybrid functional and a plane-wave basis set are usually computationally expensive, but effective enough to describe the electronic structures of strongly correlated systems.[27] The improvement of hybrid functionals on the simulation of electron localization results from the inclusion of a fraction of HF exact exchange in these functionals. Depending on the fraction of HF exact exchange included, hybrid functionals are divided into various types, including B3LYP and wB97XD functionals, extensively applied in cluster models,[28] and HSE and PBE0 functionals, which are mainly used for periodic systems. For Ce_2O_3 and CeO_2, several functionals, PBE, M06L and HSE06, have been assessed with respect to their lattice parameters, vibrational properties, band gaps, and reaction energies. Here, the HSE06 hybrid functional gave better results for vibrational properties, band gaps and surface oxygen vacancy formation energy, while PBE and M06L provided better predictions for the reduction energies of CeO_2 to Ce_2O_3.[29] The HSE hybrid functional was also successful in correctly predicting the lattice constant and the localization of a single $4f$ electron of Ce_2O_3.[30]

Different from hybrid functionals, LDA and GGA functionals, under the premise of the inclusion of the parameter of U-J (i.e. DFT+U), provide computationally cheaper but less accurate results for the simulation of periodic systems including d- or f-block elements.[25] For DFT+U, a simple Hubbard model was used in most of the calculations of REOs, wherein an additional on-site Coulomb interaction term U and site exchange term J are exerted on the on-site two-electron integrals. The two independent parameters, U and J, were further simplified by replacing them with their difference, U-J, as addressed by Dudarev et al.[31] Because J is usually set to zero, we simply represent U-J by U in this thesis.

The DFT+U method can achieve similar accuracy to hybrid functionals by adjusting the U parameter to match experimental or theoretical values. It is more empirical than

the HSE hybrid functional, but can still provide accurate results for *4f* electron localization,[32-33] or description of polarons with an optimal U parameter.[34] For CeO_2 and Ce_2O_3, the geometric, electronic, and thermochemical properties have been calculated and compared to experimental values at the LDA/GGA+U level with various U values.[35-40] Furthermore, a study of the performance of DFT+U on CeO_2 and other transition metal oxides has shown that for MO_x (where M corresponds to Ti, Co, Ni, Mo, Mn), the parameter U has a significant effect on the results generated by the DFT+U method, which empirically depends on the fitted property or the chosen reference values.[41]

For the series of lanthanide oxides, the determination of optimal U values was only studied on CeO_2 and Ce_2O_3 at the DFT+U level. Fabris et al.[42] determined the U values for the LDA or GGA functionals as 5.3 eV or 4.5 eV, respectively using the linear-response approach of Cococcioni and de Gironcoli[43]. The latter value (U = 4.5 eV) has been adopted in the most recent DFT+U calculations[18,44-46] of systems including cerium. When comparing the results of hybrid functionals (HSE and PBE0), GGA+U, and LDA+U, a lower U value of 2 eV was obtained with respect to the lattice parameters, electronic structure and thermodynamic energies of CeO_2 compared to the value obtained by the linear-response method.[30]

1.2 The Surface Lewis Acidity/Basicity and Reducibility of Irreducible La₂O₃(0001) Surfaces Doped by Various Heteroatoms

Typically, reactions facilitated by REOs take place on the surface of oxides in heterogeneous catalysis. Dopants have been found to be effective in modifying the surface reactivity, often increasing its catalytic activity. Previous studies have demonstrated that La_2O_3 modified by various metal heteroatoms can be used in methane chlorination[44], dry reforming of methane[45-46], and oxidative coupling of methane[47-48].

From a statistical analysis of a database covering the previously obtained results, Baerns et al.[10] found that substituting the surfaces with s-block metals (Na, Sr, Cs, Ba) or Mn, W dopants could lead to an increase in C2 (ethane and ethylene) selectivity of the OCM reaction, while also promoting the catalytic activity on the doped surfaces.

As discussed above, substituting surface atoms with heteroatoms can significantly influence on the M-O bond chemistry (where M denotes a heteroatom) and the electron distribution around the doping site. This doping of the surfaces activates the surface oxygen atoms and increases the ease of oxygen vacancy formation, which is reflected in the energy of the oxygen vacancy formation, also known as the surface reducibility. This is especially important in catalytic oxidation reactions, following the Mars-van Krevelen (MvK) mechanism, such as low-temperature CO oxidation, oxygen evolution/reduction reaction (OER/ORR).[49-53] Metiu et al.[14] demonstrated that La_2O_3(001) and (011) surfaces doped by Cu, Zn, Mg, Fe and Al form oxygen vacancies much more easily.

The introduction of heteroatoms to the oxide surface can have a profound effect on the electronic structure of the surface. It can cause the formation of localized states in the surface that can significantly modify the electronic structure. These localized states can be either donor or acceptor states and can lead to changes in the bandgap, the number of conduction and valence bands, and the density of states. The localized states can also lead to a shift in the Fermi level of the surface, which can have a significant effect on the electrical and optical properties of the material. Doping can significantly change the ability of surface atoms to accept or donate electron pairs, which is related to their Lewis acidity/basicity and plays an essential role in catalytic reactions. Rane et al.[54] showed that the acidity of REOs has a considerable effect on the selectivity of methane conversion reactions due to the formation of CH_3 radicals by the dissociation of methane, which too strongly adsorb on the surface, leading to the combustion of CH_3 radicals. The TPD of CO_2 experiments further demonstrated a correlation between the surface basicity and OCM reactivity for La_2O_3, Nd_2O_3, ZrO_2 and Nb_2O_5.[55-56] Sun et al.[57]

4

established a linear relationship between the CH_4 activation barrier and the Lewis acidity of the surface La atoms measured by the binding energies of F^- and the Brönsted basicity of the surface O atoms weighed by the binding energies of protons on the lanthanum sesquioxide surface. Additionally, the La_xO_y clusters were also investigated to evaluate the effect of CO_2 adsorbates on methane activation using DFT and CCSD(T). It was established that the CO_3^{2-} species formed by the CO_2 adsorption suppresses the methane activation and then decomposes at temperatures beyond 500 K, promoting the activity of methane oxidative coupling.[58]

Research by Metiu et al.[59-62] has demonstrated that the Lewis acidic and Lewis basic sites of lanthanum sesquioxide surfaces can induce the "attractive" interaction of Lewis acid-base pairs, which can lead to the dissociation of Br_2 and HBr and the co-adsorption of two Br atoms or one Br and one H atom onto Mg/Cr-doped $La_2O_3(001)$ surfaces.[62] It has also been shown that the dissociative adsorption of H_2 on $La_2O_3(001)$ surfaces is driven by the formation of Lewis acid-base pairs, whereby the two formed H atoms are likely to form a hydroxyl and a hydride pair on the polaron site.[59] Additionally, the dissociative adsorption of methane onto $La_2O_3(001)$ surfaces is also enabled by the formation of a Lewis acid-base pair.[60]

1.3 CO Oxidation and O_2 Dissociation on the –(Au-O)- Chain Structure on Au(221) Surface

In addition to the aforementioned individual REOs, hierarchical catalyst systems are commonly employed to attain higher activity, selectivity, and stability in heterogeneous catalysis. Two examples of extensively studied catalysts in this regard are cerium-supported gold nanoparticles[63-65] and gold-supported cerium oxide.[66-67] Previously, we constructed cerium clusters ($Ce_{10}O_{20/19}$) supported on the Au(321) surface, which were found to be highly stable according to AIMD simulations. Additionally, the presence of steps and kinks on the gold surface resulted in a low activation energy for the CO oxidation reaction.[66] The surface properties and activity of REOs have been discussed

in previous sections. Investigating the surface properties and activity of gold catalysts is also very important as they have been shown to exhibit relatively high activity and selectivity in many heterogeneous catalysis reactions, such as the oxidative coupling or electro-oxidation of alcohols,[68-70] the water-gas-shift reaction,[71-72] and the low-temperature oxidation of carbon monoxide.[73-75]

As discussed in previous sections, oxygen vacancies on rare earth oxide surfaces play essential role in catalytic reactions, especially those that follow the Mars-van Krevelen (MvK) mechanism. Oxygen vacancies also have a strong influence on surface geometries, Lewis acidity or basicity, and the strength of molecular adsorption. In contrast to REOs, gold catalysts do not contain oxygen atoms, so the formation of oxygen vacancies is not possible. In particular, low-index gold surfaces, such as Au(110)[76] and Au(111),[77] have been found to be resistant to chemisorption or dissociative adsorption of O_2 molecules. Molecular oxygen only weakly adsorbs on the Au(211) and stretched Au(111) surfaces.[77] However, it has been found that O_2 chemisorbs on even-sized subnanometric gold clusters in two forms, superoxo (O_2^-) and peroxo (O_2^{2-}), with electron transfer from the gold cluster to O_2.[78] Previous theoretical studies have also suggested that O_2 is likely to adsorb and dissociate on stepped and kinked Au surfaces due to the presence of unsaturated Au atoms on the steps, in comparison to the flat Au(111) surface.[77, 79-81]

When O_2 dissociates on a stepped gold surface, electron-rich O atoms will preferably occupy either two-fold coordination sites on the step edge or three-fold fcc sites adjacent to it.[82] Therefore, as the number of adsorbed surface O atoms increases, a one- or two-dimensional chain structure may form along or across the step edges of the surface.[22, 26-29] Sun et al.[83] explored the formation of a linear O-Au-O structure on different gold surfaces using Hückel theory, which was found to stabilize the adsorption of atomic oxygen. This was further substantiated by DFT calculations. Furthermore, our previous ab initio molecular dynamics (AIMD) simulations showed that a continuous –(Au-O)- chain structure formed on the step of the Au(321) surface.[84] A

6

quasi-ordered oxygen chain was characterized on an Au(110) surface at low coverage of oxygen atoms using scanning tunneling microscopy (STM) and DFT modelling.[85] The stability of an oxygen chain structure on a gold surface was also verified under specific temperature and pressure conditions.[28-29, 32-33] By investigating the possibility of forming oxygen chain structures with or without vacancies on the gold surfaces allows us to examine possible involvement if such structures in catalyzed oxidation reactions.

In many oxidation reactions catalyzed by gold catalysts, low-temperature CO oxidation has gathered significant interest. Haruta et al.[86-87] made the first attempt to prepare gold particles with a markedly enhanced catalytic activity using the coprecipitation method. The reaction activity and mechanism of CO oxidation on gold surfaces without oxygen chain structures have been extensively studied experimentally and theoretically.[88-91] Hu et al[90] suggested a two-step mechanism where CO initially reacts with O_2 to form a CO_2 molecule, and the remaining atomic O binds quickly to the CO to form CO_2. Fajín et al.[91] showed that the direct binding of CO and O_2 forms the four-atom compound OCOO as a preferred reaction pathway for CO oxidation on the Au(321) surface, with the participation of atomic O from the predissociated O_2. Another possible pathway is O_2 dissociation on the gold surface without binding to CO, followed by a direct reaction of atomic O with the CO to form CO_2.

When oxygen atoms form a chain on gold surfaces, an increase in the activity of CO oxidation is anticipated. Additionally, pre-adsorbed O atoms have been shown to facilitate the adsorption of subsequent O_2 molecules.[29, 34-35] Friend et al.[92] corroborated an increased probability of O_2 dissociation on the Au(111) surface pre-covered with atomic oxygen by means of temperature programmed desorption (TPD), using electron bombardment of condensed NO_2. A DFT study revealed that an Au(111) surface covered with oxygen adsorbs CO more strongly than a pristine Au(111) surface, although the CO adsorption strengths decreases with increasing oxygen coverage.[93] Therefore, it is likely that oxygen chain structures formed on the steps of the gold

surfaces in an oxygen-rich environment can facilitate the adsorption of O_2 and CO, thus enhancing the reactvity of CO oxidation.

1.4 Aims of this Dissertation

To understand the hierarchical catalyst system of lanthanide oxides and gold, it is necessary to study their structure, surface properties, and reactivity. Understanding REOs and gold allows us to investigate their synergetic effect in mixed REOs/Au system. Theoretical studies on REOs other than La_2O_3 and CeO_2 are scarce due to difficulty in dealing with *f* orbitals. Consequently, the first part of this work, summarized in Chapter 2&3, is to evaluate the applicability of the currently available approaches, such as DFT+U and HSE functionals applied in the plane-wave calculations in terms of describing material properties of interest of bulk REOs and surfaces.

After determining the proper method in simulating bulk REOs and surfaces, a systematic study was conducted in order to investigate the effect of a series of doping heteroatoms including *s*-block, *d*-block and *f*-block elements in the periodic table on the surface reducibility and surface acidity/basicity of the selected REO surfaces. A relationship between surface reducibility and acidity/basicity is needed to create a universal descriptor of surface properties.

Considering the reactive O species on a stepped gold surface and the possibility of one- or two-dimensional oxygen chains along the step edge, we focus on the formation of oxygen chains and their reactivity on the specific stepped Au(221) surface in the last part of this dissertation. Although O atoms in a chain may be less reactive than individual O atoms due to thermodynamical preference of fully saturated O chains, incomplete chains with vacancies can act as active sites for the adsorption and activation of O_2 in real catalytic systems. In this part of the study, we will first analyze the stability of oxygen chains on a Au(221) surface and the formation of oxygen vacancies in the chains. After determining the most favorable arrangement of vacancies

in the O chains, we will investigate the adsorption and activation of O_2 and CO, as well as the possible reaction pathways of CO oxidation facilitated by O chains.

Chapter 2 Assessment of DFT+U and HSE06 for the Bulk Rare Earth Oxides

As discussed in Chapter 1, the HSE hybrid functional usually gives more accurate results compared to DFT+U using LDA or GGA functionals, but at the expense of increased computational cost.[27, 29-30] The parameter U used in DFT+U is also empirical and depends on the calculated properties and the reference values.[35-41] Therefore, it is crucial to determine the optimal range of U values in relation to our desired properties of interest based on consistent reference values. Furthermore, most of REOs lack theoretical studies, with the exception of La_2O_3 and CeO_2. Hence, in Chapter 2, we assess the performance of DFT+U and HSE functionals on the material properties of interest of all REOs and obtain a set of optimal values of the parameter U for consistency in subsequent studies of REOs. Specifically, we focus on structural parameters and thermodynamic properties, such as formation energies of bulk REOs.

2.1 Equilibrium Lattice Parameter

For most of the lanthanide oxides, the most common structure is the sesquioxide type (Ln_2O_3, where Ln stands for any lanthanide element), with the trivalent oxidation state. The exception is cerium oxide, in which cerium is found in the tetravalent oxidation state in the form of a stoichiometric dioxide (CeO_2). Therefore, we have chosen to focus our investigation on sesquioxides, as this allows for a consistent comparison of REOs. Three different polymorphic forms exist for the sesquioxides studied, namely hexagonal (A-type), monoclinic (B-type) and cubic (C-type).[94] The geometric, electronic and thermodynamic properties of the bulk sesquioxides were calculated for the A-type polymorphs using the PBE+U and HSE methods. The crystal structures of the sesquioxides Ln_2O_3 and dioxide CeO_2 are shown in Figure 2.1. Additionally, we also considered LnF_3 with respect to the reference reaction discussed in section 2.2. The trifluorides of Sm, Eu, Ho and Tm adopt hexagonal LaF_3-type structures, but the

orthorhombic YF_3 crystals are isostructural with the majority of the LnF_3 (Ln: from Sm to Lu) crystals.[95-96] To ensure consistency, the YF_3-type structure was thus adopted for all LnF_3 (see Figure 2.1(c)).
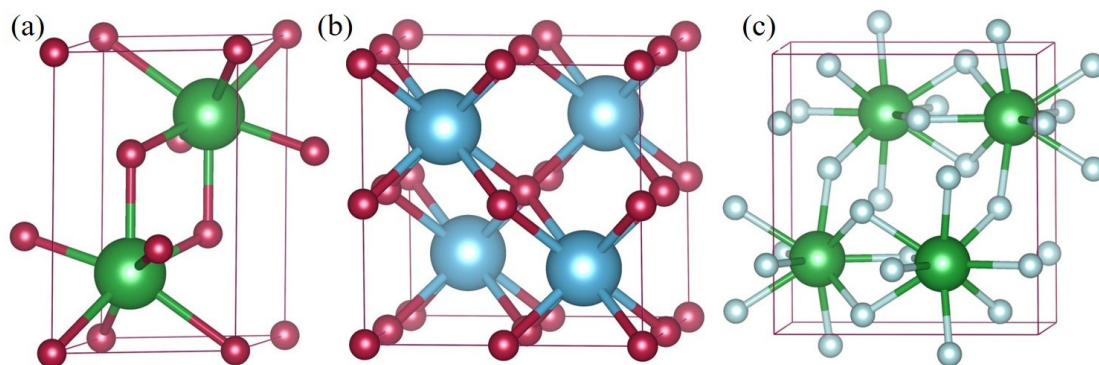
Figure 2.1. The crystal structures of (a) A-type Ln_2O_3, (b) fluorite-type CeO_2 and (c) YF_3-type LnF_3. Oxygen atoms are shown in dark red, cerium atoms in light blue, fluorine atoms in light green, and lanthanide atoms in dark green.

2.1.1 A-type Ln_2O_3

The initial lattice parameters of the A-type Ln_2O_3 were obtained from the optimization results of the PBE method by Bo Wu et al.[97] The equilibrium volumes of A-type Ln_2O_3 optimized by the HSE06 method show a decreasing trend with increasing atomic number, similar to the results obtained with the PW91[98] or PBE[97] functional using PAW pseudopotentials and with f-electrons treated as core electrons. Such "large-core" pseudopotentials mimic the so-called "lanthanide contraction".

The HSE06 method also provides accurate structural parameters when compared to the available experimental data. The theoretically predicted lattice parameters by the HSE06 method are smaller than the experimental values of La_2O_3 ($a_0 = 3.94$ Å, $c_0 = 6.14$ Å)[99] and Nd_2O_3 ($a_0 = 3.83$ Å, $c_0 = 5.99$ Å)[100] with an error less than 0.03 Å. Besides, the a_0, c_0, and the equilibrium unit cell volume of Pr_2O_3 are also underestimated by 1.0 %, 0.2 %, and 1.7 %, respectively, compared to the experimental values[101], 3.86 Å, 6.01 Å, 77.54 Å^3. The structural parameters of hexagonal Ce_2O_3 are calculated to be 3.86 and 6.09 Å for a_0 and c_0 respectively, consistent with the results reported by Hay

et al.[102] and Silva et al.[30] The HSE06 functional only slightly underestimates the lattice parameter a_0 by 0.8 % (0.03 Å) and slightly overestimates the c_0 parameter by 0.03 Å compared to the experimental a_0 (3.89 Å) and c_0 (6.06 Å).[103-104]
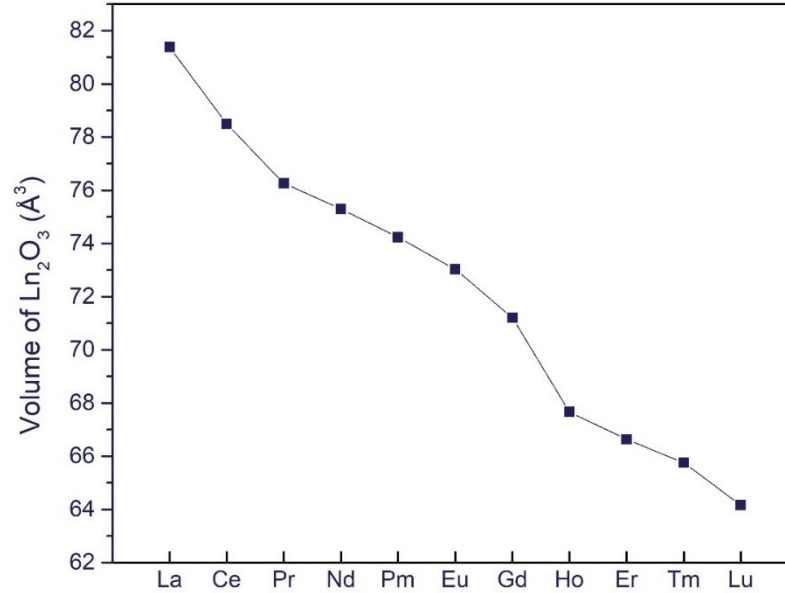
Figure 2.2. Equilibrium volumes of A-type Ln_2O_3 (Ln = La, Ce, Pr, Nd, Pm, Eu, Gd, Ho, Er, Tm, Lu) calculated with the HSE06 method.

When the PBE+U method is applied, the equilibrium lattice parameters a_0, c_0 and the volumes are found to increase with the U value for La_2O_3, Ce_2O_3, Pr_2O_3, Nd_2O_3, Pm_2O_3 and Sm_2O_3. However, this trend changes for the late Ln_2O_3 from Eu_2O_3 to Lu_2O_3, for which the variation of the crystal volumes becomes small with the increasing U parameter and from Gd_2O_3 onwards even inverse trend is found, where lattice parameters and volumes start to decrease with U, although the dependence on the U value remains small. This behaviour mainly results from the competing effects of two factors, the on-site Coulomb repulsion and shielding of valence electrons (Lanthanide contraction), of which the increased former one could reduce electron delocalization which tends to increase the lattice parameter, whereas the latter one becomes more

Table 2.1. Equilibrium lattice parameters a_0 (in Å), c_0 (in Å) and volume (in Å^3) of Ln$_2$O$_3$ (Ln = La, Ce, Pr, Nd, Pm, Sm, Eu, Gd, Ho, Er, Tm, Lu) calculated at the PBE, PBE+U (U = 1-8 eV) and HSE06 level.

REOs	Lattice parameter	PBE	PBE+U								HSE06
			U=1	U=2	U=3	U=4	U=5	U=6	U=7	U=8	
La$_2$O$_3$	a_0	3.94	3.95	3.95	3.96	3.97	3.97	3.98	3.99	3.99	3.91
	c_0	6.18	6.18	6.20	6.21	6.22	6.22	6.23	6.24	6.25	6.14
	Volume	83.02	83.36	83.86	84.28	84.82	85.16	85.57	85.93	86.30	81.38
Ce$_2$O$_3$	a_0	3.83	3.89	3.90	3.91	3.92	3.92	3.93	3.94	3.94	3.86
	c_0	6.08	6.12	6.15	6.16	6.17	6.18	6.19	6.19	6.23	6.09
	Volume	77.17	80.05	80.85	81.46	81.96	82.39	82.81	83.24	83.74	78.49
Pr$_2$O$_3$	a_0	3.84	3.86	3.87	3.88	3.89	3.90	3.89	3.90	3.90	3.82
	c_0	6.02	6.03	6.05	6.06	6.08	6.09	6.11	6.12	6.13	6.00
	Volume	77.52	77.64	78.31	78.91	79.45	79.86	80.24	80.58	80.91	76.26
Nd$_2$O$_3$	a_0	3.80	3.83	3.84	3.84	3.85	3.86	3.86	3.87	3.87	3.80
	c_0	6.03	6.05	6.07	6.08	6.10	6.09	6.11	6.11	6.11	6.02
	Volume	75.53	76.72	77.29	77.80	78.25	78.49	78.83	79.16	79.46	75.30
Pm$_2$O$_3$	a_0	3.78	3.82	3.83	3.83	3.84	3.84	3.84	3.85	3.85	3.79
	c_0	5.96	6.01	6.00	6.01	6.03	6.05	6.05	6.05	6.06	5.97
	Volume	73.81	75.94	76.11	76.45	76.81	77.34	77.40	77.56	77.76	74.23
Sm$_2$O$_3$	a_0	3.77	3.78	3.79	3.79	3.80	3.80	3.81	3.81	3.80	-
	c_0	5.95	5.96	5.98	5.97	5.99	6.01	6.01	6.02	6.01	-
	Volume	73.29	74.30	74.73	74.85	75.15	75.28	75.46	75.74	75.50	-
Eu$_2$O$_3$	a_0	3.79	3.81	3.81	3.81	3.81	3.80	3.80	3.79	3.78	3.78
	c_0	5.97	5.93	5.93	5.92	5.95	5.94	5.98	6.03	6.02	5.90
	Volume	74.37	74.58	74.69	74.46	74.73	74.51	74.69	75.08	74.18	73.03
Gd$_2$O$_3$	a_0	3.74	3.75	3.75	3.75	3.74	3.74	3.74	3.73	3.72	3.72
	c_0	5.96	5.96	5.96	5.96	5.96	5.96	5.96	5.94	5.93	5.93
	Volume	72.34	72.51	72.51	72.46	72.17	72.17	72.17	71.64	71.13	71.20
Ho$_2$O$_3$	a_0	3.67	3.67	3.67	3.68	3.68	3.64	3.60	3.50	-	3.67
	c_0	5.89	5.88	5.88	5.84	5.84	5.82	5.79	5.77	-	5.86
	Volume	68.41	68.25	68.32	67.54	67.55	66.23	64.85	61.09	-	67.66
Er$_2$O$_3$	a_0	3.66	3.67	3.66	3.66	3.65	3.65	3.64	3.64	3.63	3.64
	c_0	5.84	5.84	5.84	5.83	5.83	5.82	5.82	5.82	5.82	5.81
	Volume	67.79	67.89	67.77	67.59	67.32	67.18	66.94	66.77	66.48	66.63
Tm$_2$O$_3$	a_0	3.66	3.67	3.66	3.65	3.64	3.62	3.59	3.57	3.55	3.62
	c_0	5.78	5.82	5.82	5.82	5.81	5.79	5.79	5.76	5.72	5.82
	Volume	66.50	66.79	66.60	66.15	65.71	64.89	64.11	63.20	62.20	65.75
Lu$_2$O$_3$	a_0	3.61	3.60	3.58	3.56	3.55	3.53	3.50	3.47	3.43	3.59
	c_0	5.83	5.82	5.78	5.77	5.76	5.73	5.70	5.67	5.62	5.75
	Volume	65.56	65.03	64.24	63.39	62.63	61.58	60.35	59.10	57.22	64.16

pronounced as the atomic number increases from early to late lanthanides as well as the $4f$ states become more localized with increasing U. In addition to these two effects, also the degree of covalency of the Ln-O bond changes slightly with increasing U, as illustrated by the COHP analysis in section 2.1.3.

For the first half of the Ln series from La to Eu, and for Lu, the best agreement with the PBE+U method was achieved using U values of 1-3 eV. For Ce_2O_3, the calculated value of a_0 at U = 1 eV, 3.89 Å, agrees quantitatively with the experimental value, while the calculated volume at U = 1 eV is overestimated by 1.9 % compared to the HSE result. The overestimation increases with increasing U reaching 6.7 % for U = 8 eV. Similarly, good results are achieved for the lattice parameters of La_2O_3, Pr_2O_3 and Nd_2O_3 using the PBE+U functional with U = 1 eV, which are closer to the experimental values than those obtained with the HSE06 functional. In other words, PBE+U with U = 1-3 eV allowed for achieving similar accuracy to that of the HSE06 method for the lattice parameters of La, Ce, Pr, and Nd sesquioxides. In contrast, a much higher U value, U = 7-8 eV, is required for the PBE+U method to achieve the best agreement between the PBE+U and HSE06 lattice parameters for Eu_2O_3, Gd_2O_3 and Er_2O_3, although the U value of 3 eV only overestimates the lattice volumes by less than 2.0 %. The calculated lattice parameters of Ho_2O_3 and Tm_2O_3 at U = 3-4 eV are very close to the HSE06 results, whereas the cell volumes deviate by 0.2 % and 0.6 %, respectively from the HSE06 benchmark. Therefore, we conclude that it should be safe to use the U value around 3 eV to obtain reasonable equilibrium lattice parameters for the lanthanide sesquioxides with the PBE+U method.

2.1.2 YF$_3$-type LnF$_3$

Similar to A-type Ln_2O_3, the decreasing trend of the equilibrium volumes optimized at the HSE06 level across the Ln series as their atomic number increases is also observed for YF$_3$-type LnF$_3$, namely the "lanthanide contraction". Compared to the available experimental crystal volumes of EuF_3 (204.3 Å^3), GdF_3 (201.6 Å^3) and HoF_3 (192.8 Å),

the lattice volumes of EuF_3 (205.05 Å^3), GdF_3 (203.63 Å^3) and HoF_3 (194.84 Å^3) are respectively predicted to be 205.05 Å^3, 203.63 Å^3, 194.84 Å^3 by the HSE06 method, showing a high accuracy of the latter.[96] The HSE06 functional predicts somewhat overestimated cell volumes for the fluorides of late Lanthanides ErF_3, TmF_3 and LuF_3[96] compared to experimental values, but the deviation is less than 5%. Interestingly, we found that the volumes of LnF_3 predicted by pure PBE and PBE+U methods are close to each other as shown in Table 2.2, i.e., the parameter U of the PBE+U method has little effect on the volumes of LnF_3. Generally, the PBE functional typically overestimates lattice volumes of LnF_3 with the error of around 3% compared to the HSE06 functional.

Table 2.2. The equilibrium volume (Å^3) of LnF_3 (Ln = La, Ce, Pr, Nd, Pm, Sm, Eu, Gd, Ho, Er, Tm, Lu) calculated at the PBE and PBE+U (U = 1-8 eV) and HSE06 level.

REOs	PBE	PBE+U								HSE06
		U=1	U=2	U=3	U=4	U=5	U=6	U=7	U=8	
LaF_3	235.65	234.60	234.23	234.84	234.05	234.05	234.12	234.11	234.10	229.36
CeF_3	234.92	230.45	230.45	230.59	230.59	230.59	230.59	230.59	230.59	223.95
PrF_3	222.75	222.56	222.56	222.56	222.56	222.56	222.56	222.56	222.56	218.16
NdF_3	219.34	219.33	219.03	219.23	219.15	219.20	219.35	219.23	219.21	214.66
PmF_3	215.68	215.68	215.68	215.68	215.67	215.68	215.68	215.67	215.69	211.01
SmF_3	212.09	213.05	213.42	212.96	212.74	212.78	213.10	213.18	213.36	-
EuF_3	212.53	212.35	212.63	212.35	212.82	212.59	212.34	212.77	212.79	205.05
GdF_3	207.82	207.94	207.74	207.88	208.15	207.90	208.17	207.75	207.70	203.63
HoF_3	200.38	199.69	199.69	199.77	200.34	199.62	199.56	199.05	198.73	195.39
ErF_3	205.31	204.74	204.71	205.46	205.07	204.00	205.12	205.57	205.23	198.86
TmF_3	203.65	203.37	203.04	203.38	203.38	203.38	203.38	203.38	203.38	196.45
LuF_3	199.25	199.25	199.25	199.45	199.25	199.45	199.45	199.45	199.45	194.64

2.1.3 Fluorite-type CeO_2

We specifically focused on cerium dioxide (CeO_2), the most common and well-studied REO, to compare the HSE06 and PBE+U methods for its lattice geometry with hexagonal Ce_2O_3. In the previous studies of CeO_2 using various state-of-the-art approaches to obtain the equilibrium lattice parameter a_0 and the volume V_0, Hay et

al.[102] applied the Birch-Murnaghan equation of state[105-106] to fit the energy-versus-volume curve and derived a_0 of 5.41 Å for CeO_2 with the HSE method, while Da Silva et al.[30] minimized the stress tensor and all internal degrees of freedom and obtained the optimal value of a_0 of 5.40 Å with HSE03, very close to the result of Hay et al.[102]. In another study based on the atom-centered basis sets rather than the plane-wave basis sets with the HSE06 functional, a value of a_0 of 5.408 Å was calculated.[29] Our calculations based on optimizing the stress tensor of the crystal cell and performed with the HSE06 hybrid functional also predicted a value of the lattice parameter a_0 (5.39 Å) close to the above results.

Table 2.3. Equilibrium lattice parameters a_0 (in Å) and volume (in Å^3) of CeO_2 calculated by PBE, PBE+U (U = 1-8 eV) and HSE06 methods.

Lattice parameter	PBE	PBE+U								HSE06
		U=1	U=2	U=3	U=4	U=5	U=6	U=7	U=8	
a_0	5.48	5.48	5.49	5.49	5.50	5.50	5.51	5.51	5.52	5.39
Volume	164.26	164.26	165.30	165.75	166.23	166.50	167.16	167.65	168.05	156.97

When comparing to the reported experimental values of the lattice parameter a_0, 5.39 Å[107], 5.406 Å[108] and 5.411 Å[109], it is found that the HSE06 functional predicts very accurate geometry irrespective of the types of basis sets or the methods of cell volume optimization used in the above-mentioned calculations. However, optimization of the lattice parameters by PBE+U results in a larger deviation from the experimental values for cerium dioxide than for cerium sesquioxide. Increasing the parameter U results in a larger overestimation of the lattice parameters of CeO_2 at the PBE+U level than in the case of Ce_2O_3. Even the smallest considered value of U of 1 eV overestimates the a_0 value (5.48 Å) of CeO_2 by 1.7 % compared to the HSE result (5.39 Å), while the PBE functional without the inclusion of the parameter U also predicts a too larger value of the lattice constant, 5.47 Å. Although larger values of U result in slowly increasing overestimation for the lattice parameter of CeO_2, we find that the U value of 2-3 eV only slightly changes the lattice parameter to 5.49 Å. Therefore, small U values (1-3

eV) or no U give the best agreement between the calculated lattice parameter and the experimental values for Ce(IV) oxide.

2.1.4 COHP analysis of covalent bonding in Ln₂O₃

In the previous sections, we discussed the impact of Hubbard U parameter of the PBE+U approach on the lattice constants of various lanthanide oxides. Furthermore, we selected Ce_2O_3 and Ho_2O_3 as representative early and late Ln sesquioxides, respectively, to investigate the effect of U potential on the M-O bonding and the contribution of 4*f* states to the covalent part of the bonding, which could explain the change of lattice constants upon tuning the effective parameter U. Hence, we calculated the crystal orbital Hamilton population (COHP)[110] diagrams and the integrated values (ICOHP), respectively, providing us with information about the bonding/anti-bonding contributions between the band-structure energy and on the strength of covalent bonding (the larger the ICOHP value the stronger the covalent bonding). The crystal geometry optimized at the HSE06 level was adopted to calculate the COHP of one pair of Ln-O nearest neighbor contacts (Ln = Ce/Ho) by using the LOBSTER package[111-112] at the PBE+U level with various U values. As shown in Table 2.4, the contribution to covalent bonding of the Ln-O bonds mainly comes from O2*p*-Ln5*d* interactions and partly originates from O2*s*-Ln5*d* interactions, as well as contains a small contribution from the Ln4*f* states. Interestingly, the COHP diagrams for Ce_2O_3 and Ho_2O_3 visually appear to be almost independent of the U value, whereas the quantitative ICOHP values vary slightly by tuning the parameter U. For Ce_2O_3, the net ICOHP values increase slightly with increasing U, where the Ce5*d*-O2*s*, Ce5*d*-O2*p*, and Ce4*f*-O2*p* contributions to bonding show a different type of dependence on U. The contribution of Ce5*d*-O2*s* to the covalent part of the bonding becomes more pronounced with increasing the U parameter. The same is true for the Ce5*d*-O2*p* contribution while the opposite holds for the participation of 4*f* states in covalent bonding, which may possibly

result from the change of the conduction band character from mainly Ce4f to mainly Ce5d upon increasing the U value.
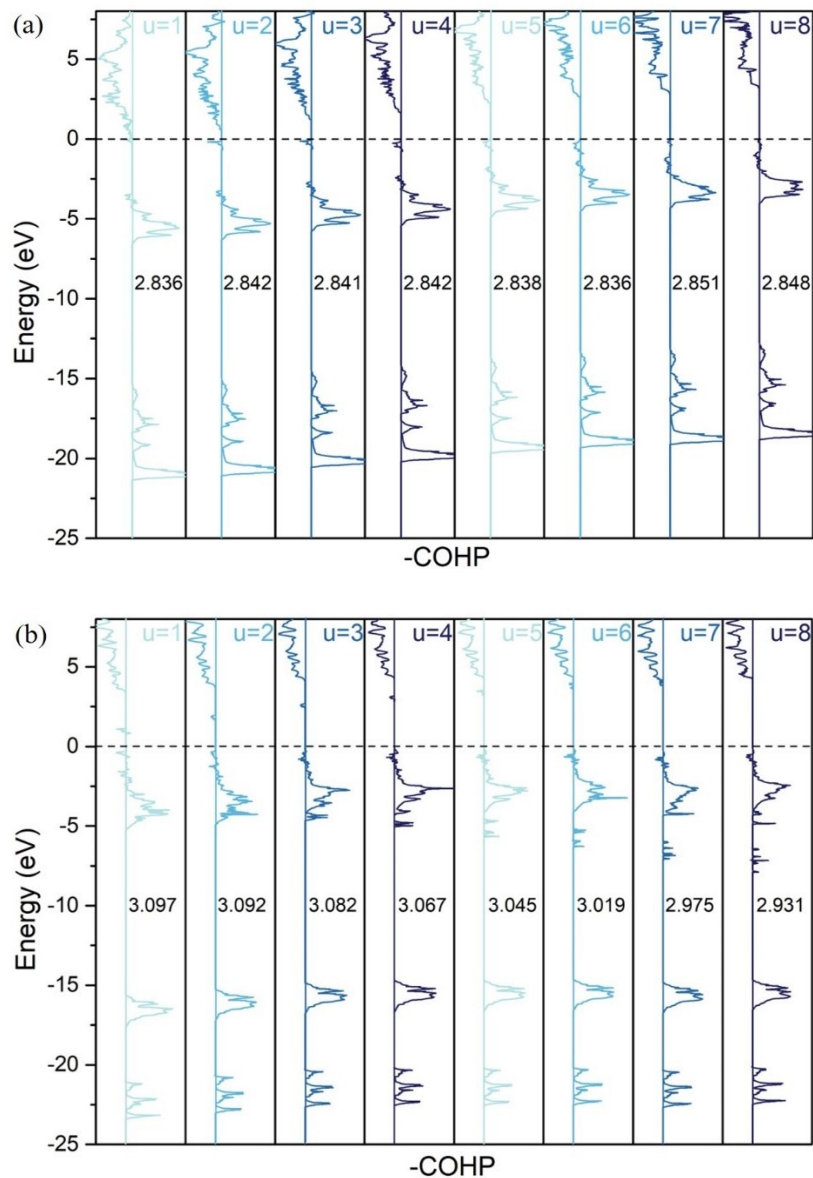
Figure 2.3. The -COHP curves and -ICOHP values for Ce-O or Ho-O bonds in (a) Ce_2O_3 and (b) Ho_2O_3 employing various U values. The calculations were performed at a fixed geometry optimized at the HSE06 level.

Similar to the Ce-O bonds in Ce_2O_3, in Ho_2O_3 the main contribution to covalency comes from Ho5d-O2p interactions, with almost negligible contribution from Ho4f states to Ho-O bonds in Ho_2O_3. Nevertheless, the 4f states of Ho are even more localized than

for Ce and their contribution to covalent bonding decreases with U different from Ce4*f* states. Moreover, the degree of Ho5*d*-O2*s* and Ho5*d*-O2*p* covalent bonding also decreases with U, opposite to what was found for Ce_2O_3.

Table 2.4. The -ICOHP values of Ln5*d*-O2*s*, Ln5*d*-O2*p* and Ln4*f*-O2*p* (Ln = Ce, Ho) for Ce_2O_3 and Ho_2O_3 calculated by PBE+U with U = 1-8 eV.

	PBE+U							
	U=1	U=2	U=3	U=4	U=5	U=6	U=7	U=8
Ce5*d*-O2*s*	0.734	0.742	0.743	0.743	0.744	0.745	0.747	0.747
Ce5*d*-O2*p*	1.355	1.376	1.384	1.391	1.395	1.399	1.412	1.413
Ce4*f*-O2*p*	0.190	0.157	0.147	0.140	0.133	0.127	0.125	0.120
Ho5*d*-O2*s*	1.022	1.021	1.019	1.017	1.013	1.008	1.0	0.989
Ho5*d*-O2*p*	1.441	1.441	1.441	1.438	1.430	1.417	1.390	1.358
Ho4*f*-O2*p*	0.056	0.051	0.045	0.039	0.034	0.030	0.026	0.025

2.2 Thermodynamic Properties

2.2.1 A-type Ln₂O₃

In addition to the crystal structure discussed in the previous sections, the other property of interest is the reaction energy especially in modelling the reaction mechanism of catalytic reactions. The enthalpy of formation of an oxide from the elements is often treated as a model reaction to assess the performance of PBE+U and HSE06 functionals. However, DFT suffers from a failure in describing the electronic structure of the O_2 ground state. Therefore, we selected the following imaginary reference reaction,

$$2LnF_3 + 3H_2O \rightarrow Ln_2O_3 + 6HF \qquad (2.1)$$
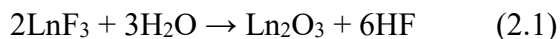
to investigate the influence of the parameter U of PBE+U on the thermodynamic properties of A-type Ln_2O_3 and its performance in comparison to the HSE06 functional, which allowed us to avoid the calculation of O_2 and metallic Ln. Hence, the chosen reaction is intrinsically more balanced because it incorporates six polar covalent bonds (in $3H_2O$ or 6HF molecules, respectively) and an ionic compound on each side. Furthermore, H_2O and HF are both molecular compounds known to be described well by standard DFT, while LnF_3 and Ln_2O_3 are both ionic compounds, furthermore, the

electronic energies of LnF_3 are hardly dependent on the variation of the U parameter (see Figure 2.4). The invariance of the electronic energies of lanthanide fluorides with respect to tuning the U parameter, allows us to focus on the performance of the PBE+U with various U and HSE06 functional on the electronic structure of the lanthanide oxide.
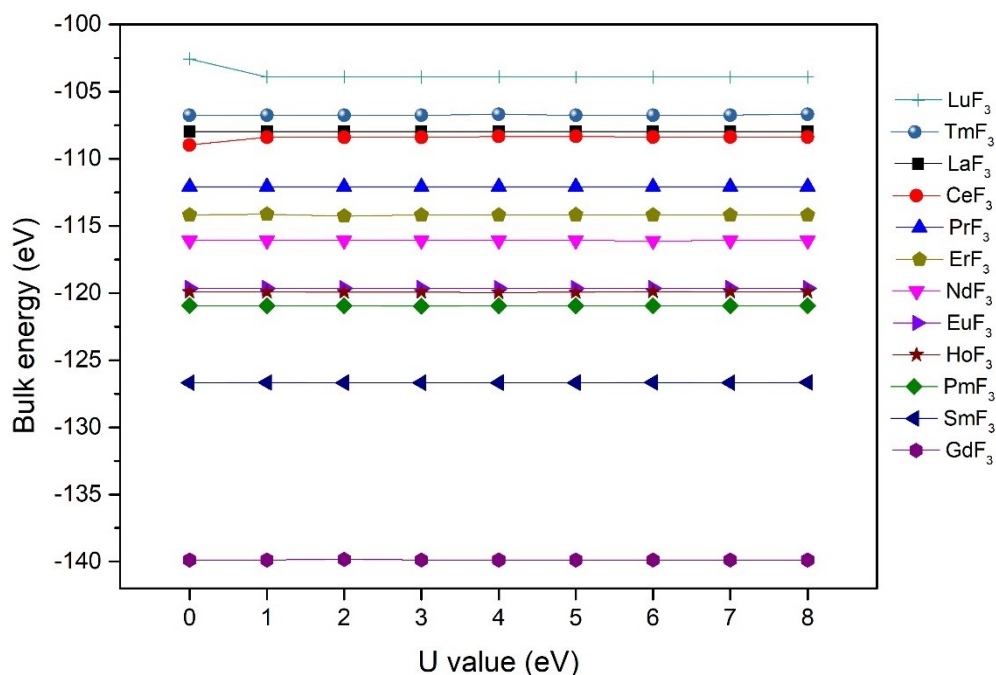
Figure 2.4. The equilibrium bulk energies of YF_3-type LnF_3 (Ln = La, Ce, Pr, Nd, Pm, Eu, Gd, Ho, Er, Tm, Lu) calculated by PBE (U = 0 eV) and PBE+U (U = 1-8 eV).

The performance of PBE+U and HSE06 methods on the energetic properties of A-type Ln_2O_3 has been assessed based on the reference reaction (2.1). As shown in Figure 2.5(a), the HSE06 hybrid functional predicts a slow lowering of the reference reaction energy as the Ln atomic number increases from ~7 eV to ~6.5 eV, except for two cusps seen for Eu and Tm. The appearance of the two cusps can be rationalized after looking at the variation of the Ln_2O_3 and LnF_3 bulk energies calculated with the HSE06 functional across the Ln series. The calculated HSE06 total energies for bulk Ln_2O_3 and LnF_3 have a similar non-linear dependence on the Ln atomic number, steadily decreasing from La to Gd and increasing again from Gd to Lu. The big drop of the

21

energies for Gd sesquioxide and fluoride is attributed to the stabilization of the half-filled f shell of Gd.
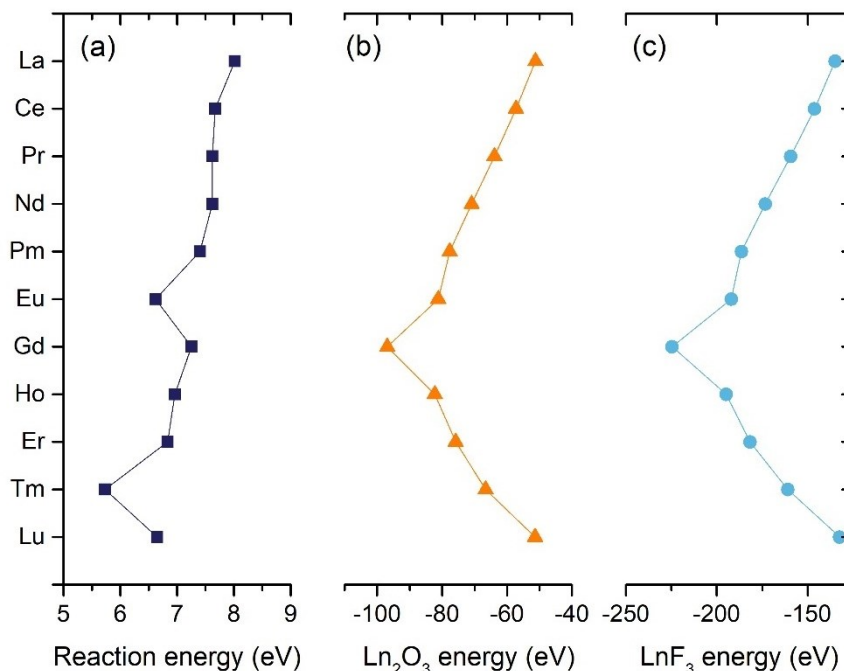
Figure 2.5. (a) Energies (in eV) of the reference reaction $2LnF_3 + 3H_2O \rightarrow Ln_2O_3 + 6HF$ and total electronic energies of (b) A-type Ln_2O_3 and (c) YF_3-type LnF_3 (Ln = La, Ce, Pr, Nd, Pm, Eu, Gd, Ho, Er, Tm, Lu) calculated at the HSE06 level.

In selected cases, the "experimental" reaction enthalpy of reaction (2.1) could be estimated from the available experimental enthalpy of formation of A-type Ln_2O_3[113] and LnF_3[114] (Ln = La, Pr, Nd, Gd, Ho, Er) and gas molecules (H_2O and HF).[115] These experimental reaction enthalpies estimated in this fashion are listed in Table 2.5. By comparing the reaction energies obtained based on the experimental values and the energies calculated with the PBE or HSE06 functional, we found that uncorrected PBE performs better than HSE06 for La_2O_3, Nd_2O_3 and Er_2O_3, but worse than HSE06 for Pr_2O_3, Gd_2O_3 and Ho_2O_3. However, HSE06 shows smaller maximum deviation and overall better agreement with the experiment than PBE among the considered Ln_2O_3 (Ln=La, Pr, Nd, Gd, Ho, Er), where HSE06 predicts the reaction energy with a less root mean square error (RMSE) of 0.8 eV than PBE (RMSE: 1.2 eV) relative to the

experimental values. An earlier study has shown that the performance of the HSE06 functional could be further tuned by adjusting the fraction of exact exchange to 15%, which improved the agreement with the experiment for the energy of the conversion reaction from CeO_2 to Ce_2O_3,

$$2CeO_2 \rightarrow Ce_2O_3 + 0.5\,O_2 \qquad (2.2)$$
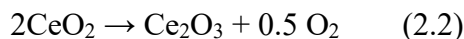
and also gave a good agreement with experimental data for the electronic DOS.[116] Although the reaction energies calculated by the hybrid functional do not always perfectly agree with the experimental values, we still treat the HSE results as the benchmark to assess the PBE+U results in view of the lack of the experimental data on the thermodynamic properties of the whole lanthanide compounds. Moreover, the currently available experimental data are not always mutually consistent, as they were obtained by different techniques or at different experimental conditions and sometimes not known with sufficient accuracy. Speaking of LnF_3 (Ln = La, Pr, Nd, Gd, Ho, Er) as an example, the experimental enthalpies of formation were reported in ref.[114] based on unknown lattice structure types, possibly belonging to YF_3-type or LaF_3-type.

Table 2.5. Calculated (by PBE or HSE06 functional) and experimental values of the reaction energies (in eV) for the reference reaction $2LnF_3 + 3H_2O \rightarrow Ln_2O_3 + 6HF$ (Ln = La, Pr, Nd, Gd, Ho, Er).

	La_2O_3	Pr_2O_3	Nd_2O_3	Gd_2O_3	Ho_2O_3	Er_2O_3
PBE	7.54	7.72	6.74	5.09	8.30	6.15
HSE06	8.02	7.62	7.62	7.25	6.96	6.83
Expt.	7.23	6.82	6.65	6.93	6.24	5.98

Compared to the reaction energies calculated with the HSE06 functional, the U values of 2-3 eV allowed for the best agreement between HSE06 and PBE+U reaction energies for La_2O_3, Ce_2O_3, Nd_2O_3 and Ho_2O_3 as shown in Figure 2.6(a) and (c). Here we refer to published studies about the performance of DFT+U for Ce_2O_3, which was assessed with respect to energies of other types of model reactions. For reaction (2.2), accurate energies could be determined at the PW91+U level with the same optimal range of U

values (around 2 eV) as found in this work for PBE+U and our studied reaction (2.1).[38] A similar optimal U value of 1-2 eV was also derived by applying the PBE+U functional to reaction (2.2).[30] Note that two different oxidation states, trivalent and tetravalent Ce are involved in the reaction (2.2), indicating that it is a redox process. The observation that the optimal U value determined by our considered reaction (2.1) also works well with other types of reactions, including redox processes, is a good sign suggesting transferability of optimal U values.

For Er_2O_3, the closest agreement between PBE+U and HSE06 for the reaction energy of (2.1) is achieved with the U value of 6 eV, but lower values of the U parameter, U = 2-6 eV, also give reasonable agreement within the error of 0.4 eV. The minimum deviation of PBE+U reaction energies of (2.1) from the HSE06 values could be achieved at U = 1 eV for Pr_2O_3, Pm_2O_3 and Lu_2O_3, where the error of PBE+U increases with the U value and reaches its maximum at U = 7 eV, Figure 2.6(b) and (c). The best agreement between the PBE+U and HSE06 results for Eu_2O_3 and Tm_2O_3 is also achieved at U = 1 eV, whereas the maximum deviation from the benchmark does not exceed 2 eV even at higher U values, Figure 2.6(b) and (c). For Gd_2O_3 the parameter U has almost no effect on the calculated reaction energies at the PBE+U level, which underestimates the energy by around 2 eV compared to the HSE06 results, showing a poor agreement between PBE+U and HSE06, which is not fixed by tuning the U parameter, Figure 2.6(c). In conclusion, the minimum deviation between PBE+U and HSE06 could be achieved for the chosen reference reaction at U = 2-3 eV for La_2O_3, Ce_2O_3, Nd_2O_3 and Ho_2O_3. The same is true for Er_2O_3 where the good agreement is maintained even when increasing the U value up to 6 eV, while the opposite holds for Pr_2O_3, Pm_2O_3, Eu_2O_3, Tm_2O_3 and Lu_2O_3, where U = 1 eV gives the best fit to HSE06. For Gd_2O_3, the energy of our model reaction significantly deviates between PBE+U and HSE06 (by >2 eV) at any of the considered U values.
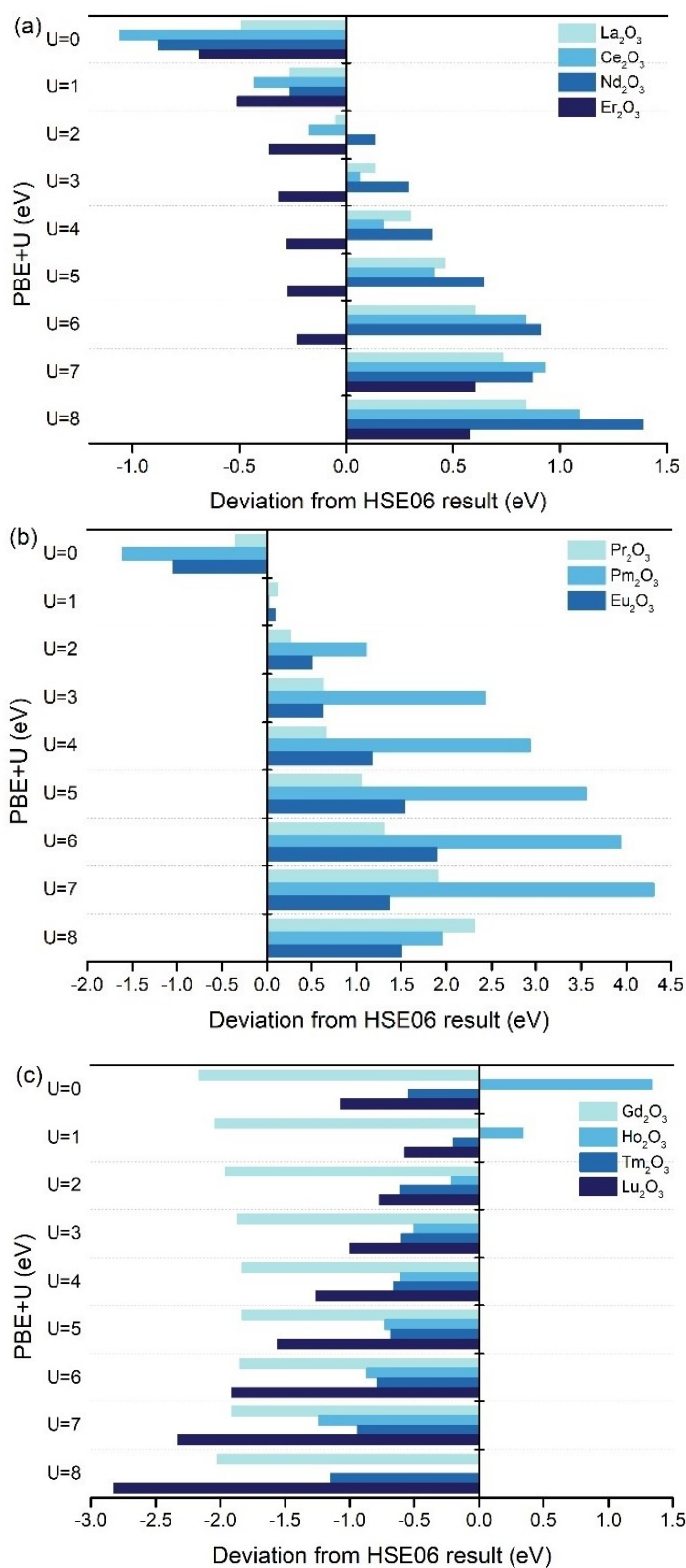
Figure 2.6. Relative energies (in eV) of the reference reaction $2LnF_3 + 3H_2O \rightarrow Ln_2O_3 + 6HF$ (Ln = La, Ce, Pr, Nd, Pm, Eu, Gd, Ho, Er, Tm, Lu) calculated by PBE (U=0 eV) or PBE+U (U = 1-8 eV) with respect to the HSE06 functional. For clarity, the results are separately shown in three figures, (a), (b) and (c).

25

2.2.2 Fluorite-type CeO_2

For the assessment of the PBE+U method for predicting energies of reactions involving CeO_2, we selected a stoichiometric model reaction, shown below:

$$2CeF_3 + 4H_2O \rightarrow 2CeO_2 + H_2 + 6HF \qquad (2.3)$$
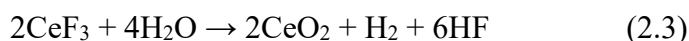
Reaction (2.3) is analogous to the reaction designed for A-type Ln_2O_3, except that it involves the change in the oxidation state of Ce from Ce(III) to Ce(IV); therefore, water is reduced to H_2. The reaction energy of (2.3) calculated for CeO_2 at the PBE+U level increases almost linearly with the increasing U parameter, getting closest to the HSE06 result (21.96 eV) at U = 3 eV (22.76 eV). The optimal value of U is the same as found for Ce_2O_3 in spite of the different oxidation state and coordination environment of ceria. We now would like to compare this result to an earlier published study on reaction (2.2), namely, the conversion reaction from CeO_2 to Ce_2O_3, where the best agreement with the experimental value could be achieved by using PBE+U with the U value of 1-2 eV.[30] In the present work, through replacing the dioxygen by H_2O – H_2 to avoid calculating the energy of molecular oxygen, a modified reaction, $2CeO_2 + H_2 \rightarrow Ce_2O_3 + H_2O$, was used to assess the performance of PBE+U. For this reaction, U = 0.2 eV gave the closest agreement to the experimental value, 138 kJ/mol.[117] Moreover, the calculated value of the reaction energy ($2CeO_2 + H_2 \rightarrow Ce_2O_3 + H_2O$) using U = 1-2 eV was still close to the experimental value within the error of 0.5 eV,[117] which is in line with the optimal U range found in ref.[30] Similarly, the U value of 2 eV was found optimal to reproduce the experimental reaction energy for the formation reaction of CeO_2 from the Ce metal and O_2 without considering the correction to the O_2 energy using a different functional, PW91+U.[38] Note that the HSE06 hybrid functional with an atom-centered basis set underestimates the reaction energy of reaction (2.2) by around 1.0 eV compared to the experimental value.[29] The optimal parameter U obtained for reaction (2.2)[30] could thus be adjusted to 3 eV if fitted to the HSE06 benchmark value, which is in agreement with the optimal U value found in this work based on our proposed reference reaction (2.3). It also remains consistent with the optimal parameter

U obtained by fitting the PBE+U energy of reference reaction (2.1) for the cerium sesquioxide to the benchmark HSE06 value. Therefore, it appears that the optimal range (2-3 eV) of U values derived above for Ce should be applicable to calculating reaction energies of different reactions including our proposed reference reaction and redox reactions, suggesting that the optimal U ranges obtained for other lanthanide oxides are probably transferable to different reaction schemes at the GGA+U (PBE or PW91) level.
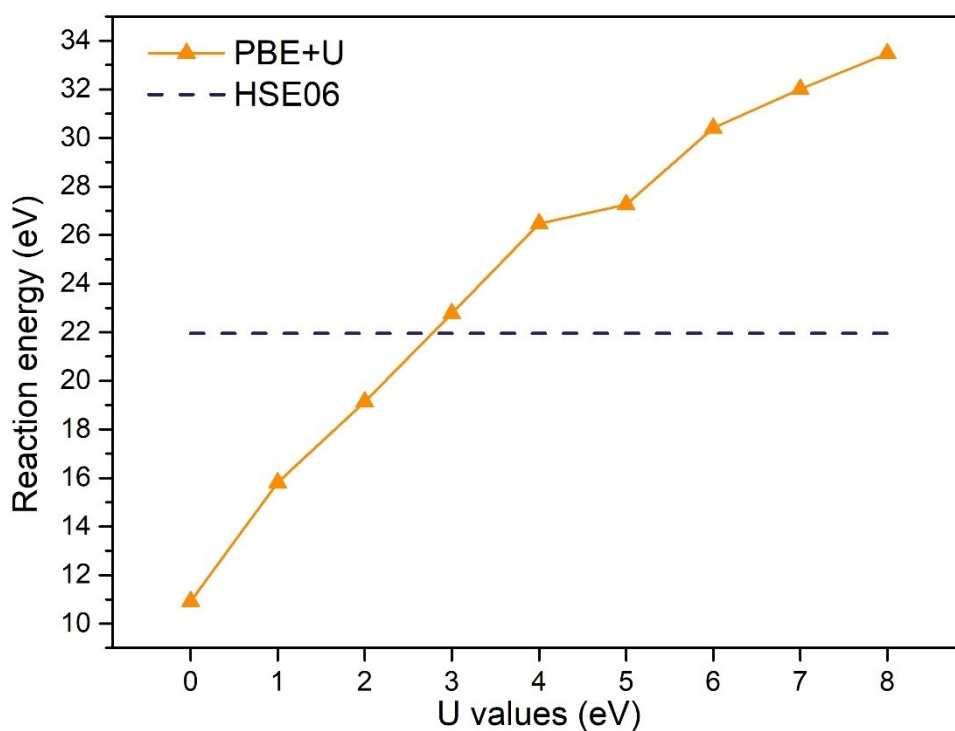
Figure 2.7. Calculated energies of a reference reaction for fluorite-type CeO_2 by PBE (U=0 eV) or PBE+U (U = 1-8 eV) as well as HSE06 functional. Reference reaction: $2CeF_3 + 4H_2O \rightarrow 2CeO_2 + H_2 + 6HF$.

Chapter 3 Assessment of the DFT+U and HSE06 Methods for Modelling Adsorption Reactions at Rare Earth Oxides Surface

In Chapter 2, we investigated how the lattice parameters and the reaction energies of A-type Ln_2O_3 and fluorite-type CeO_2 are dependent on the Hubbard U parameter of PBE+U, and discussed the degree of agreement with the benchmark results obtained using the hybrid HSE06 functional or with the available experimental results. Because our reactions of interest are surface reactions and molecular adsorption on the surfaces of REOs, it is necessary to evaluate the transferability of the derived optimal U parameter from bulk REO calculations to chemical processes on the REO surfaces. For this purpose, we selected CeO_2 and Nd_2O_3 as representatives of dioxide and sesquioxides of REOs, respectively. We constructed the corresponding surface slabs and assessed the electron localization of Ce and Nd ions, the work function, and the adsorption energies of the CH_3 radical and NH_3 molecule as a function of the U parameter. In this chapter, $Nd_2O_3(0001)$ and $CeO_2(111)$ surfaces were considered for Nd_2O_3 and CeO_2, respectively. A $p(3\times3)$ supercell comprising nine layers was built for the $CeO_2(111)$ surface, while the $Nd_2O_3(0001)$ surface was modelled by a $p(2\times2)$ surface slab including ten layers, where the bottom half of the surface slabs was constrained to the optimized bulk crystal structure.

3.1 Degree of Electron Localization

When discussing the applicability of the GGA+U approach to describe the electronic structure of REO surfaces, the primary focus is on the localization of the $4f$ electrons in these strongly correlated systems. With regard to the degree of localization of the f-shell electrons of lanthanide elements, we are first interested in the dependence of this property on the U parameter of PBE+U and we shall also compare the PBE+U description of REO surfaces with the results obtained using the HSE06 functional. The

net ionic charges, calculated by subtracting the valence charges obtained by Bader projections[118] of the computed total electron charge density from the number of valence electrons given in the PAW potentials, could give us an indication of the $4f$ electron localization degree in the surface Ln atoms. It needs to be mentioned that the density partitioning scheme, i.e. Bader charge analysis[119-122] used in this section, has a great effect on the results of the obtained ionic charges. Hence, caution should be exerted when interpreting these charges.

On a regular CeO_2(111) surface (here and further in this chapter we apply the term "regular" to a surface without oxygen vacancies), the average net ionic charge of the surface Ce ions is predicted to be +2.26 e by the conventional PBE functional without the Hubbard term, and then steadily increases to +2.44 e (U = 8 eV) with the increase of the U parameter at the PBE+U level. Our results calculated at the PBE+U level are in quantitative agreement with those for bulk CeO_2 obtained using the LDA+U approach in the published work by Castleton et al.[33] Compared to the results (+2.51 e) of HSE06 obtained in this work, PBE+U predicts a slightly smaller net ionic charge, where both the results are smaller than the nominal charge on Ce(IV), +4 e, owing to some covalence character present in the Ce-O bonds, as indicated by the COHP analysis in section 2.1.4.

We will apply the term "defective" or "reduced" to REO surfaces with O vacancies. In terms of the CeO_2(111) surface, an oxygen vacancy forms by removing one surface lattice oxygen atom from the surface. Because of the formal -2 charge on the O ion, removing a neutral atom formally results in two excess electrons left on the surface, which become mainly distributed on the surface atoms adjacent to the vacancy including two surface Ce ions near the vacancy.[123] However, the actual calculated charges on O atoms are only -1.13 e (PBE, U = 0 eV). Upon removal of an O atom, this charge delocalizes on all ions. Nevertheless, Ce ions close to the vacancy bear a slightly less positive charge +2.21 e than those far from the vacancy, +2.24 e (PBE, U = 0 eV). Upon increasing the U parameter, the average net ionic charge on the two Ce ions close

to the vacancy site decreases from +2.21 e (PBE, U = 0 eV) to +2.07 e (U = 8 eV) owing to partial localization of the excess electrons near the defect site. Simultaneously, the average net ionic charge of Ce ions far from the defect becomes more positive from +2.24 e (PBE, U = 0 eV) to +2.43 e (U = 8 eV), which is close to the net ionic charge of Ce ions on the regular CeO_2(111) surface calculated with U = 8 eV. Hence, the difference between the net ionic charges of the Ce ions near the vacancy and those far from the vacancy increases with the increase of the U parameter, especially at the U values above 3 eV, which is an expected result consistent with the findings for bulk CeO_2 by Castleton et al.[33], indicating that increasing U results in a stronger electron localization.
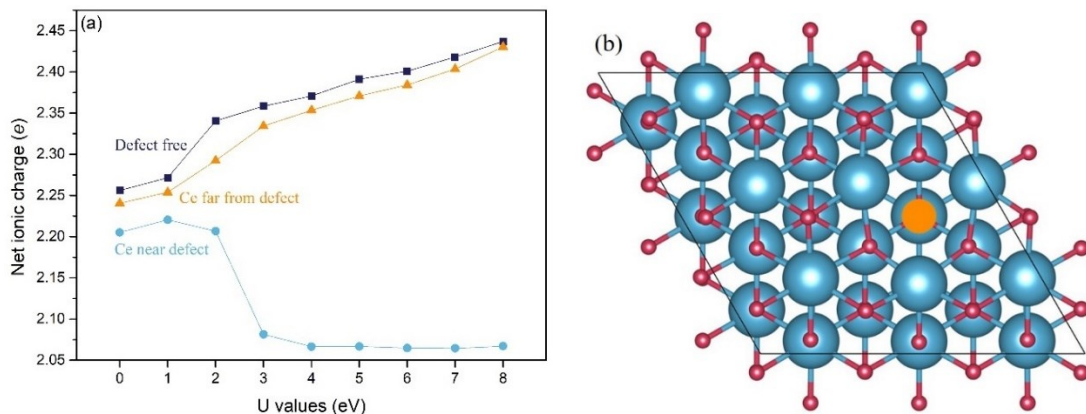
Figure 3.1. (a) Average net ionic charges of Ce ions on the CeO_2(111) surfaces as a function of U. The three plots correspond to Ce ions on the regular surface (dark blue squares), two Ce ions with the lowest net ionic charge (light blue circles), and Ce ions far from the oxygen vacancy site (orange triangles). (b) Top view of the CeO_2(111) surface with one surface oxygen vacancy highlighted in orange. Ce atoms are shown in blue and O atoms in dark red.

A similar dependence on the U parameter was found for the net ionic charge of Nd ions on the Nd_2O_3(0001) surface as shown in Figure 3.2. The net ionic charge of Nd ions on the regular Nd_2O_3(0001) surface increases with an increasing U value of PBE+U. On the defective Nd_2O_3(0001) surface, the net ionic charge of Nd ions near the oxygen vacancy reaches a constant value of +1.63 e at U = 3 eV, while the charge on the Nd

ions far from the defect, increases from +1.90 e (U = 0 eV, i.e. PBE) to +2.03 e (U = 8 eV). Therefore, the charge difference between the two types of Nd ions increases, similar to what was observed for the CeO$_2$(111) surface, suggesting that the degree of electron localization also increases on the Nd$_2$O$_3$(0001) surface with increasing U.
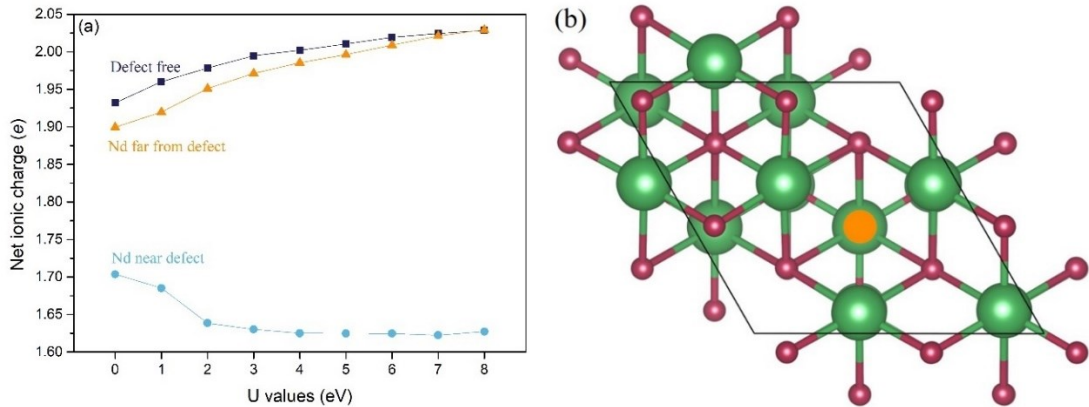
Figure 3.2. (a) Average net ionic charges of Nd ions on the Nd$_2$O$_3$(0001) surfaces as a function of U. The three plots correspond to Nd ions on the regular surface (dark blue squares), three Nd ions near the oxygen vacancy site (light blue circles), and Nd ions far from the oxygen vacancy site (orange triangles). (b) Top view of the Nd$_2$O$_3$(0001) surface with one surface oxygen vacancy highlighted in orange. Nd atoms are shown in green and O atoms in dark red.

However, it is not possible to separate the localization of the f-shell electrons using the net ionic charges, which is unable to distinguish between the contributions of p, d, and f electrons of surface Ce/Nd ions. Therefore, we have also looked at the contributions of 4f orbitals to local magnetic moments of surface Ce and Nd ions as an alternative way of assessing the influence of the U parameter on the 4f electrons localization.

On a defective CeO$_2$(111) surface, the formation of an oxygen vacancy leaves two extra electrons on the defect site, which are expected to localize on two adjacent Ce ions, i.e. two tetravalent Ce ions change their oxidation state to trivalent and acquire a 4f^1 electronic configuration. The change of the valences of two Ce ions near the vacancy was also reflected by the average contributions of 4f orbitals to local magnetic moments of Ce ions which hits the plateau at U = 4 eV beyond 0.9 μ_B as shown in Figure 3.3(a).

Whereas the average magnetic moment of Ce ions close to the oxygen vacancy is only 0.09 μ_B without the inclusion of the parameter U, the U correction, especially at U > 3 eV, leads to increased contributions of $4f$ orbitals to local magnetic moments, indicating that the localization of $4f$ electron of Ce atoms could be achieved at U = 3 eV, which is slightly larger than the optimal U required to reproduce the lattice parameters and reaction energies (U = 1-3 eV) of the bulk CeO_2.

On the regular $Nd_2O_3(0001)$ surface, trivalent Nd ions corresponds to a $4f^3$ configuration, consistent with the calculated contributions (closer to 3) of $4f$ orbitals to local magnetic moments of Nd ions shown in Figure 3.3(b). With the formation of the oxygen vacancy, the two excess electrons tend to spread over the surface or stay in the defect site owing to the irreducibility of Nd ions. This is reflected in the slightly increased $4f$ contribution to magnetic moments for the surface Nd ions on the defective surface compared to the regular ones. On the defective $Nd_2O_3(0001)$ surface, the average magnetic moment of the three Nd ions near the vacancy climbs up to a maximum, 3.16 μ_B, at U = 2 eV and then declines to 3.02 μ_B at U = 8 eV. For the Nd ions far from the oxygen vacancy the average contribution from $4f$ electrons to the magnetic moment shows a continuous decrease from 3.09 to 3.01 μ_B as U increases from 0 to 8 eV. Therefore, the excess electrons partially localize on the $4f$ orbitals on the defective $Nd_2O_3(0001)$ surface. The highest degree of localization is achieved at U = 2-5 eV, based on the maximum difference of magnetic moments between the two types of Nd ions: either close to or far from the defect. Different from the continuous increase of the net ionic charge difference between the Nd ions near to and far from the oxygen vacancy on the defective $Nd_2O_3(0001)$ surface shown in Figure 3.2(a), the difference between the magnetic moments for the two types of Nd ions decreases and almost vanishes for U = 8 eV, indicating a failure in describing the $4f$ electron localization at large U values. It is partly due to the indirect net ionic charge analysis including the contributions from all orbitals and partly attributed to the difference of density partitioning scheme, where the Bader volume is constructed in the charge

analysis, while the atom-centered Wigner-Seitz spheres are used in the magnetization calculations. In conclusion, the optimal range of U for Nd_2O_3 is confirmed to lie at 2-3 eV, which works best for proper description of the 4*f* electron localization as well as for best prediction of the lattice constants and reaction energies, as discussed in Chapter 2 for Nd_2O_3 bulk.
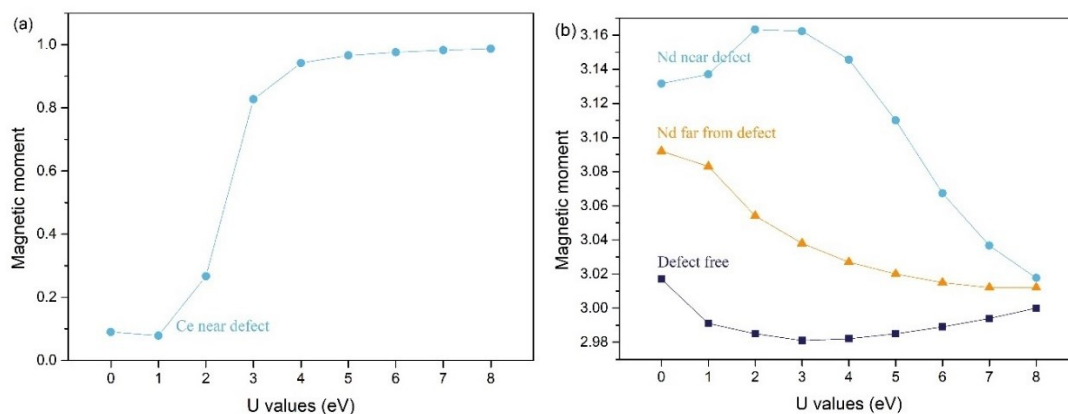
Figure 3.3. Average contributions of 4f orbitals to local magnetic moments of (a) two Ce atoms with the highest magnetic moment near the vacancy site on the defective $CeO_2(111)$ surface and (b) Nd atoms on the regular $Nd_2O_3(0001)$ surface (dark blue squares), three Nd atoms near the oxygen vacancy site (light blue circles), and Nd atoms far from the oxygen vacancy site (orange triangles) on the defective $Nd_2O_3(0001)$ surface as a function of U.

3.2 Surface Reactivity Described by the Work Function

In this section, we will assess the performance of PBE+U and HSE06 on the surface reactivity of the two previously selected surfaces, $CeO_2(111)$ and $Nd_2O_3(0001)$, as well as the $Ce_2O_3(0001)$ surface, to allow for a comparison between the surfaces of cerium dioxide and sesquioxide. The surface reactivity will be measured by its work function reflecting the ability to release an electron from the surface, calculated as the energy difference between the Fermi energy and the energy of an electron at rest in the vacuum nearby the surface.[124]

As shown in Figure 3.4, the U parameter of the PBE+U method has no evident influence on the work function of the $CeO_2(111)$ surface. PBE+U predicts the value of the work

function around 6.30 eV, far smaller than the result obtained at the HSE06 level with a large deviation up to 1.2 eV, showing that the description of this surface with PBE+U is not satisfactory in terms of the work function. Different from the $CeO_2(111)$ surface, the work function predicted by PBE+U increases with the increasing U for the $Nd_2O_3(0001)$ and $Ce_2O_3(0001)$ surfaces. The work function of the $Ce_2O_3(0001)$ surface increases from 2.50 eV (U = 1 eV) to 5.59 eV (U = 8 eV), the U value of 5 eV being in quantitative agreement with the result of the HSE06 functional. For the $Nd_2O_3(0001)$ surface, the work function calculated at the PBE+U level increases continuously with increasing parameter U, approaches the value of HSE06 functional, and almost levels off at U = 6-8 eV. This optimal range of U values obtained for surface reactivity is substantially higher than that derived earlier for the lattice constants and reaction energies for the calculated bulk Ce/Nd sesquioxides or Ce dioxide.
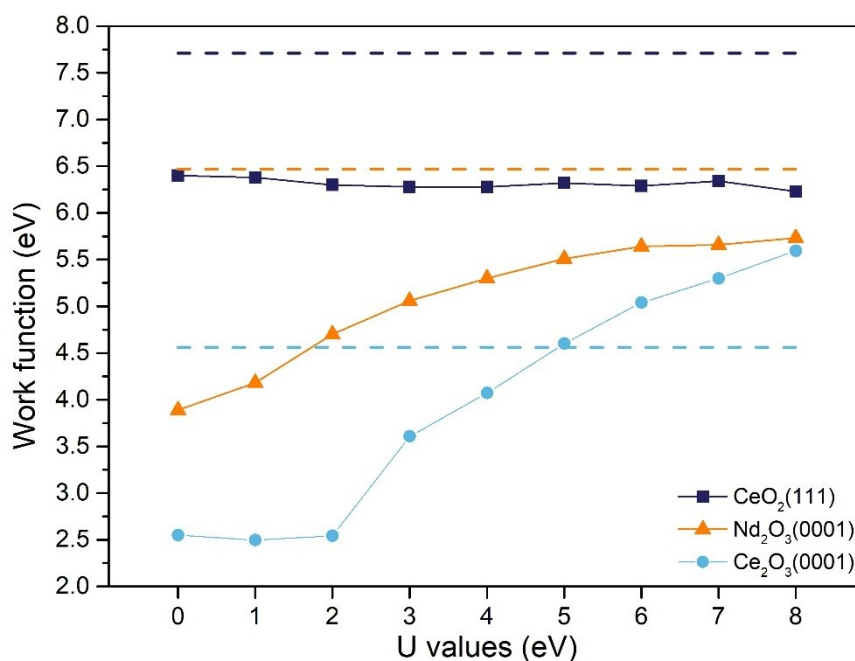
Figure 3.4. Work function for the regular $CeO_2(111)$ surface (dark blue, squares), $Nd_2O_3(0001)$ surface (orange, triangle) and $Ce_2O_3(0001)$ surface (light blue, circles) as a function of the U parameter. All of the horizontal dashed lines separately represent the HSE06 results of the corresponding colors.
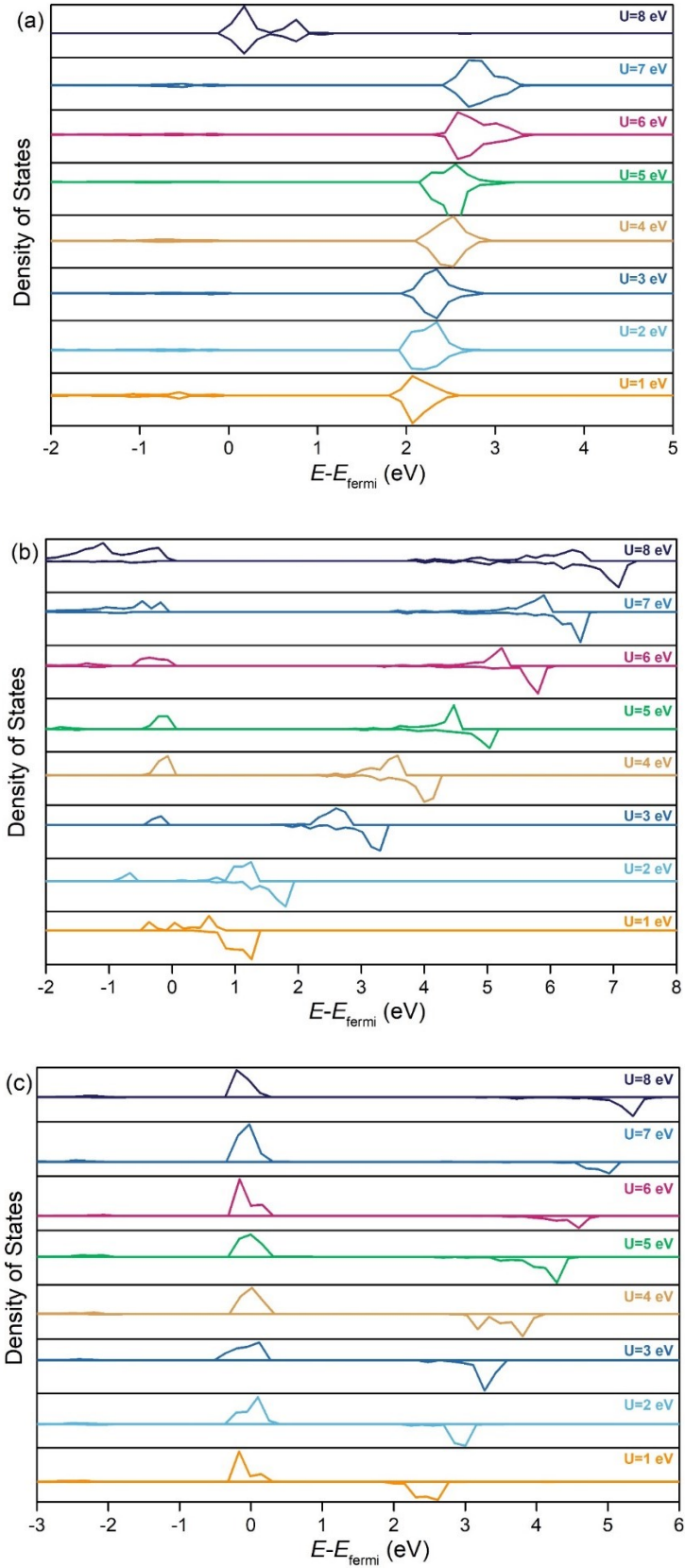
Figure 3.5. The partial density of states (*p*DOS) of Ce(4*f*) or Nd(4*f*) state of (a) CeO$_2$(111), (b) Ce$_2$O$_3$(0001) and (c) Nd$_2$O$_3$(0001) surfaces calculated by PBE+U with U = 1-8 eV.

The partial densities of states (pDOS) of Ce4f or Nd4f states of the CeO$_2$(111), Ce$_2$O$_3$(0001) and Nd$_2$O$_3$(0001) surfaces and their dependence on the U parameter are shown in Figure 3.5. The Ce4f states are mainly unoccupied on the CeO$_2$(111) surface showing that the tetravalent Ce ions cannot be further oxidized, which results in the invariance of the work function with respect to the U value on the surface. However, the Ce4f states on the Ce$_2$O$_3$(0001) surface are partially occupied and partially unoccupied; the Hubbard correction pushes occupied d/f states to lower energy, hence, the work function increases with the parameter U. A similar behaviour is observed for the Nd$_2$O$_3$(0001) surface, for which the unoccupied Nd4f states are forced to higher energy under the correction of Hubbard U.

3.3 Adsorption Properties of CH$_3$ and NH$_3$

In this section, we will investigate the effect of the Hubbard U parameter of PBE+U on the adsorption energies of two probe molecules, CH$_3$ and NH$_3$, on the two selected surfaces: CeO$_2$(111) and Nd$_2$O$_3$(0001). The CH$_3$ and NH$_3$ molecules separately owing an isolated electron or lone pair tend to bind to a surface Ln atom which is prone to accept electrons, as indicated by the unoccupied or partially unoccupied 4f states for the CeO$_2$(111) or Nd$_2$O$_3$(0001) surface in Figure 3.5.

The parameter U of PBE+U has little effect on the adsorption energies of CH$_3$ and NH$_3$ on the CeO$_2$(111) surface, the maximum change in the adsorption energy upon increasing the U value being less than 0.1 eV (see Figure 3.6(a)), similar to the behaviour of the work function. The adsorption energies slightly increase with increasing U parameter and then slightly decrease again. A similar behaviour was observed in a previously published study for the adsorption energy of formaldehyde on a CeO$_2$(111) surface, which was not strongly affected by the U parameter, while a dependence on U was found for the activation and reaction energy of the first C-H bond breaking and for the adsorption energy of the generated adsorbed CHO$^-$ and H$^+$, of

which the barrier energy decreases and the reaction energy becomes more negative with increasing U and both of them come closest to the HSE06 result at U = 3-4 eV.[41] That is, processes including an electron transfer are more affected by the inclusion of the U term in the PBE functional than the weak adsorption of molecules or radicals on the $CeO_2(111)$ surface.

Comparing the adsorption energies of CH_3 and NH_3 calculated by PBE+U and HSE06 methods, we found that HSE06 functional predicts larger (by magnitude) adsorption energies with the maximum difference between the PBE+U and HSE06 results reaching 0.5 eV on $CeO_2(111)$. In order to assess the performance of the HSE06 functional with respect to available experimental data, we also calculated the adsorption energy of an H_2O molecule on $CeO_2(111)$ by HSE06. Water was chosen because no experimental data exist for the adsorption energies of CH_3 and NH_3 on the $CeO_2(111)$ surface. Our calculated adsorption energy of H_2O is -1.45 eV on the (3×3) $CeO_2(111)$ surface using the HSE6 method with DFT-D3 (zero damping)[125] empirical dispersion correction, far larger in magnitude than the experimental desorption energy of H_2O, around -0.9 eV at low coverage.[126] This is an indication that the hybrid functional HSE06 probably also overestimates the adsorption energies of CH_3 and NH_3. PBE+U predicts the adsorption energy of water to be around -0.8 eV on the $CeO_2(111)$ surface, in much better agreement with the experiment. However, it should be noted that the calculated adsorption energy of H_2O also depends substantially on both the coverage of H_2O[38] and the inclusion/non-inclusion of a dispersion correction. A previously published study calculated the adsorption energy of H_2O by HSE06 without a dispersion correction of -0.49 eV on the (2×2) $CeO_2(111)$ surface,[126] lower (in magnitude) than our calculated result (-1.45 eV) on the (3×3) $CeO_2(111)$ surface including the D3 empirical correction to account for dispersion interactions.

We also visualized the interaction between the adsorbates and surfaces by the Independent Gradient Model (IGM) analysis based on the electronic charge density ρ and its derivatives. To this end we plotted the isosurfaces of the $\delta_g{}^{inter}(\rho)$ descriptor,

defined as $\delta_g^{inter}(\rho) = |\nabla\rho^{IGM, inter}| - |\nabla\rho|$, i.e. the difference between the virtual upper limit of electron density representing non-interacting system $|\nabla\rho^{IGM, inter}|$ and the true electron density gradient $|\nabla\rho|$.[127] The isosurface was also colored by the values of sign$(\lambda_2)\rho$ via a blue-green-red color scale, where λ_2 is one of the eigenvalues of the Laplacian of the charge density $\nabla^2\rho$. The colored isosurface reflects the interaction types, where the blue and red colors indicate strong attractive interaction (hydrogen bond, halogen bond etc.) or strong nonbonding overlap, respectively. As shown in Figure 3.6(b), a green isosurface is visible between the CH_3 and the $CeO_2(111)$ surface indicating a weak interaction of CH_3 with the $CeO_2(111)$ surface, consistent with its low adsorption energy around -0.4 eV. The NH_3 adsorption shows larger adsorption energies around -0.8 eV than those of CH_3, which is confirmed by the blue color of the isosurface indicating an attractive interaction between the NH_3 and the surface.
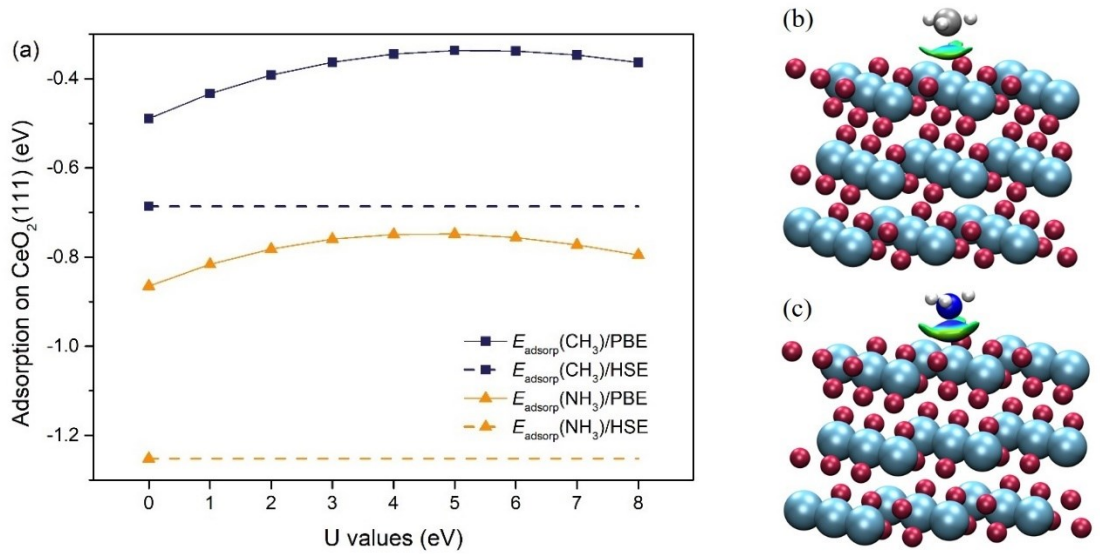
Figure 3.6. (a) Adsorption energy of CH_3 (dark blue, squares) and NH_3 (orange, triangles) on the $CeO_2(111)$ surface as a function of U and the corresponding HSE06 results shown by the horizontal dashed lines. The equilibrium adsorption geometries and IGM isosurfaces of (b) CH_3 and (c) NH_3 molecules on the $CeO_2(111)$ surface calculated by PBE+U with U = 3 eV. Oxygen atoms are shown in dark red, hydrogen atoms in white, nitrogen atoms in dark blue, carbon atoms in silver, and cerium atoms in light blue. The $\delta_g^{inter}(\rho) = 0.01$ a.u. isosurface is shown for the adsorption complexes. A blue-green-red color scale represents the values of sign$(\lambda_2)\rho$ ranging from -0.05 to 0.05 a.u. on the isosurface, where the blue color indicates strong attractive interaction, while the red color indicates strong nonbonding overlap.
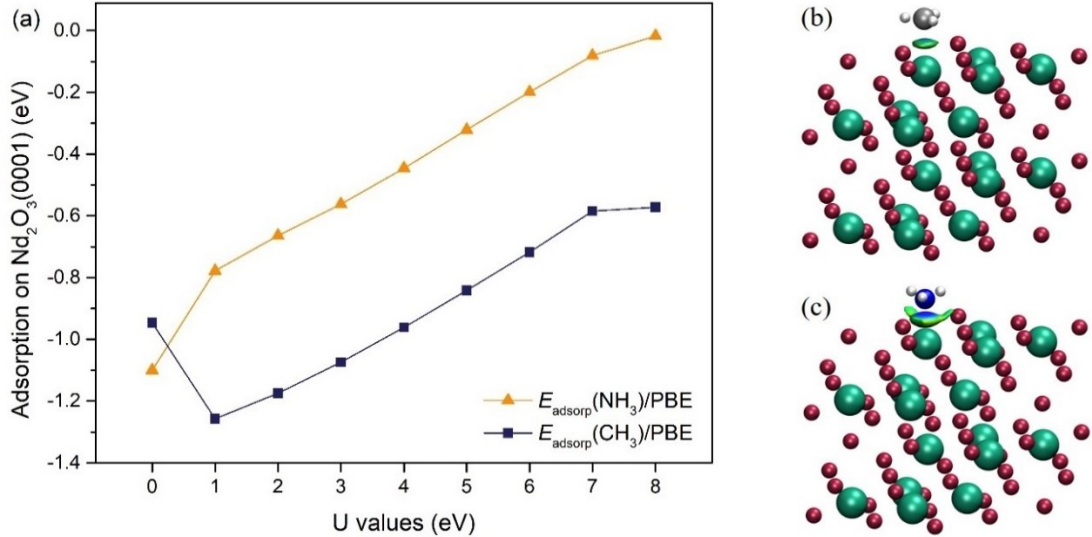
Figure 3.7. (a) Adsorption energy of CH_3 (dark blue, square) and NH_3 (orange, triangle) on the $Nd_2O_3(0001)$ surface as a function of U. The equilibrium adsorption geometries and IGM isosurfaces of (b) CH_3 and (c) NH_3 molecule on $Nd_2O_3(0001)$ surface calculated by PBE+U with U = 3 eV. Oxygen atoms are shown in dark red, hydrogen atoms in white, nitrogen atoms in dark blue, carbon atoms in silver, neodymium atoms in dark green. The $\delta_g^{inter}(\rho) = 0.01$ a.u. isosurface is shown for the adsorption complexes. A blue-green-red color scale represents the values of $sign(\lambda_2)\rho$ ranging from -0.05 to 0.05 a.u. on the isosurface, where the blue color indicates strong attractive interaction, while the red color indicates strong nonbonding overlap.

Different from the small variation of the adsorption energies of CH_3 or NH_3 as a function of the U parameter on the $CeO_2(111)$ surface, the adsorption energies rapidly decrease (in magnitude) with increasing U parameter on the $Nd_2O_3(0001)$ surface, as seen in Figure 3.7(a). The adsorption energy of CH_3 changes from -1.25 eV (U = 1 eV) to -0.6 eV (U = 8 eV), while NH_3 shows weaker adsorption, contrary to the adsorption on $CeO_2(111)$. The adsorption energy of NH_3 changes from -0.75 to 0 eV with increasing U. A small IGM volume ($\delta_g^{inter}(\rho) = 0.01$ a.u.) indicates the electrons participating into the interaction are localized. The adsorption of NH_3 corresponds to a larger IGM volume compared to that of CH_3, while a blue color on the isosurface (see Figure 3.7(b)) shows an attractive interaction between NH_3 and the surface as Lewis acid-base pair. The weakening of CH_3 and NH_3 adsorption with increasing U might be related to the increased degree of localization of $4f$ electrons and their weakened

contribution to bonding on the $Nd_2O_3(0001)$ surface. Unfortunately, our attempts to calculate the adsorption energies of CH_3 and NH_3 on the $Nd_2O_3(0001)$ surface by the HSE06 method were not successful due to a convergence failure. Based on the preceding discussion of the adsorption energies on $CeO_2(111)$, we concluded that the inclusion of a Hubbard correction to PBE functional gives a reasonable description for the adsorption energies of H_2O, CH_3 and NH_3, perhaps even better than the results obtained with the HSE06 functional, which tends to overestimate the adsorption energies.

Chapter 4 Lewis Acidity-Basicity of Doped La_2O_3(0001) Surfaces

In this chapter, we will systematically investigate the influence of heteroatom doping on the Lewis acidity/basicity of the surface lanthanum/oxygen atoms on the doped La_2O_3(0001) surface, chosen as a representative surface of irreducible REOs. Although the Mg or Zr doped La_2O_3(0001) surfaces have been studied in terms of the Lewis acidity/basicity and adsorption properties,[62] systematic studies comparing the effect of heteroatom doping within a group of dopants, including *s*-block, *d*-block and *f*-block elements, on the surface Lewis acidity/basicity is still scarce. Consequently, we constructed a *p*(4×4) model of the La_2O_3(0001) surface comprised of two repeated units (each unit consists of five atom layers in O-La-O-La-O sequence) in the direction normal to the surface based on the crystal unit cell of the HSE06 optimized A-type La_2O_3, as described in Chapter 2. The heteroatoms used to replace the La atom on the surface include *s*-block elements (Li, Na, Mg, Ca), *d*-block elements (Ti, V, Cr, Mn, Fe, Co, Ni, Cu, Mo, Ru,) or *f*-block elements (Ce, Pm, Nd, Eu, Gd, Ho, Er). The PBE functional with the Hubbard correction[31] was employed in the surface calculations, where the U-J values for the *d* orbitals of *d*-block heteroatoms were taken from literature while the U-J parameter values obtained in Chapter 2&3 were adopted for the *f* orbitals of *f*-block dopants, listed as follows: U-J value of 3.0 eV for Ti,[128] 2.5 eV for V,[117] 3.5 eV for Cr, 4.0 eV for Mn,[129-130] 4.0 eV for Fe,[131] 3.5 eV for Co, 6.4 eV for Ni, 4.0 eV for Cu,[132] 8.6 eV for Mo,[117] 3.0 eV for La, Ce, Nd, Ho, 1.0 eV for Pm and Eu, 6.0 eV for Gd and Er.

4.1 The Geometry of Doped La_2O_3(0001) Surfaces

On the regular (= without O vacancies) La_2O_3(0001) surface with one Ln atom per *p*(4×4) unit cell replaced by a dopant metal, the dopant site is a hexa-coordinated (octahedral) site connecting to three surface O atoms (labeled as O_a, O_b, O_c) and three

subsurface O atoms (labeled as O_d, O_e, O_g) as illustrated in Figure 4.1(a). According to their proximity to the dopant site, La and O positions on the regular $La_2O_3(0001)$ surface are divided into two types each, denoted as La_i, La_{ii} or O_i, O_{ii} sites, respectively. For the defective (containing an O vacancy) $La_2O_3(0001)$ surface an additional type of surface cationic sites is introduced, denoted La_{iii}, referring to La atoms adjacent to an oxygen vacancy. An oxygen vacancy is created by removing one O atom at the O_c site from the surface (see Figure 4.1(b)).
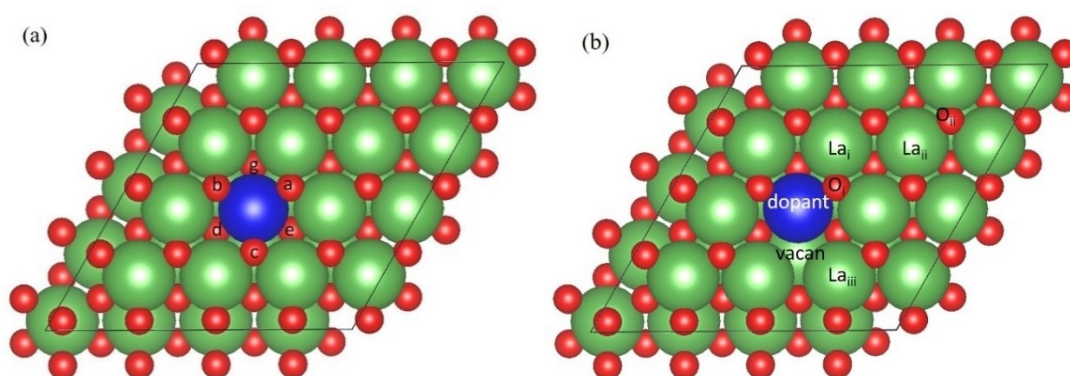
Figure 4.1. Illustration and labeling of (a) six O sites surrounding the dopant site and (b) several types of cationic and anionic surface sites discussed including the dopant site, oxygen vacancy site, surface La or O sites on the $La_2O_3(0001)$ surface. Three surface oxygen atoms are denoted as O_a, O_b, O_c, while three subsurface oxygen atoms are named as O_d, O_e, O_g. La atoms are shown in green, O atoms in red, and dopant atoms in blue.

When heteroatom dopants (whose atomic radii and/or valence state are different from La) are incorporated into the surface, the surface geometry changes accordingly, especially interatomic distances near the doping site. To compare the geometry near the dopant site of regular (no O vacancy) doped surfaces to the respective undoped $La_2O_3(0001)$ surface, we calculated the differences in bond lengths between the dopant atom (labelled as X) and the adjacent oxygen atoms, of which the three surface O atoms are collectively referred to as O_{upper}, while the three subsurface O atoms referred to as O_{lower}. As shown in Figure 4.2, the X-O_{upper} bond lengths on the doped $La_2O_3(0001)$ surfaces generally decrease with respect to the undoped surface. In contrast, the X-

O_{lower} bond lengths on the surfaces doped by the *s*-block and *d*-block heteroatoms (except Mo) increase upon doping. In view of the atomic radius (herein referring to ionic radius[133-134]), the ionic radii (0.6-0.8 Å) of most of *d*-block and *s*-block metals (except Na and Ca) are smaller than the one (1.03 Å) of La. Therefore, the dopant atom is lifted up relative to its position on the undoped surface in the direction normal to the surface, resulting in stronger bonds with the surface O atoms (O_{upper}), while the subsurface O atoms (O_{lower}) slightly shift down by ~0.05 Å enhancing the bonding with the lower La atoms. In addition to the ionic radius, the oxidation state of the heteroatom dopants also has an impact on the surface geometries. Na and Ca, which have large radii of approximately 1.0 Å, only slightly decrease the X-O_{upper} bond length. However, when the oxidation state of Na and Ca is smaller than that of La, the dopants move up to bind more strongly to the surface O atoms, causing the subsurface O atoms attracted by the lower La ions to shift down. This leads to an increase in the X-O_{lower} bond length. However, *f*-block dopants induce contraction of the bond lengths between a dopant atom (X) and the adjacent subsurface O atoms (O_{lower}), indicating that lanthanide dopants (having a slightly smaller ionic radius and same oxidation state relative to La) tend to pull the surrounding oxygen atoms, which causes slight shortening of X-O distances by a similar amount for upper and lower O atoms. This also applies to the Mo dopant which shows a close Bader charge (Mo^{3+}) to La and also has a smaller ionic radius (~0.69 Å). Overall, a much lower degree of deformation is caused by *f*-block dopants compared to *s*-block and *d*-block dopants due to a similar ionic radius and oxidation state of *f*-block dopants to La.

In order to elucidate the effect of an oxygen vacancy on the surface geometries of doped $La_2O_3(0001)$ surfaces, the oxygen atom located at the O_c site was removed from the surface to form one oxygen vacancy. The formation of an oxygen vacancy forces dopants to move closer towards the two adjacent surface O atoms located on O_a and O_b sites, whereas the X-O_g distance to the subsurface O_g atom opposite to the vacancy shrinks. Hence, O_a, O_b and O_g become the three closest O ligands on the defective doped

45

La$_2$O$_3$(0001) surfaces. As is shown in Figure 2(b), the X-O$_g$ bond length on the defective La$_2$O$_3$(0001) surfaces is usually shorter than the one on the regular surfaces, while the X-O$_{e/d}$ distance increases in the presence of an oxygen vacancy. For the surface doped by Mo, the X-O$_g$ bond length slightly increase with the Mo dopant shifting up. Owing to the tendency of the dopants towards forming three short bonds to O$_{a/b}$ and O$_g$ and two longer ones to O$_{e/d}$, the dopants will simultaneously conduct the horizontal and vertical displacement, which slightly increases or decreases the bond lengths between the dopants and the surface O$_{a/b}$ atoms, namely d(X-O$_{upper}$) in Figure 4.2(b). Again, the f-block dopants and La itself lead to the smallest deformation of the surface geometry with the formation of the oxygen vacancy in comparison to s-block and d-block dopants.
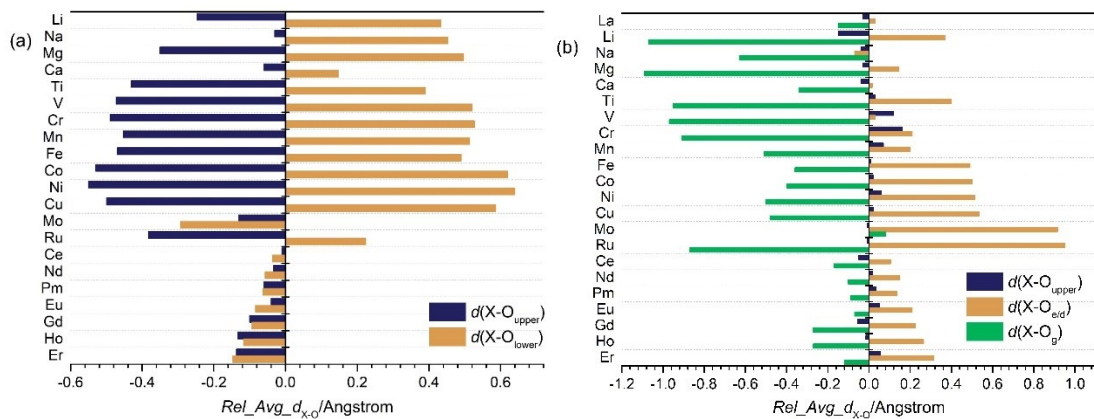
Figure 4.2. Relative differences in bond lengths between heteroatom dopants (X) and the surrounding O atoms calculated by subtracting the corresponding bond lengths (a) on a regular undoped La$_2$O$_3$(0001) surface from those on doped La$_2$O$_3$(0001) surfaces, and (b) on a regular La$_2$O$_3$(0001) surface from those on defective La$_2$O$_3$(0001) surfaces with the same doping heteroatom. O$_{upper}$ and O$_{lower}$ denote three surface or subsurface O atoms near the dopant site, respectively. X-O$_{upper}$/O$_{lower}$/O$_{e/d}$/O$_g$ denotes the bond lengths between dopants and the corresponding adjacent O atoms.

46

4.2 The Lewis Acidity of the Surface Metal Atoms

4.2.1 The adsorption energy on the d-block dopants

Catalytic activity of oxide surfaces is often related to their Lewis acidity or basicity. For example, Lewis acidity/basicity of REOs was proposed to have an effect on the C-H activation of methane, the rate-limiting step in the oxidative coupling of methane reaction.[57, 60, 135] As will be discussed in detail below, oxide surfaces may act as either Lewis acids or Lewis bases, depending on the nature of the active site and the adsorbate molecule. The adsorption energy of a chosen probe molecule with electrophilic or nucleophilic properties can serve as a measure of the Lewis acidity/basicity of the surface. The higher the Lewis acidity of the surface, the more likely it is that a molecule possessing lone pairs of electrons will adsorb to it more strongly. Likewise, Lewis basicity is a measure of the ability of a surface to donate electrons to molecules or ions. The more electron-donating ability the surface has, the stronger the adsorption of electron-deficient molecules on that surface. In this work, we selected NH_3 showing Lewis basicity to measure the Lewis acidity of the cationic sites of doped $La_2O_3(0001)$ surface distinguishing between the La atoms and the dopants. The adsorption energy of NH_3 was calculated as $E_{ads} = E(\text{adsorption complex}) - E(\text{surface}) - E(NH_3)$. Accordingly, a more negative value of the adsorption energy indicates stronger adsorption, and hence stronger Lewis acidity of the adsorption sites.

In addition to the adsorption energy of selected probe molecules, we explored the d-band center (of the metal) as a possible electronic structure descriptor related to the Lewis acidity of the surface. A well-known d-band model developed for transition metal surfaces correlated to the adsorption strength of adsorbates to the d-band center, which depends on the nature of a metal and its d-shell filling.[136] In this work, we applied the d-band center model to transition metal oxides and anticipated a relationship between this simple descriptor of the electronic structure and the Lewis acidity of cations on pristine and doped $La_2O_3(0001)$. The d-band center (ε_d) was calculated

according to equation (4.1) based on the partial density of states (pDOS) projected onto d orbitals of the metal atoms, as follows

$$\varepsilon_d = \frac{\int_{-\infty}^{\infty} n_d(\varepsilon)\varepsilon d\varepsilon}{\int_{-\infty}^{\infty} n_d(\varepsilon) d\varepsilon} \qquad (4.1)$$

where ε represents the energy, and $n_d(\varepsilon)$ denotes the electron density of d orbitals in the DOS plots. However, the original Hammer-Nørskov model for the d-band center did not consider spin-polarization. Therefore, a spin-averaged d-band center model was developed for spin-polarized calculations, with equation (4.2) replacing equation (4.1), shown as follows,[137]

$$spin\ averaged\ \varepsilon_d = \sum_\sigma \frac{f_\sigma \varepsilon_{d\sigma}}{\sum_\sigma f_\sigma} \qquad (4.2)$$

where σ represents the possible spin configurations while f_σ indicates the fractional filling of the p or d states with spin σ, which is calculated by integrating DOS below or above the Fermi level.

The d-band center of a transition metal typically exhibits a linear correlation with the molecular adsorption energy at a transition metal surface.[138-139] However, the applicability of the d-band center model to adsorption on transition metal oxides is less straightforward because the M-O bonding (M stands for metal) significantly alters the symmetry of d-orbitals of the metal atoms. Calle-Vallejo et al.[140] proposed the number of valence electrons remaining on the metal atom upon oxidation (termed "outer electrons") as a descriptor for adsorption on transition metal oxides. Kitchin et al.[141] expressed the adsorption energies on doped TiO_2 by combining the adsorption energy on the pure oxide of the dopant and perturbations caused by changing its neighboring metal cations and by incorporating strain effects. They further established a relationship between the adsorption energies on the doped transition metal oxides and the center of the t_{2g} d-band, which is derived from the crystal-field splitting of d-orbitals. Both approaches make use of either the d-band of a specific symmetry or a combination of them, or the band filling rather than the band center position, to improve the correlation with the adsorbate adsorption.

Inspired by the above-mentioned d-band theory of transition metals, we attempted to find a simple descriptor of the electronic structure by correlating the d-band center position to the surface Lewis acidity/basicity of doped $La_2O_3(0001)$ surfaces. We performed calculations on the regular (without O vacancies) $La_2O_3(0001)$ surface doped by Ti, V, Cr, Mn, Fe, Co, Ni, Cu, Mo and Ru. The adsorption energies of NH_3 served to measure the Lewis acidity of the doping site. For the surfaces doped by Ti, one narrow filled state can be seen near the Fermi level, corresponding to the oxidation state of +3, and there is little overlap between the Ti$3d$ and N$2p$ bands after NH_3 adsorption on the surface (see Figure 4.3(a)). For the V dopant, we observe a larger overlap between the V$3d$ band (mainly d_{z2}) and N$2p$ band (see Figure 4.3(b)), corresponding to a more negative adsorption energy of NH_3 compared to the Ti dopant. Among the dopants, Ru shows the strongest adsorption of NH_3 on the doping site (Figure 4.4), in line with the largest overlap between the d-band of the dopant and the p-band of N atom (see Figure 4.3(d)).

However, the d-band center calculated for the complete d states of the dopants on the regular doped $La_2O_3(0001)$ surfaces shows little correlation with the adsorption energy of NH_3, as indicated in Figure 4.4(a). An interaction of NH_3 with the d-block metal dopants is mainly formed through the donation of lone-pair electrons from the N atom of NH_3 to the empty d-orbital of the dopant (of proper symmetry). This suggests that the band center of the unoccupied d states should be more reflective of the adsorption energy, which is corroborated by Figure 4.4(b). The d-block dopants on $La_2O_3(0001)$ form bonds with six surface/subsurface O atoms, resulting in the splitting of the d-orbitals into groups based on their spatial orientations. Let us consider the $La_2O_3(0001)$ surface doped by Fe as an example (Figure 4.3(c)). The d-orbitals split in the crystal field into three symmetry-equivalent groups, with the d_{z2} orbital having the lowest energy, followed by the group consisting of the d_{xz} and d_{yz} orbitals, and the group with the highest energy comprised of the d_{xy} and d_{x2-y2} orbitals. The d_{z2} orbital plays a major role in the bonding mechanism of NH_3 on the doped $La_2O_3(0001)$ surfaces by accepting

electrons from the $2a_1$ orbital of NH_3, as evidenced by a substantial overlap between the d_{z2} orbital of the dopants and the $2p$ orbital of the N atom on the doped surfaces after adsorbing NH_3 (Figure 4.3). This is further demonstrated by the linear relationship between the spin-averaged d-band center of the unoccupied d_{z2} state of the dopants and the adsorption energy of NH_3 on the dopant atoms as seen in Figure 4.4(c).
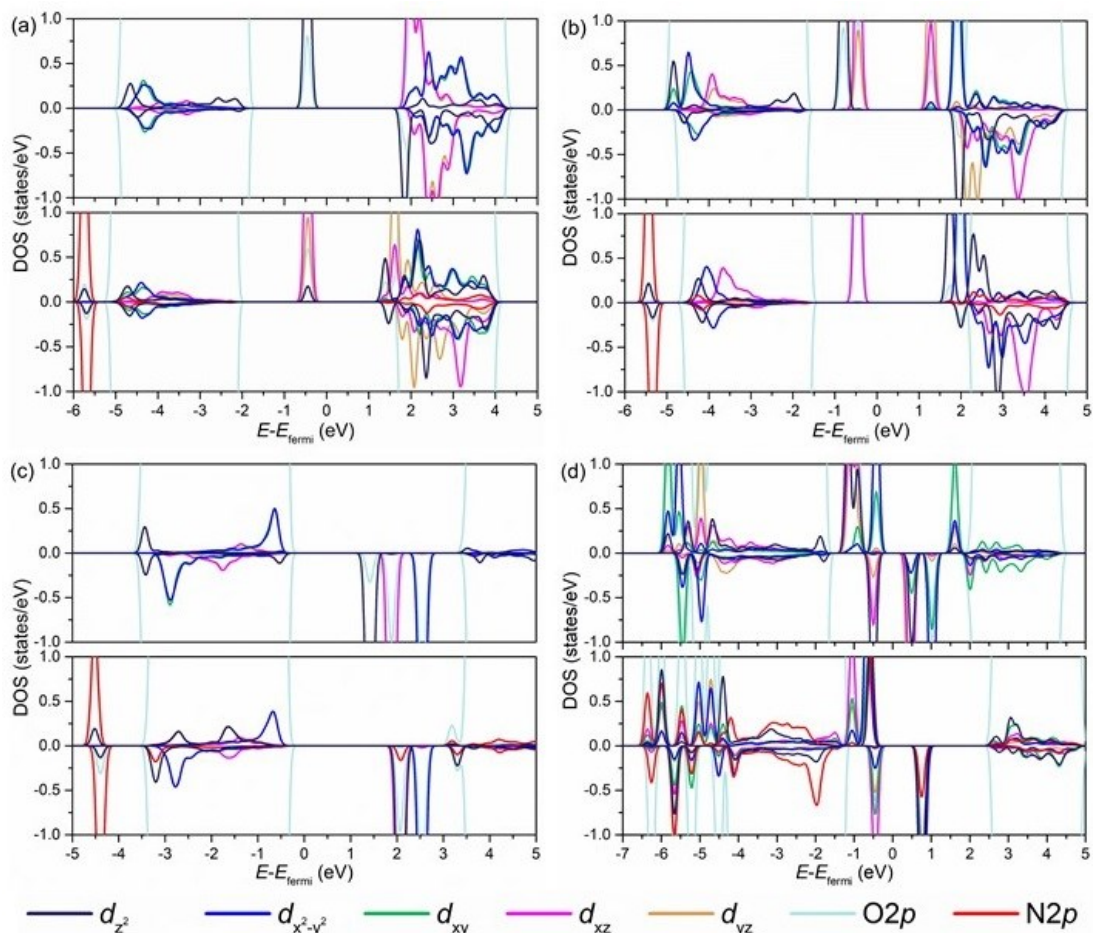
Figure 4.3. The partial density of states (PDOS) projected onto d orbitals of (a) Ti, (b) V, (c) Fe and (d) Ru doped on the regular La_2O_3(0001) surfaces with or without the adsorption of NH_3, as well as the PDOS of N $2s$ and $2p$ orbitals on the doped surfaces after adsorbing NH_3.
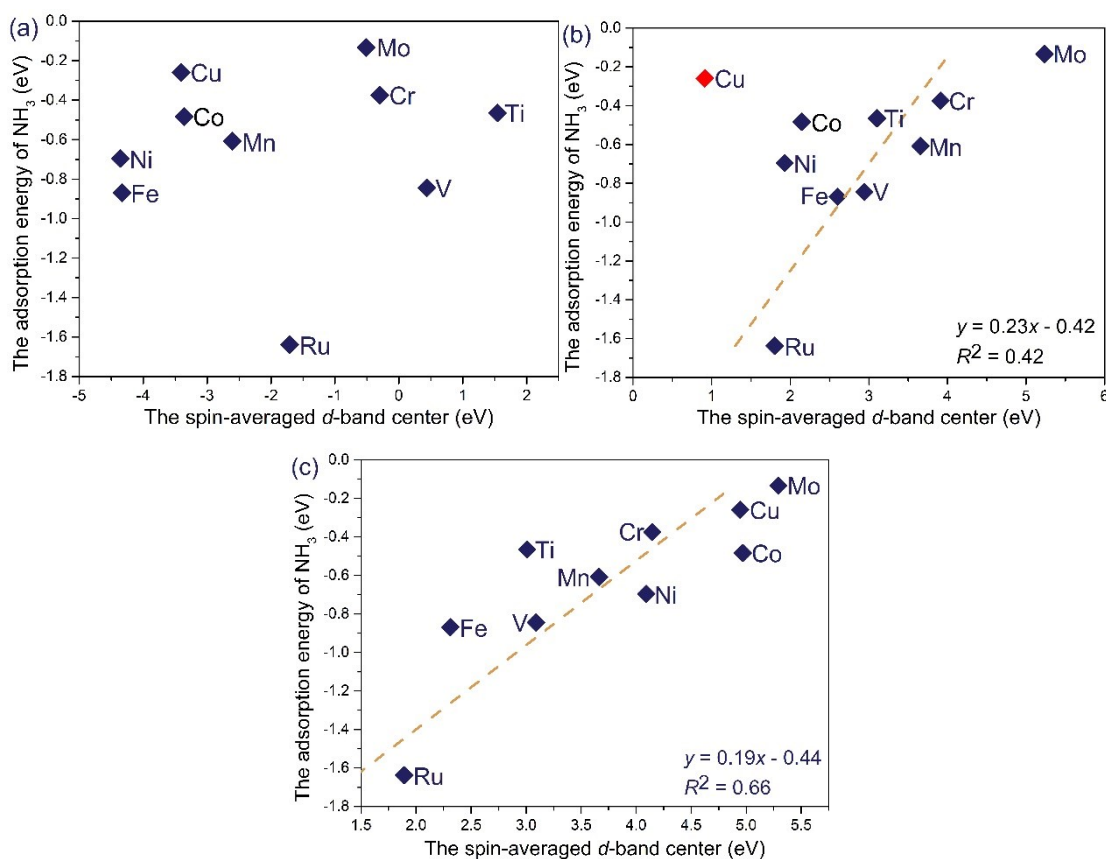
Figure 4.4 The scatter diagram for the regular $La_2O_3(0001)$ surfaces doped by various d-block heteroatoms combining the adsorption energy of NH_3 on the dopants with the spin-averaged band center of (a) the complete d states, (b) the unoccupied d states, or (c) the unoccupied d_{z2} states of the doping heteroatoms. The point labelled in red color in panel (b) was not considered in the linear fitting.

4.2.2 The d-band center of the surface lanthanum atoms

To evaluate the Lewis acidity of the surface lanthanum atoms, we calculated the adsorption energy of NH_3 and CO on the regular $La_2O_3(0001)$ surfaces doped by Ti, V, Cr, Mn, Fe, Co, Ni, Cu, Mo, Ru and Ce at La_i sites. We found that the adsorption energies of both NH_3 and CO on La_i sites were almost unaffected by the presence of the dopants, with each energy equaling around -0.72 eV and -0.32 eV, respectively (Figure 4.5). The relatively weak adsorption is mainly due to the high position of the empty d band of La atoms, which lies too high in energy to accept electrons from NH_3 and CO. The high energy of the empty d-band is reflected by the high position of the unoccupied d-band center. The d-band center was calculated in two different ways -

with the Fermi level or the $O2p$ valence band maximum (VBM) chosen as the zero of energy. By selecting the Fermi level as the zero energy, the $La5d$ band center relative to the Fermi level captures the effect of the filled states contributed by the doping heteroatoms (which shift the Fermi level toward the conduction band), while the latter approach only reflects the relative position of the $La5d$ band to the $O2p$ band. As seen in Figure 4.5, the d-band center relative to $O2p$ VBM remains unchanged with the incorporation of dopants, in line with the only slightly varied adsorption strength of the probe molecules, NH_3 and CO on the surface La atoms. The Lewis acidity of the surface La atoms is thus hardly affected by the dopants. Nonetheless, the spin-averaged unoccupied d-band center of the surface La atoms at La_i site relative to the Fermi level exhibits a marked fluctuation of up to 2.0 eV with the incorporation of d-block dopants (see Figure 4.5). This indicates that the d-band center model relative to the Fermi level could give us further insights into the effect of heteroatoms on the surface properties of $La_2O_3(0001)$ in addition to the Lewis acidity of the surface La atoms.
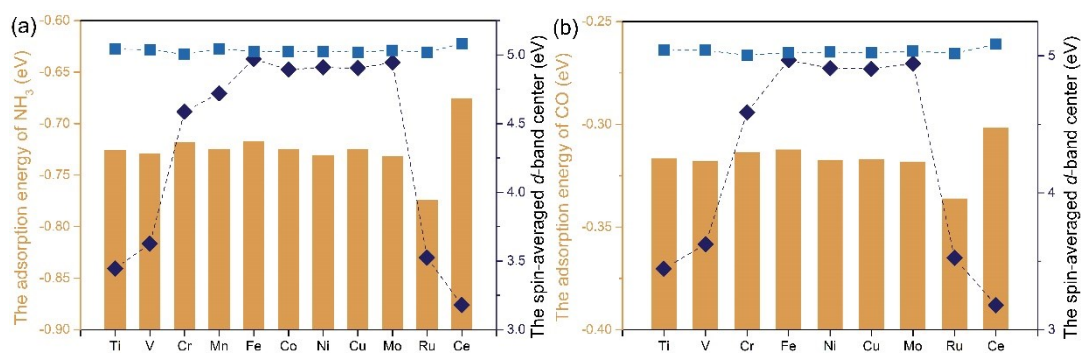
Figure 4.5. The adsorption energy of (a) NH_3 or (b) CO on the La_i site and the spin-averaged band center of the unoccupied d band of the specific La atom at La_i site on the regular $La_2O_3(0001)$ surfaces doped by Ti, V, Cr, Mn, Fe, Co, Ni, Cu, Mo, Ru and Ce. In the calculations of the d-band center, the zero energy was chosen as the Fermi level (dark blue diamonds) or the $O2p$ valence band maximum (light blue squares).

To investigate the impact of dopants and oxygen vacancies on the surface properties of $La_2O_3(0001)$, we selected a variety of s-block, d-block and f-block heteroatoms to dop the regular (without oxygen vacancy) and defective (with oxygen vacancy) surfaces.

Considering the sensitivity of the d-band center (relative to the Fermi level) to surface modifications through dopants, we calculated the spin-averaged d-band center of the complete or unoccupied d states. This was done for all surface La atoms (La$_{surface}$) and separately for La atoms located at La$_i$ or La$_{ii}$ sites. Figure 4.6(a) demonstrates that the variation of the d-band center due to dopants remains unchanged whether we consider the complete or only the unoccupied La$5d$ states on the regular La$_2$O$_3$(0001) surface. Both the complete and unoccupied La$5d$ states show a similar dependence on the nature of the dopants. The unoccupied d-band center is raised up by about 1.5 eV compared to the complete La$5d$ band. This correlation is also seen for the defective doped La$_2$O$_3$(0001) surfaces, as illustrated in Figure 4.6(b). The strong correlation is mainly attributed to the almost empty $5d$-band of trivalent La atoms, as seen in Figure 4.7.

On the regular La$_2$O$_3$(0001) surface, the d-band center lies at 5.0 eV for the surface La atoms (La$_{surface}$). The surfaces doped by Ti, V, Ru and Ce show a considerable shift in the position of the d-band center (Figure 4.6(c)). According to the d-band theory of Hammer and Nørskov, if the band is less than half filled, narrowing the band induces a downward shift of the d-band center. Therefore, a distortion of the surface geometry may have a significant effect on the position of the d-band center. However, the La$5d$ band is almost empty and its unoccupied states are at high energy. This implies that the position of the empty state relative to the Fermi level, rather than the band width, determines the d-band center. Hence, the large down-shift of the d-band center of the surface La atoms, observed for the surfaces doped with Ti, V, Ru and Ce (Figure 4.6(c)) shall be mainly attributed to a large shift of the Fermi level from just above the O$2p$ band toward the conduction band, further inducing a change in the position of the La$5d$ band relative to the Fermi level, with the band width remaining largely unchanged (see Figure 4.7(a)). The shift of the Fermi level results from the appearance of one or more narrowly filled states in the band gap contributed by the d band of the dopants (see the example of Ti in Figure 4.7(a)). The extra electrons will be residing in the d orbitals of the high-valence dopants after the dopants bind to the adjacent O atoms lying higher in

energy than the O2p valence band. The surface La atoms were divided in two categories: La$_i$ and La$_{ii}$, depending on their proximity to the doping site. As seen in Figure 4.6(c), the spin-averaged d-band centers for La atoms in both categories show similar behavior with respect to the type of dopant.

Next, the d-band center of La atoms on the defective undoped La$_2$O$_3$(0001) surface was studied. The spin-averaged d-band centers of both the unoccupied d states of the surface La atoms (La$_{surface}$) and the surface La atoms located at La$_i$, La$_{ii}$ or La$_{iii}$ sites (defined according to their proximity to the doping site and to the oxygen vacancy) were calculated. Due to the irreducible nature of trivalent La cations, the two extra electrons left by the formation of an oxygen vacancy remain localized in the center of the cavity. This is evidenced by the appearance of two narrow filled states, located close to the conduction band, beneath the Fermi level. The two electrons of the vacancy are rather weakly bound, thus can be easily donated, which accounts for their high energy close to the bottom of the conduction band (Figure 4.7(b)). Consequently, the formation of a vacancy causes the Fermi level to move from the top of the O2p valence band to the position close to the bottom of the conduction band (Figure 4.7), resulting in a downward shift of the d-band center of La atoms (to 1.7 eV) compared to the position (5.0 eV) on the regular undoped surface (Figure 4.6 (c) and (d)).

Note that even on the undoped La$_2$O$_3$(0001) surface, the creation of an oxygen vacancy results in different d-band centers for the surface La atoms located at the La$_{surface}$, La$_i$, and La$_{ii}$ sites. The La$_{iii}$ atom closest to the oxygen vacancy has the lowest d-band center at 1.5 eV, while the La$_i$ atom close to the dopants and the La$_{ii}$ atom far from the dopants and from the vacancy, have higher d-band centers of around 1.7 eV. However, the variation of the d-band centers of La$_i$, La$_{ii}$ and La$_{iii}$ with respect to doping with various heteroatoms remains similar to that of the La$_{surface}$ atoms (Figure 4.6(d)).
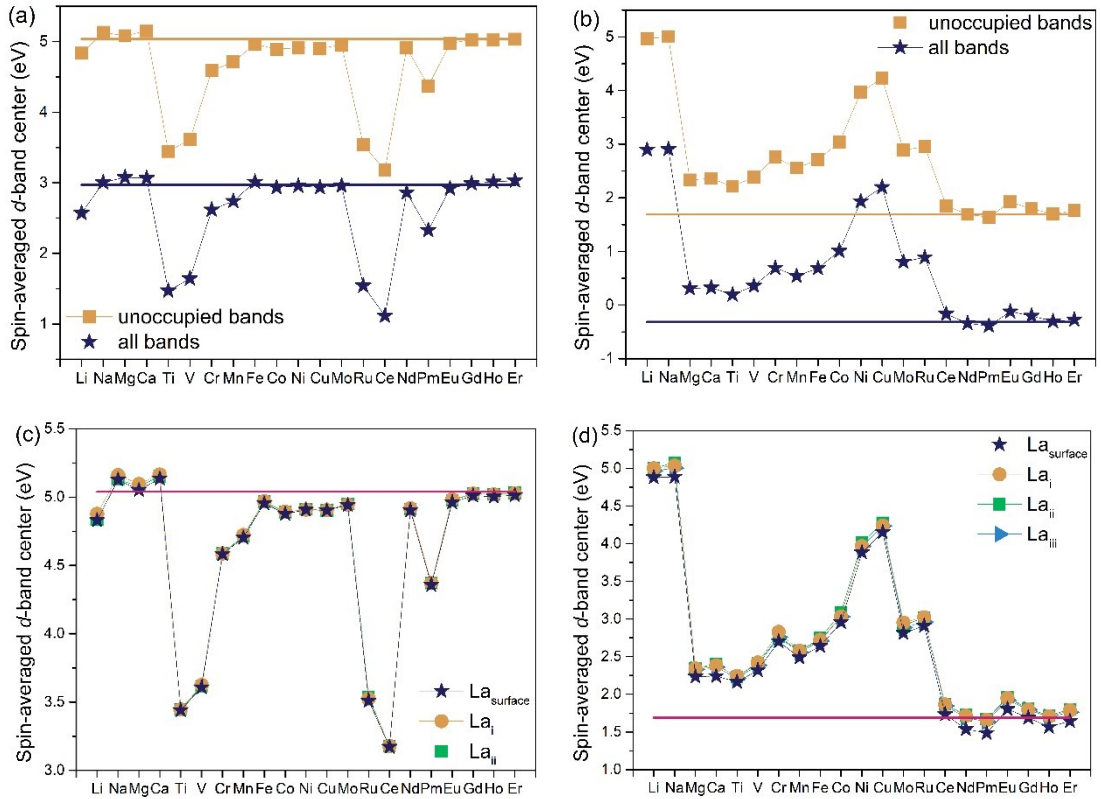
Figure 4.6. The comparison between the complete and unoccupied bands used to calculate d-band centers of the surface La atoms on the (a) regular or (b) defective doped $La_2O_3(0001)$ surface by various doping heteroatoms. The spin-averaged d-band centers of the surface La atoms ($La_{surface}$), and the single La atom located at La_i or La_{ii} or La_{iii} site on the (c) regular or (d) defective $La_2O_3(0001)$ surface doped by various heteroatoms. The horizontal line denotes the d-band center of the $La_{surface}$ atoms on the undoped $La_2O_3(0001)$ surface.

The incorporation of heteroatoms into the $La_2O_3(0001)$ surface has a major impact on the redistribution of the extra electrons resulting from the formation of an oxygen vacancy. The Li and Na dopants, with regular oxidation state of +1, exhibit electron deficits after being incorporated into the surface, which is evident from the appearance of an empty acceptor state appearing as a small shoulder above the Fermi level (Figure 4.7(a)). These electron deficits can be perfectly compensated by the extra electrons from the oxygen vacancy, thus maintaining the Fermi level at the top of the $O2p$ valence band (Figure 4.7(b)), which corresponds to the high positions of the d-band center for such doped surfaces (Figure 4.6(d)). The divalent s-block dopants, Ca and Mg only compensate for one electron left by the oxygen vacancy, thus forming a filled state in

the La5d-O2p band gap (Figure 4.7(b)). This filled state moves the Fermi level inside the band gap close to the La5d conduction band, resulting in a lower d-band center position compared to Li and Na (Figure 4.6(d)). In contrast, d-block dopants with variable oxidation states can accept the extra electrons to their vacant d-orbitals (lying close in energy to the O2p VBM) and thus cause the Fermi level to stay close to the O2p VBM and the La5d band to shift to a high energy relative to the Fermi level on the defective doped La$_2$O$_3$(0001) surface. Generally, low-valence dopants (Cu, Ni) tend to cause a larger down-shifting of the Fermi level than the high-valence dopants. For example, Ti (high-valence) creates two filled states above the O2p valence band, which puts the d-band center in a similar position to the defective undoped surface (Figure 4.6(d) and 4.8(b)), whereas Cu (low-valence) shifts the Fermi level close to the O2p valence band, similar to the Li dopant (Figure 4.7(b)). Furthermore, f-block heteroatoms, which are chemically similar to La atoms, cause almost no change to the d-band center compared to the defective undoped surface.
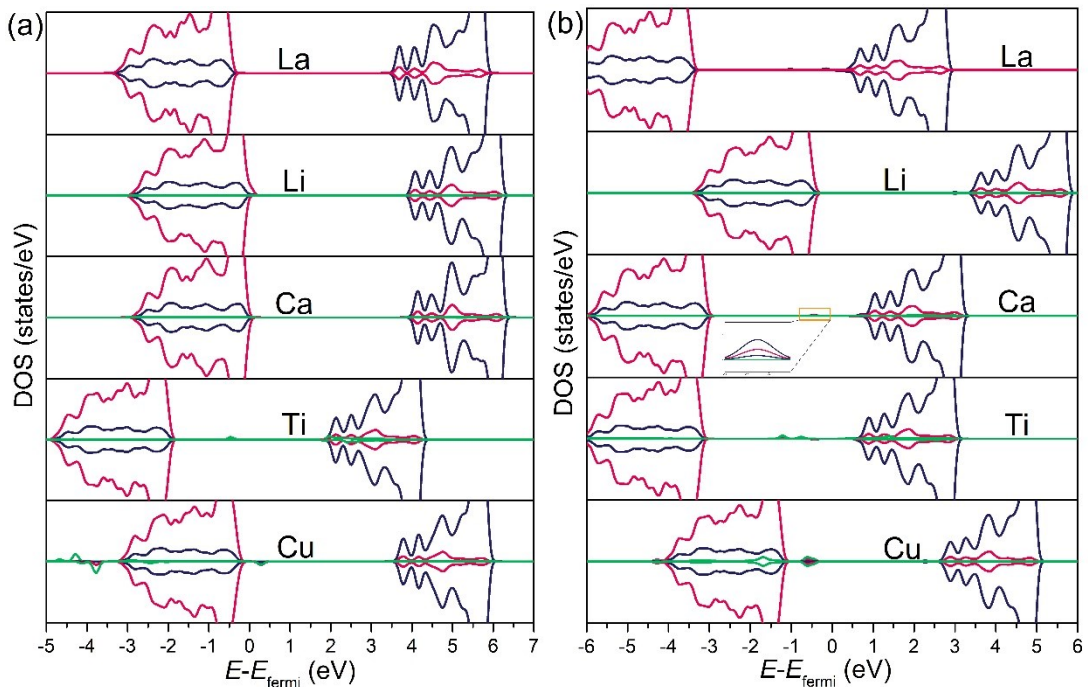
Figure 4.7. The local density of states (LDOS) of the La (in dark blue), O (in red) and dopant (in green) atoms on the (a) regular or (b) defective La$_2$O$_3$(0001) surface without doping or doped with Li, Ca, Ti and Cu.

4.3 The Lewis Basicity of the Surface Oxygen Atoms

To assess the Lewis basicity of doped $La_2O_3(0001)$ surfaces, we calculated the adsorption energy of CO_2 on the regular $La_2O_3(0001)$ surfaces doped by Ti, V, Cr, Mn, Fe, Co, Ni, Cu, Mo, Ru and Ce at the O_i site. Different from the adsorption energy of NH_3 and CO on La atoms, the adsorption energy of CO_2 on O_i atom was calculated by $E_{ads} = E(\text{surface}) + E(CO_2) - E(\text{adsorption complex})$, where a more positive energy corresponds to stronger adsorption strength in order to keep consistency with the p-band center. The $O2p$-band center can be calculated as the centroid of the projected density of $O2p$ states relative to Fermi level using Equation (4.1-4.2) with $La5d$ bands replaced by $O2p$ bands. Shao-Horn et al.[142-144] have used this descriptor to analyze the OER activity of perovskites, and to discuss the metal-ligand bonding, including the mixing between the O p-band and the d-band of metal atoms. Additionally, the O $2p$-band center has been developed as a descriptor of the reactivity (such as the deprotonation of the adsorbed OH) of surface oxygen atoms on the kinked $RuO_2(121)$ surface.[145] We calculated the spin-averaged p-band center for the occupied $O2p$ states by summing up both spin-up and spin-down p-band centers weighed by the band filling of the corresponding spin configuration.

As shown in Figure 4.8(a), the adsorption energy of CO_2 on O_i atom can be affected by the presence of dopants, varying from 0.68 eV to 1.32 eV. The p-band center of the surface O atoms was calculated by taking Fermi level or the $O2p$ VBM as the reference point of zero energy. Both p-band centers exhibit a similar variation trend with the doping of heteroatoms, with a large deviation from the undoped surface for the surfaces doped by Ti, V, Ru and Ce. This is attributed to the large shift of the Fermi level on the regular $La_2O_3(0001)$ surfaces doped by Ti, V, Ru and Ce (Figure 4.7(a)), as previously discussed in relation to the d-band center of the surface La atoms on the same surfaces (Figure 4.5). As in molecular systems, where the location of the highest occupied molecular orbital is related to the Lewis basicity of these systems, the band center of the occupied $O2p$ states can serve as a measure of the Lewis basicity of the surface O

57

atoms. A higher *p*-band center implies stronger Lewis basicity, as it indicates that the electrons in the O2*p* orbitals are closer to the Fermi level, and thus have the ability to donate electrons more easily. The *p*-band center indeed shows a correlation to the adsorption energy of CO_2 regardless of whether one refers to the Fermi level or the O2*p* VBM. The inconsistency for some of the dopants might be due to the fact that the adsorption energy of CO_2 does not only depend on the surface O site, as two oxygen atoms of CO_2 also interact with the adjacent surface La atoms.
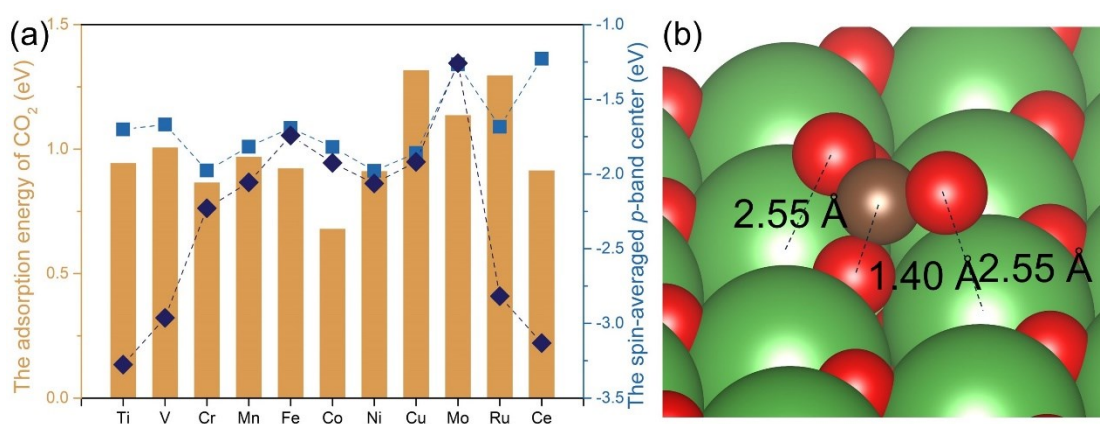
Figure 4.8. (a) The adsorption energy of CO_2 on the O_i site and the spin-averaged band center of the occupied *p* band of the specific O atom at O_i site on the regular $La_2O_3(0001)$ surfaces doped by Ti, V, Cr, Mn, Fe, Co, Ni, Cu, Mo, Ru and Ce. In the calculations of *p*-band center, the zero energy was chosen as either the Fermi level (dark blue diamonds) or the O2*p* valence band maximum (light blue squares). (b) The adsorption geometry of CO_2 with the C atom binding on the O_i site on the regular undoped $La_2O_3(0001)$ surface. La atoms are shown in green color, O atoms in red color, and the carbon atom in grey color.

To investigate the effect of the dopants and oxygen vacancies on the surface properties of $La_2O_3(0001)$, we calculated the spin-averaged *p*-band center for doped and undoped $La_2O_3(0001)$ surfaces with and without oxygen vacancies, taking the Fermi level as the zero energy. We compared the *p*-band center calculated for the complete *p*-band to the occupied *p*-band of the surface O atoms on the regular or defective $La_2O_3(0001)$ surfaces doped by various heteroatoms. Figures 4.9(a) and (b) demonstrate that the band center of the occupied *p*-band is shifted down relative to the complete *p*-band by an

almost constant amount of around 0.5 eV, while the variation of both electronic structure descriptors due to doping is remarkably similar.

We considered two types of surface O atoms: O_i or O_{ii}, located close to or far from the doping site, at the respectively, and collectively denoted as $O_{surface}$. As displayed in Figure 4.9(c), the p-band center of the surface O atoms is at about -1.3 eV for the regular undoped La_2O_3(0001) surface. The influence of dopants on the p-band center of the surface O atoms is similar to the effect on the d-band center of the surface La atoms, as seen in Figure 4.6. This is attributed to the change of the Fermi level caused by the dopants. The dopants with a higher regular oxidation state than La cation force the Fermi level to the top of the filled d states of the dopants, resulting in a lower position of the p-band center relative to the regular undoped surface, as shown for dopants, such as Ti, V, Ru and Ce in Figure 4.7(a) and 4.9(c).

The surface oxygen atoms located at the O_i (close to the doping site) and O_{ii} site (far from the doping site) display a similar variation in the positions of their p-band centers on the regular doped La_2O_3(0001) surfaces. However, there is a slight difference between the two surface O atoms. The addition of d-block heteroatoms causes a larger downshift of the p-band center for the O_i atom in comparison to the O_{ii} atom, while the opposite occurs when s-block heteroatoms are present, leading to a higher p-band center of the O_i atom compared to the O_{ii} atom (Figure 4.9(c)).

On the defective doped La_2O_3(0001) surfaces, the formation of an oxygen vacancy causes the p-band centers of $O_{surface}$, O_i and O_{ii} to become more negative compared to the regular La_2O_3(0001) surface, due to the two extra electrons left by the removal of the surface oxygen atom. These two electrons occupy a defect state in the La5d-O2p band gap, thus causing the Fermi level to shift upwards. The p-band center of $O_{surface}$ atoms decreases from -1.3 eV on the regular undoped surface to -4.6 eV on the defective undoped surface (Figure 4.9(c) and (d)). For most dopants, excluding those of the f-block, the p-band center on the defective doped La_2O_3(0001) surface shifts upward in energy, relative to the defective undoped surface, as a result of a Fermi level shift

59

caused by dopants completely or partially "absorbing" the extra electrons from the O vacancy. Specifically, s-block dopants increase their oxidation state from +3 to +1 or +2, whereas the d-block dopants increase their oxidation state to +1, with the extra electrons occupying their d-orbtals. The f-block dopants having the same trivalent state as La atoms cause the p-band center of the surface O atoms to remain almost unchanged. The p-band centers of O_i, O_{ii} and $O_{surface}$ atoms on the defective doped $La_2O_3(0001)$ surfaces exhibit a similar trend to the d-band center of La atoms on the same surface when exposed to dopants, as illustrated in Figure 4.6(d) and 4.9(d).
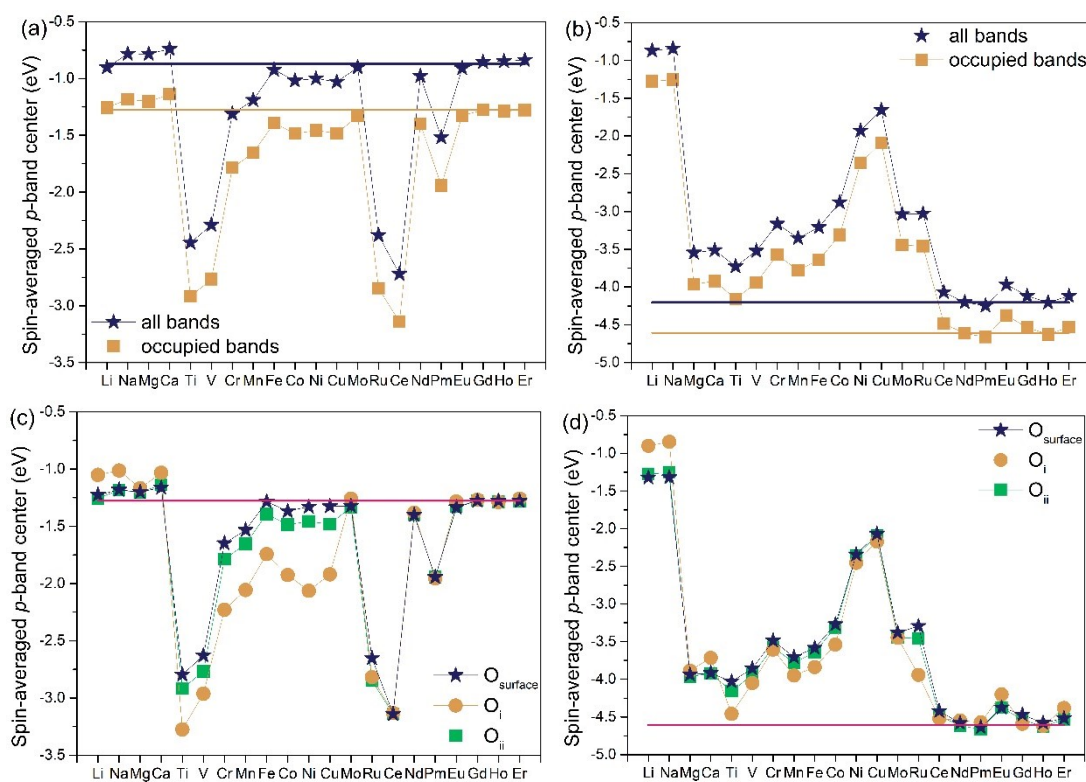
Figure 4.9. The comparison between the complete and occupied bands used to calculate p-band centers of the surface O atoms on the (a) regular or (b) defective $La_2O_3(0001)$ surface doped by various heteroatoms. The p-band centers of the surface O atoms, and the single O atom located at the O_i or O_{ii} site on the (c) regular or (d) defective $La_2O_3(0001)$ surface doped by various elements. The horizontal line denotes the p-band center of the surface O ($O_{surface}$) atoms on the undoped $La_2O_3(0001)$ surface.

Chapter 5 Surface Reducibility and its Relationship to *d*- or *p*-Band Centers of Doped La$_2$O$_3$(0001) Surfaces

5.1 Surface Reducibility of Doped La$_2$O$_3$(0001)

The formation energy of an oxygen vacancy can be regarded as a measure of surface reducibility, as it reflects the ability to release one surface oxygen atom from the surface. This tendency to release oxygen atoms is especially critical for oxidation reactions obeying the Mars-van Krevelen mechanism, where surface oxygen atoms directly participate in the reaction via binding to the adsorbate, making the ease of forming an oxygen vacancy a crucial factor for the reaction. Consequently, the oxygen vacancy formation energy is a key descriptor that captures both the reactivity and the surface reducibility.
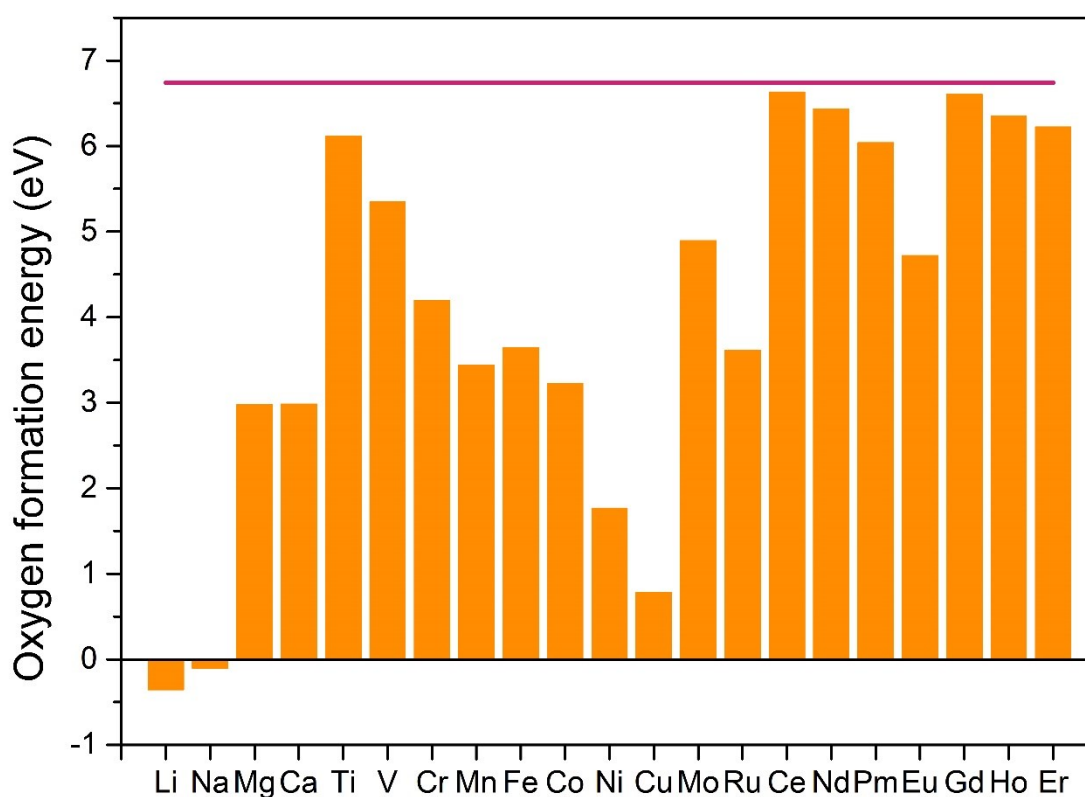
Figure 5.1. Oxygen vacancy formation energy (eV) for the La$_2$O$_3$(0001) surfaces doped by various heteroatoms. The top horizontal line represents the oxygen vacancy formation energy of the undoped La$_2$O$_3$(0001) surface.

We have calculated oxygen vacancy formation energies on the doped or undoped $La_2O_3(0001)$ surfaces. As seen in Figure 5.1, the formation of an oxygen vacancy on the undoped $La_2O_3(0001)$ surface results in a high vacancy formation energy of 6.7 eV, which is comparable to the *d*-band energy and to the band gap of La_2O_3. This high energy is predominantly due to the irreducibility of the lanthanum atoms. When an oxygen vacancy is formed, two extra electrons are left on the surface, which in general could either spread over the adjacent surface atoms, or could be localized on the metal atoms reducing them, or could be trapped in the vacancy site. However, due to the high energy of the empty states for La_2O_3, it is very difficult for the extra electrons to occupy the empty bands, resulting in the difficulty of changing the oxidation state of La atoms. This forces the extra electrons to localize in the vacancy site, where they are only weakly bound, therefore this state has a high energy close to the top of the conduction band, which explains the observed large oxygen vacancy formation energy.

The incorporation of doping heteroatoms in the $La_2O_3(0001)$ surfaces lowers the energy required for the oxygen vacancy formation, as shown in Figure 5.1. Owing to their different atomic radii and/or oxidation states, dopants modify the surface geometry in the vicinity of the doping site and induce a redistribution of the electrons of the atoms adjacent to the dopants, which further changes the capacity of the surface for releasing oxygen atoms. On the doped $La_2O_3(0001)$ surface, all of the considered doping heteroatoms are able to increase the surface reducibility to a various degree. Alkali metals (Li, Na) belonging to *s*-block elements give the largest promotion for oxygen vacancy formation owing to their low oxidation states (+1), where the release of the surface oxygen (in the form of O_2) changes from an endothermic process to an exothermic process. Although still endothermic, the oxygen vacancy formation energy is decreased dramatically for Mg, Ca dopants (to ~3 eV), and most of the *d*-block heteroatoms (to 3-4 eV) except for Ti (6.1 eV), V (5.3 eV), Ni (1.8 eV) and Cu (0.8 eV). Due to their similar chemical properties and atomic radii to La, all of the *f*-block dopants have a negligible impact on the oxygen vacancy formation energy.

5.2 Relationship Between Surface Reducibility and d- or p-Band Centers

As discussed in Chapter 4, the d- or p-band center relative to the Fermi level takes into account the filled d states of the dopants and their effect on the surface properties. Dopants with different stable oxidation states from La result in different distribution of their valence electrons after doping onto the $La_2O_3(0001)$ surface, which in turn can cause a shift of the Fermi level and change the d- or p-band center position of the surface La or O atoms relative to the Fermi level. Additionally, s- or d-block dopants may introduce vacant ("acceptor" states) in the band gap. These initially empty states readily accept electrons. To further explore the impact of the dopants on the formation of oxygen vacancies, we compared the d- or p-band center of the unoccupied La5d states of surface lanthanum atoms or of the occupied O2p states of oxygen atoms, respectively, with the oxygen vacancy formation energy to establish the relationship between them. As demonstrated by Figure 5.2 (a) and (b), the d-band center of the surface lanthanum or p-band center of oxygen atoms on the defective $La_2O_3(0001)$ surface, respectively, exhibits a linear relationship with the oxygen vacancy formation energy. Dopants from the s-block, with lower stable oxidation states than La, create an electron-deficient site surrounding them that is indicative of their higher propensity for accepting electrons than La. This electron-deficient site is capable of compensating partially or fully for the extra electrons introduced by the oxygen vacancy, thus promoting its formation. Although oxygen vacancy is usually considered a Lewis base, it is important to note that the facilitation of the oxygen vacancy formation by s-block dopants should be attributed to an electron donor-acceptor interaction instead of a Lewis acid-base interaction between the s-block dopant atom and the vacancy. This can be seen in Figure 4.7 (a), where the empty states near Fermi level are mainly contributed by the O2p band on the regular $La_2O_3(0001)$ surface doped by Li. The extra electrons from the vacancy will occupy these empty O2p states. Additionally, the Fermi level close to the O2p

VBM translates into a less negative p-band center of the occupied O2p states and a more positive d-band center of the unoccupied La5d states on the regular La$_2$O$_3$(0001) surface doped by s-block dopants (see Figure 5.2(a) and (b)). Next in line are the d-block dopants with variable oxidation states. The d-block dopants with a low oxidation state, such as Ni and Cu, are similar to the s-block dopants; however, the reverse is true for the d-block dopants with a high oxidation state, like Ti, V, and Ce. When these are used to dop a surface, filled d states appear in the La5d-O2p band gap, shifting the Fermi level close to the conduction band (Figure 4.7). As a result, the p- or d-band center shift downwards, while the oxygen vacancy formation energies increase on the surfaces doped by the d-block dopants with a high oxidation state in comparison to those doped by s-block or d-block dopants with a low oxidation state. The f-block dopants, which possess the same oxidation state (+3) as La atoms, have the least effect on the defect formation on the La$_2$O$_3$(0001) surface. Consequently, a linear relationship between the oxygen vacancy formation energy and the d- or p-band center can be seen on the defective doped surface. However, the d- or p-band center on the regular doped La$_2$O$_3$(0001) surfaces does not have a linear relationship to the energy of forming an oxygen vacancy, due to the absence of an oxygen vacancy and thus the lack of its effect on the maximum of the occupied states, i.e. the Fermi level.

In addition, we calculated the ratio between the O p-band center and La d-band center on the defective La$_2$O$_3$(0001) surface (denoted as O2p/La5d band center ratio) and related it to the oxygen vacancy formation energy. A less negative p-band center and a more positive d-band center lead to a less negative value of the O2p/La5d band center ratio, which usually correspond to the down-shifting of the Fermi level (determined by the position of the filled vacancy state) close to the O2p VBM and far from the La5d conduction band. It indicates that the doped surface exhibits electron-deficit property due to the (low-valence) dopants, inducing a lower oxygen vacancy formation energy than on the undoped La$_2$O$_3$(0001) surface. Hence, the O2p/La5d band center ratio (of the defective surface) reflects the position of the Fermi level relative to O2p VBM

which usually relates to the ease of the removal of one surface O atom, namely the surface reducibility. Given the simultaneous and concerted shift of the d- and p-band centers caused by dopants, a hyperbola-type fit can be established between the O2p/La5d band center ratio and the oxygen vacancy formation energy, as illustrated in Figure 5.2(c). We also tried to correlate the difference between the spin-averaged d-band center of the surface La atoms and p-band center of the surface O atoms to the oxygen vacancy formation energy. However, as previously noted, the positions of the d- and p-band centers shift in unison, approximately preserving the energy gap between them, which is close to the gap between the La5d CBM and O2p VBM energies, as well as the energy required to form an oxygen vacancy on the undoped $La_2O_3(0001)$ surface. Therefore, there is no linear relationship for the difference of the d- and p-band center and the oxygen vacancy formation energy as shown in Figure 5.2(d).

As seen in Figure 5.2, Li or Na dopants lead to the highest position of d- and p-band centers after the O vacancy formation, and simultaneously the smallest oxygen vacancy formation energy representing the strongest surface reducibility. This large modification to the surface properties due to Li or Na as dopants correlates with the high activity of Li/Na-doped lanthanum oxides in some oxidation reactions. For example, Baerns et al.[10] conducted a statistical analysis based on a database of already-obtained catalytic data of catalysts and found that lanthanide oxide doped with alkali or alkaline earth metal yielded one of the high-performance OCM catalysts. Furthermore, Li/Na-doped Sm_2O_3 achieved C2 (ethane and ethylene) yield of 22%, far exceeding the 10-12% yield of unpromoted La_2O_3, Sm_2O_3 and Nd_2O_3 catalysts.[11-12] Additionally, the TbO_x/n-MgO catalyst doped with Li or Na maintained a high CH_4 conversion (22.9%) and C2 selectivity (63.6%) even at a relatively low temperature (650°C).[146-147]
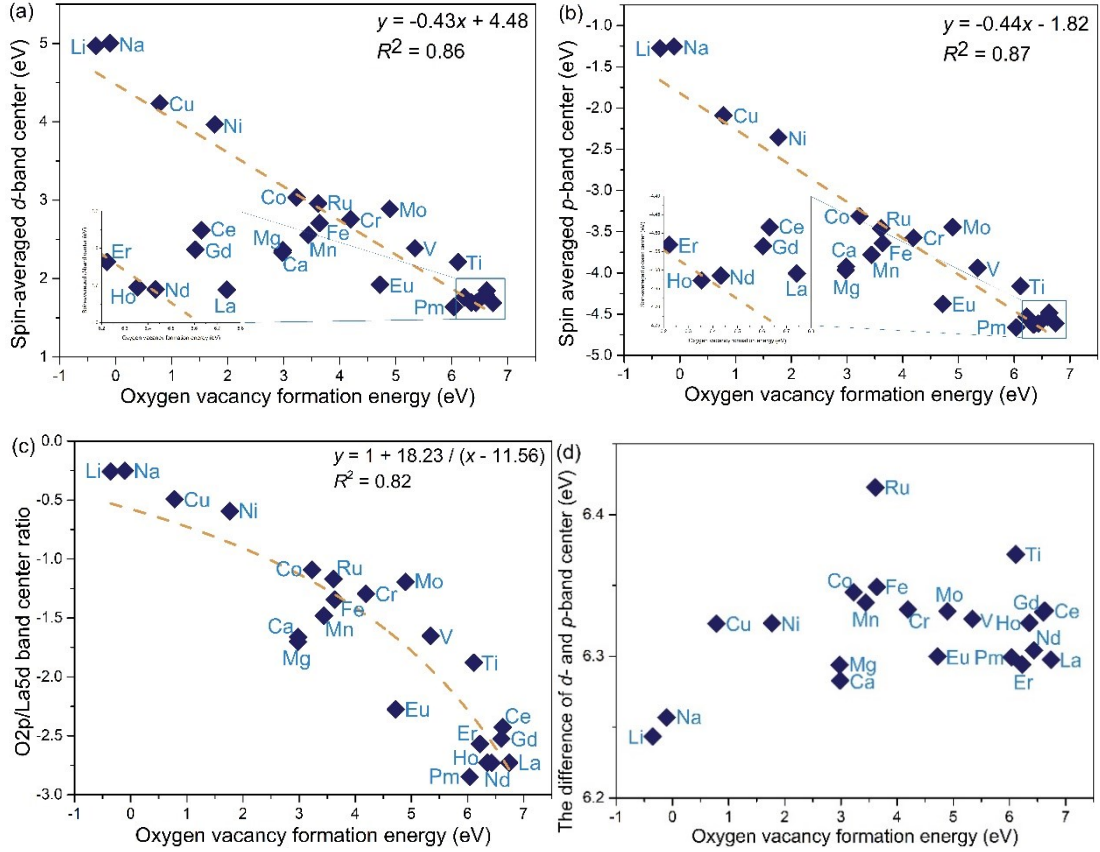
Figure 5.2. The scatter diagram for the doped defective La$_2$O$_3$(0001) surface by various doping elements combing the oxygen vacancy formation energy (eV) with (a) the spin-averaged d-band center, (b) the spin-averaged p-band center, (c) the spin-averaged O2p/La5d band center ratio, or (d) the difference between the spin-averaged d-band center of the surface La atoms and p-band center of the surface O on the same doped defective La$_2$O$_3$(0001) surfaces, where p- or d-band center was separately calculated for the occupied O2p states or the unoccupied La5d states.

Unlike Li and Na heteroatoms, Mg and Ca only cause a moderate increase in the d- and p-band centers of the defective La$_2$O$_3$(0001) surface and a slight reduction in the oxygen vacancy formation energy. With the exception of Ni and Cu, which have stable mono- and divalent valence states), other d-block metal atoms lead to a moderate shift of the d- and p-band centers and a slight increase in surface reducibility when compared to the defective undoped La$_2$O$_3$(0001) surface. In contrast, Ni and Cu dopants lead to a greater shift in the La5d or O2p states and a lower oxygen vacancy formation energy compared to Mg, Ca and other d-block metal atoms, making them more similar to Li and Na dopants. This suggests that the lanthanum surface doped by Cu and Ni elements

may have similar reactivity and potentially better surface stability than that doped by Li or Na atoms. Meanwhile, the *f*-block heteroatoms have the least effect on the surface geometry and the position of the Fermi level resulting in almost unchanged *d*- or *p*-band center and reducibility compared to the undoped $La_2O_3(0001)$ surface.

Chapter 6 CO Oxidation and O_2 Dissociation Assisted by a 1D Gold Oxide Chain on a Stepped Au Surface

Theoretical and experimental studies provide evidence that adsorbed O atoms on the stepped gold surfaces may self-organize to form linear ("one-dimensional") O chains with alternating Au and O atoms even at low O coverage,[85] while more abundant supply of O atoms via special pretreatment methods[148-152] or in molecular beam experiments[153-154] possibly promotes the formation of two-dimensional (branched) O chains on Au surfaces. Computational DFT-based studies also predicted the formation of "single" (consisting of linear –O–Au–O– units) and "double" (consisting of square shaped –AuO_4– units) O chains along the straight steps of stepped Au surfaces and their higher thermodynamical stability compared to adsorbed individual O atoms.[155-156] Owing to their thermodynamic preference, the idealized fully saturated O chains are expected to be less reactive than individually adsorbed O atoms on the gold surface. However, incomplete chains with O vacancies may be formed on the gold surface in real catalytic systems, which may enhance the adsorption and activation of adsorbates, such as CO and O_2 and further promote the reactivity of CO oxidation. CO oxidation is our model reaction, but in general, the same principles may apply to other oxidation reactions on Au surfaces. In this chapter, we selected the Au(221) surface as our model stepped surface with straight steps prone to formation of O chains along the steps (see Figure 6.1). In the following, using the Au(221) surface as a model, we discuss the energetics of O atoms chemisorption along the steps, the formation energy of single and multiple oxygen vacancies in the double chain, as well as present a systematic study of the oxygen chain's ability to bind the adsorbates, O_2 and CO, and to catalyze CO oxidation. The surface models chosen in this study contain a nanostructured 1D gold oxide, which also allows us to relate the described reactivity to gold nanoparticles supported on reducible oxides, such as ceria-supported gold nanoparticles[63-65] or inverse gold-supported reducible oxide nanoparticles[157] to some extent, where not only the gold

nanoparticle but also the oxide component is directly involved in the reactivity by contributing to activating dioxygen (O_2), and the reaction is believed to occur mainly at the boundary sites between the gold and the oxide components.[65, 157-159] Therefore, our model system discussed in this chapter uncovers a new facet of gold surface chemistry by forming self-organized nanostructured 1D surface oxide chains which probably play a notable role in the overall reactivity of gold-based catalysts.
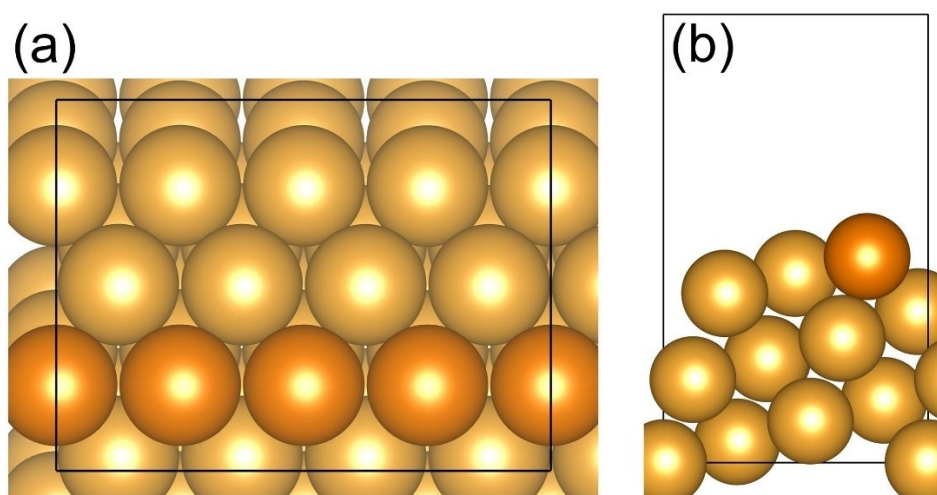
Figure 6.1. (a) Top view and (b) side view of the Au(221) surface model. Au atoms at the step edge are indicated by an orange color; the remaining Au atoms are shown in gold color.

6.1 Oxygen Chain Structure on the Au(221) Surface

6.1.1 The formation of oxygen chains on Au surfaces

In a related study by our group based on AIMD simulations, it was found that a single oxygen chain may form on the Au(321) surface with zig-zag shaped steps after the adsorption of the atomic O.[84] To deeper understand this self-organization process and to further investigate O_2 dissociation and CO oxidation on Au-based catalysts, we first calculated the adsorption energies of various numbers of oxygen atoms in chains of various stoichiometry on the steps of a Au(221) surface. The adsorption energy was

calculated by $E_{ads} = {^1\!/_N} \left[E(\text{adsorption complex}) - E(\text{surface}) - N * E(O) \right]$,

where $E(O)$ indicates the energy of one O atom treated as $\frac{1}{2}E(O_2)$, and N means the number of O atoms on the surface. As is shown in Figure 6.2, one individual O atom tends to adsorb at a 3-fold fcc site near the step edge by releasing the energy of -0.27 eV. Two O atoms located at the step edge prefer to form a linear -O-Au-O- chain. The adsorption energy per O atom slightly increases in absolute value to -0.29 eV (Figure 6.2(b)). A continuous increase in the number of O atoms leads to stronger adsorption per O atom until four oxygen atoms reaching the maximum of the adsorption energy, -0.32 eV (Figure 6.2(c) and (d)). With the chosen size of the unit cell, the four adsorbed O atoms constitute an infinite –(Au-O)- chain structure along the step edge on the Au(221) surface. This steady increase in the binding strength is at first glance surprising because usually repulsion and surface deformation lead to weakening of binding energy at a higher adsorbate coverage. The formed chain structure is stabilized by the strongly directional Au-O bonding within the chain. Similar stabilization of adsorbed O within chains was also found on Au(321) and Au(310) surfaces.[22, 29] As we continue to add more O atoms at the step edge, gradually forming a second chain in the opposite direction to the initial O chain, the adsorption strength per O atom initially weakens to -0.12 eV and then slowly increases in magnitude to -0.17 eV for a chain with only one O vacancy, although the adsorption remains exothermic (Figure 6.2 (e)-(g)). The weakening of the binding results from the growing electrostatic repulsion among the negatively charged O atoms at a high coverage and from the adsorbate-induced deformation of the Au surface. The resulting structures shown in Figure 6.2 (e)-(g) could be treated as an incomplete double O chain with oxygen vacancies as a whole. However, as the number of adsorbed oxygen atoms along the step edge on the surface increases to eight, a complete double –(Au-O)- chains structure (see Figure 6.2(h)) forms with the increased adsorption energy of -0.25 eV per O atom. The stability of the double oxygen chain structure is very close to that of short chains consisting of one or two oxygen atoms adsorbed along the step edge. Hence, the strong directional bonding interaction within the –(Au–O)– chain greatly enhances the stability of the chain even

in spite of the increasing repulsion among the O atoms. Therefore, we anticipate the formation and thermodynamic stability of the double oxygen chains on stepped Au surfaces if gold catalysts are exposed to a sufficiently strong oxygen source for a sufficient time in the experiment.

Figure 6.2. The adsorption energies (eV) per O atom and the corresponding geometries for O chains of various stoichiometry (1-8 O atoms) in a $p(4 \times 1)$ unit cell on the Au(221) surface. Au atoms at the step edge are indicated by an orange color; the remaining Au atoms are shown in gold color. O atoms are shown in red.
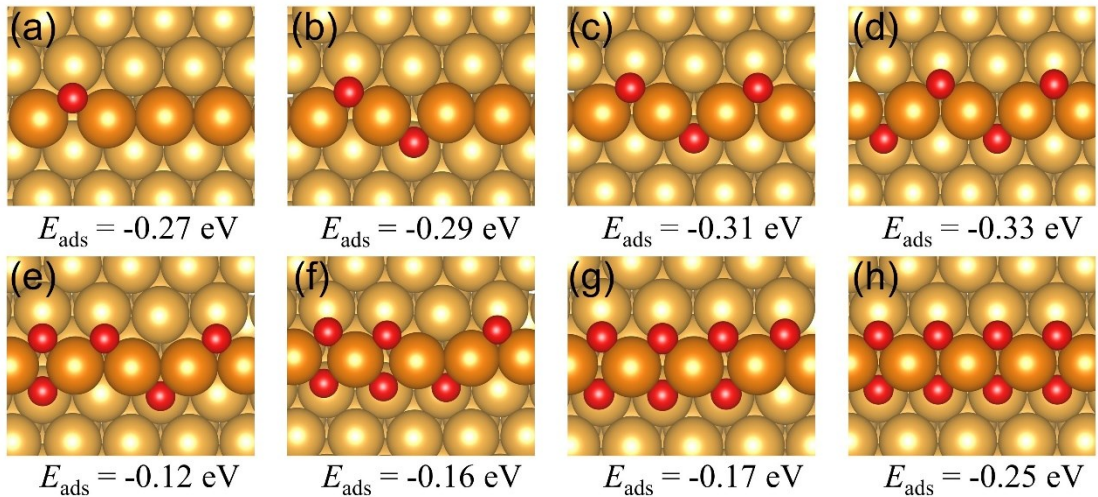
We further compared the projected density of states (PDOS) onto $O2s$, $O2p$ and $Au5d$ orbitals for several Au(221) surfaces with different types of O adsorption (see Figure 6.3). For one O atom adsorbing on the Au(221) surface, two rather broad resonances form near the top and near the bottom of the $Au5d$ band by the hybridization (mixing) between the $O2p$ and $Au5d$ orbitals (Figure 6.3(b)). A largely occupied anti-bonding state near the top of the valence band corresponds to a relatively weak Au-O bonding strength explaining the rather low adsorption energy (-0.27 eV, Figure 6.2(a)) of one O atom on the gold surface, even weaker than the adsorption (up to 0.8 eV) on the Cu(100) and Ag(100) surfaces without steps[160]. As a single –(Au-O)– chain forms on the surface, an enhanced hybridization of the $Au5d$ band with the $O2p$ band is achieved by the widened $Au5d$ band owing to the strong directional Au-O bonds within chains, and as

a result of this enhanced hybridization a new peak appears at the bottom of the Au5d

band (Figure 6.3(c)), which also indicates the stronger adsorption of O atoms on the Au

surfaces with the –(Au-O)– structures. With the formation of a double O chain on the

Au(221) surface, we observed a distinct bonding O2p state at the bottom of the Au5d

band and the partially unoccupied anti-bonding state at the top of it within more

broadened Au5d and O2p bands (Figure 6.3(d)), indicating stronger Au-O bonding

compared to that on the surface with the adsorbed single O atoms. However, the

thermodynamic stability of a double O chain is not solely determined by the Au-O

bonding. Contrary to the Au-O bonding, a high coverage and high density of O atoms

on the step edge within a double O chain bring about some repulsion which slightly

lifts up O atoms and elongates the average bond length between the O atoms of the

chain and Au atoms on the terrace by about 0.08 Å, corresponding to a decreased

adsorption energy per O atom. The higher coverage of O atoms on the surface with a

double O chain and a resulting electrostatic repulsion may account for its lower

thermodynamic stability than that of the surface with a single O chain.
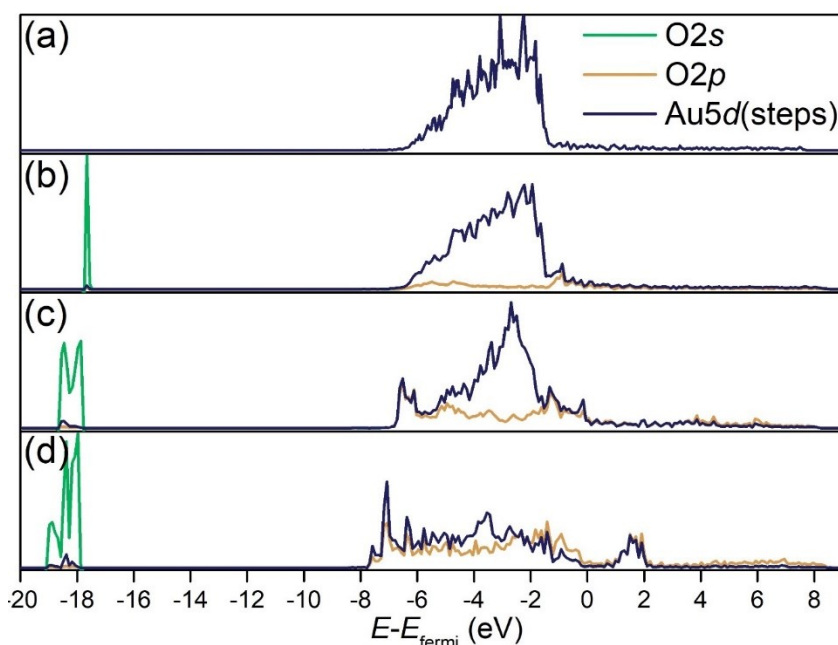
Figure 6.3. The projected density of states (PDOS) of O2s, O2p, and Au5d states for one O atom and one adjacent Au atom at the step edge of a Au(221) surface: (a) a regular surface without O chains, (b) with a single O atom adsorbed at the step edge, (c) with a single O chain, or (d) with a double O chain.

6.1.2 The formation of oxygen vacancies

If a gold catalyst is exposed to an insufficiently rich oxygen source, we anticipate the formation of incomplete double oxygen chains with one or more oxygen defects within them. Oxygen vacancies could also be formed as a result of oxygen atoms of the chain participating in the oxidation reactions of adsorbate molecules, such as CO. The O vacancies could further act as active sites for subsequent adsorption of O_2 and CO. In view of the known crucial role of the oxygen vacancies in the reactivity of oxide catalysts, i.e. La_2O_3 and CeO_2 introduced in Chapter 2-5, we considered two types of oxygen vacancies, a single or a double vacancy, formed within the 1D double chain on the Au(221) surface. The formation energy of a single oxygen vacancy reaches 0.81 eV (Figure 6.4 (a)). As for the double vacancies, two different arrangements for the defects were considered, the adjacent or separate ones (Figure 6.4(b) and (c)). The formation energy of two oxygen vacancies is calculated to be almost equal to twice that of a single oxygen vacancy. In this work, the oxygen vacancy formation energies were obtained by taking the difference between the energy of the surface slab with a complete double oxygen chain and the sum of the energies of the surface slab with the defective chain and the removed oxygen atoms (the energy of O atom was taken as the half of O_2 molecule). The energy required for the formation of two adjacent vacancies (1.59 eV) is lower than that required to create separate oxygen vacancies (1.75 eV) as shown in Figure 6.4 (b) and (c). The more facile formation of adjacent oxygen vacancies results from a little more destabilization of the adsorption geometry of the central top O atom in Figure 6.4(c). Therefore, we selected the geometry with two adjacent O vacancies as the probable active site for the subsequent calculations of the adsorption and activation of CO and O_2.

| $E_v = 0.81$ eV | $E_v = 1.59$ eV | $E_v = 1.75$ eV |
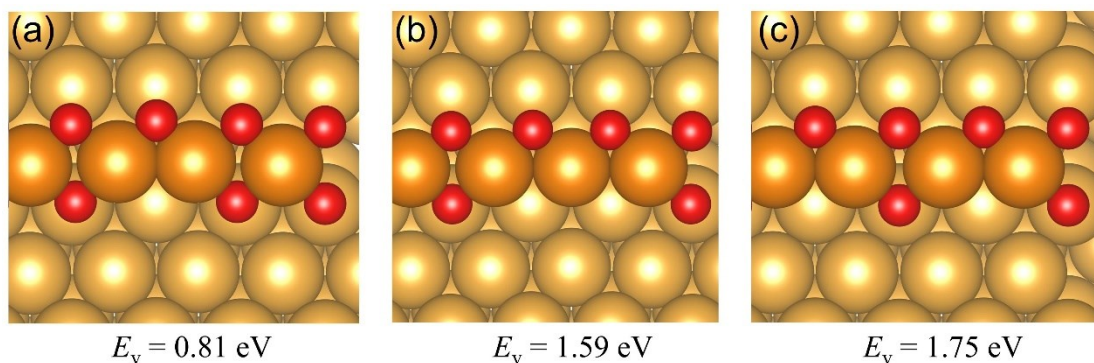
Figure 6.4. The oxygen vacancy formation energies (eV) and the corresponding geometries of the defected double O chain on a Au(221) surface with (a) one oxygen vacancy, (b) two adjacent oxygen vacancies, (c) two separate oxygen vacancies. The oxygen vacancy formation energy in the case of two vacancies is the total energy required to form two vacancies rather than the average energy per vacancy. Au atoms at the step edge are indicated by an orange color; the remaining Au atoms are shown in gold. O atoms are shown in red.

6.2 The Adsorption of CO and O₂

6.2.1 The adsorption of CO

We have also investigated the adsorption of a CO molecule on the regular Au(221) surface and on the same surface hosting a double oxygen chain with O vacancies. Next, we studied the reaction of the adsorbed CO with the oxygen atom of the double oxygen chain. The adsorption energies and the reaction mechanism have been separately given in Figure 6.5 and Figure 6.6. The bonding of CO to transition metals is usually explained in terms of the σ-donation/π-backdonation model.[161] Because the non-bonding σ orbital of CO is centered on C, CO usually binds to a metal via its carbon end donating the nonbonding σ to an empty d orbital of a metal. This is what our calculations predict for the adsorption of CO on the Au(221) surface. CO adsorbing on the surface via the oxygen end only releases 0.09 eV, but the one adsorbing via the carbon end releases 0.69 eV (see Figure 6.5(a) and (b)). A similar adsorption strength of CO is also observed for its adsorption with the carbon end on a vacancy site of the double oxygen chain with one or two adjacent oxygen vacancies, releasing -0.64 and -0.62 eV, respectively (Figure 6.5(c) and (d)). When adsorbing on the double chain with

75

two separate vacancies, the adsorption energy of CO increases to -0.76 eV (Figure 6.5(e)). Besides, the C-O bond length is elongated by 0.04 Å to reach 1.19 Å on the double chain with oxygen vacancies owing to a stronger π back-donation from Au to the π^* of CO relative to the adsorption on the regular Au(221) surface.
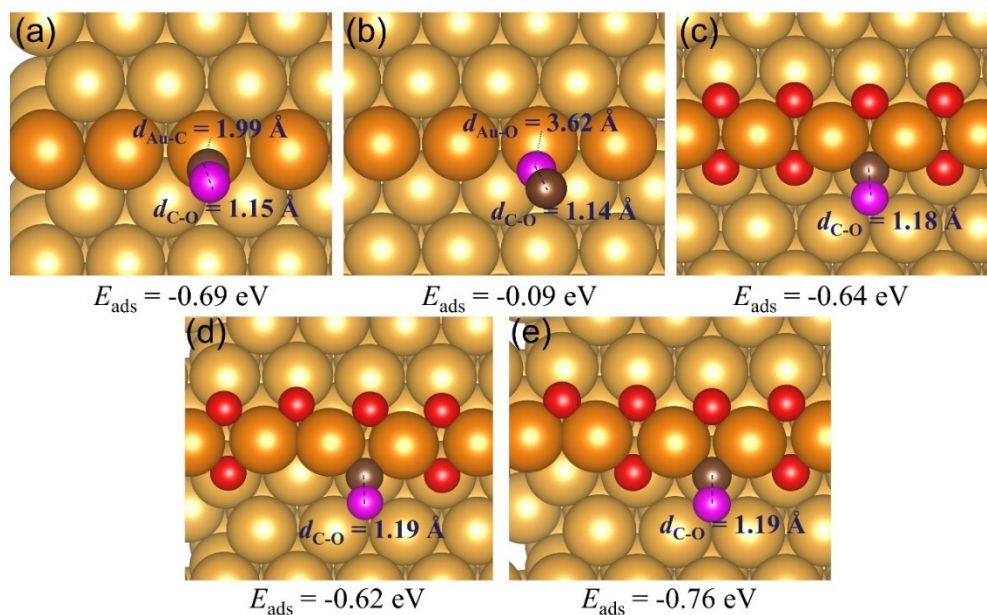
Figure 6.5. The adsorption energies and the corresponding geometries for the CO molecule adsorbed in various ways on the regular Au(221) surface (a,b) via (a) the carbon end, or (b) the oxygen end, and via the carbon end on the surface with an incomplete double oxygen chain (c-e) with (c) a single O vacancy, (d) two adjacent O vacancies, and (e) two separated O vacancies. The C-O bond length and selected Au-O/C bond lengths are given in the corresponding figures. Au atoms at the step edge are indicated by an orange color; the remaining Au atoms are shown in gold. O atoms of the chain structure are shown in red, while O and C atoms of the CO molecule are shown in pink and black, respectively.

We anticipate the Au(221) surface with double oxygen chains formed along the step edge under a sufficient oxygen source as an idealized surface model. The chains can provide O atoms to oxidize CO resulting in the formation of O vacancies. Hence, we conducted ci-NEB calculations to study the oxidation of CO on a double chain where one of the O atoms of the chain reacts with the adsorbed CO* molecule (where * denotes the adsorbed state) to form a CO_2^* molecule. The reaction path has been shown

in Figure 6.6. The CO* first adsorbs at a terrace site adjacent to the step edge, then moves closer to one of the oxygen atoms of the double chain to form a bent CO_2* with a relatively small barrier (0.19 eV), accompanied by the gradual decrease of the carbon-oxygen bond length d_{C3-O1} from 2.70 Å to 1.37 Å. This bent CO_2* is similar to the structure of the charged CO_2^- species[162], which is metastable and easily gives away its extra electron becoming a linear CO_2 with the C-O bond lengths of 1.18 Å with a near-zero energy barrier. The linear CO_2 molecule in the final state desorbs from the surface because of its negligibly low binding energy on Au. The overall reaction of CO oxidation by the oxygen atom of the double chain to CO_2 is exothermic by 2.14 eV. The reaction is thermodynamically facile, but kinetically limited by a relatively weak adsorption (-0.33 eV) of CO at flat terrace sites (which means that the coverage and residence time of CO on the surface will be rather low).
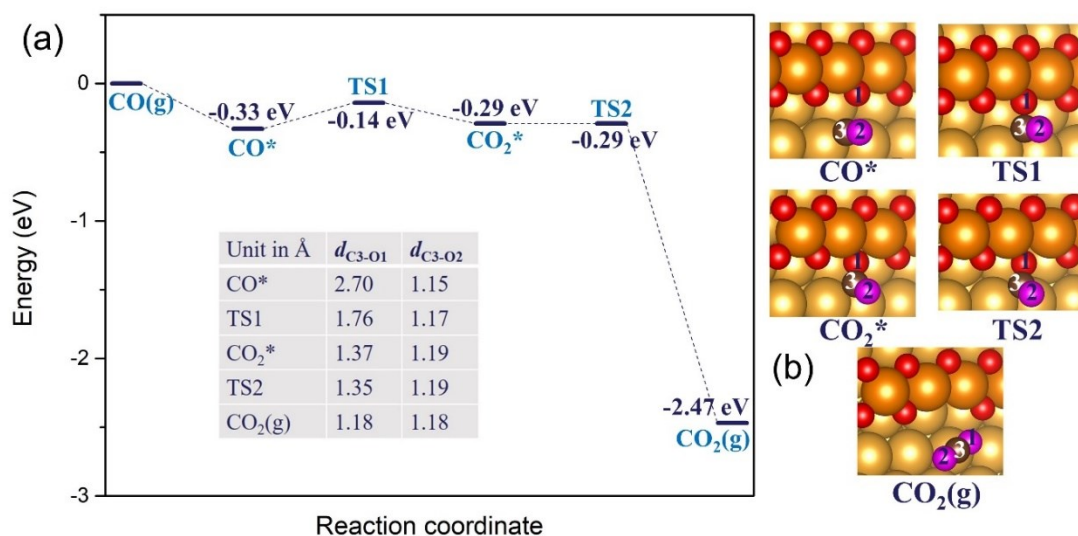
Figure 6.6. (a) The reaction energy diagram and (b) the corresponding geometries of CO reacting with the oxygen atom of the double chain on a Au(221) surface. The labelled C-O bond lengths are listed in a table embedded in the figure (a). Au atoms at the step edge are indicated by an orange color; the remaining Au atoms are shown in gold. O atoms of the chain structure are shown in red, while O and C atoms of the CO molecule are shown in pink and black, respectively.

6.2.2 The adsorption of O_2

We also calculated the adsorption energies of an oxygen molecule on the pristine Au(221) surface and on the vacancy sites of a double oxygen chain. The optimized adsorption geometries and the adsorption energies are shown in Figure 6.7. It is possible for O_2 to bind on the surface in either horizontal or vertical way. Usually, O_2 prefers to adsorb on the surface or the vacancies in a horizontal way. On the regular Au(221) surface, the energy of the horizontally or vertically adsorbed oxygen molecule is -0.22 and 0.35 eV, respectively (Figure 6.7(a) and (b)). However, a slightly less favorable adsorption energy, -0.01 or 0.48 eV, is observed for the horizontal or vertical adsorption of O_2 on the chain with a single O vacancy due to larger steric hindrance arising in the confined space of a single vacancy (Figure 6.7(c) and (d)). In contrast, more favorable adsorption energy values of -0.32 and 0.10 eV are obtained for the horizontal and vertical O_2 adsorption on the double chain with two adjacent vacancies, while the energies of -0.34 and 0.31 eV correspond to the adsorption on the chain with separate vacancies (see Figure 6.7 (e)-(h)). The horizontal adsorption of O_2 on the double chain with separate vacancies leads to a relatively large distortion of the chain structure. Conversely, the facile distortion of the two separate vacancies enhances the horizontal adsorption strength of O_2 compared to a less flexible nature of the double chain with a single O vacancy resulting in a weaker adsorption strength of O_2 on the former. Correspondingly, the O-O bond length of the activated O_2 molecule elongates to 1.40 Å (typical for a peroxo O_2^{2-} species) when adsorbed on the two separate O vacancies. The zero net spin magnetic moment is also indicative of a peroxo species (structures (e) and (g) of Figure 6.7). A partially-activated O_2 shows a shorter bond length (~1.3 Å) with the spin magnetic moment of approximately 1 which is either evenly distributed over two O atoms (structures (a) and (c) of Figure 6.7), or remains mainly localized on the O atom far from the surface (structures (b), (d), (f) and (h) of Figure 6.7). In all cases, the adsorbed O_2 molecule shows longer O-O bond length than that in gas phase (1.23 Å).
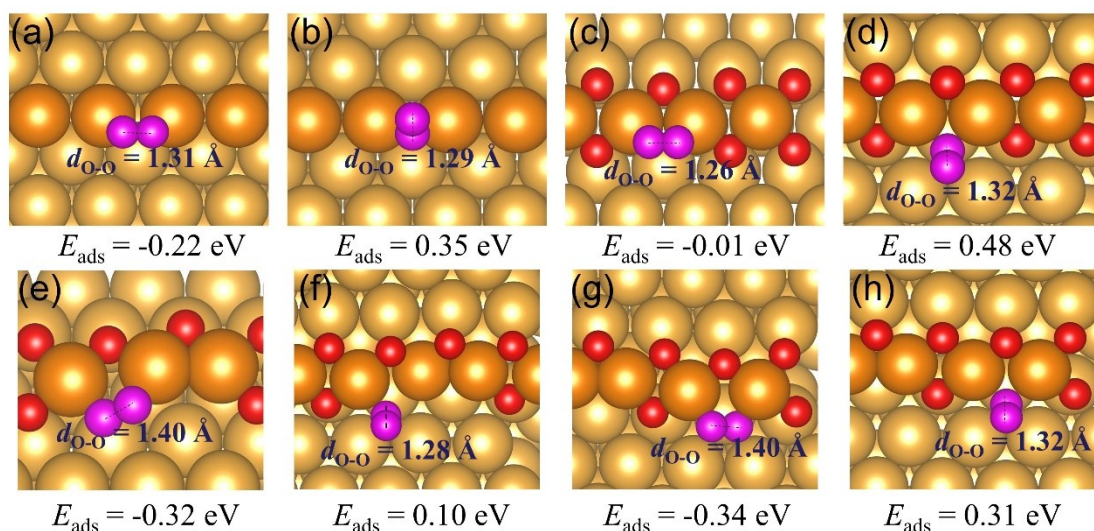
Figure 6.7. The adsorption energies and the corresponding geometries for the O_2 molecule adsorbed in various ways on the regular or O-covered Au(221) surface: (a) horizontally or (b) vertically adsorbed on the regular Au(221) surface, (c) horizontally or (d) vertically adsorbed on the double oxygen chain with the single O vacancy, (e) horizontally or (f) vertically adsorbed on a chain with two adjacent O vacancies, (g) horizontally or (h) vertically adsorbed on a chain with two separate O vacancies. The O-O bond length of the O_2 molecule is given in the corresponding figures. Au atoms at the step edge are indicated by an orange color; the remaining Au atoms are shown in gold color. O atoms of the chain structure are shown in red, while the O atoms of the O_2 molecule are shown in pink.

6.3 The Reaction of CO and O_2

In view of the enhanced adsorption strength of O_2 and CO discussed in the previous sections, it becomes necessary to elucidate the reactivity of O_2 and CO on a double oxygen chain with O vacancies on the Au(221) surface. Two principal types of CO oxidation mechanisms considered in this study are named the dissociation mechanism and the association mechanism, according to the way of participation of O_2 in the reaction. In the dissociation mechanism, O_2 first dissociates to two O* atoms. The adsorption and dissociation of O_2 are facilitated on the O vacancies of a double O chain due to the strong interaction between O_2 and the defective double chain. Thereafter, the formed reactive O* atom can directly bind with the adsorbed CO* to form CO_2* (see eq. 6.1). In the association mechanism, the adsorbed O_2* directly reacts with the co-adsorbed CO* to form an intermediate, OCOO*, which is further decomposed to CO_2*

and O*, as indicated in eq. 6.2. (The intermediate OCOO* is a metastable minimum. As the reader will see in section 6.3.2.2, depending on the specific adsorption sites of the reactants, sometimes the OCOO* intermediate does not form, but a reaction proceeds directly to CO_2.) The associative mechanism was previously computationally predicted by our group to be much faster than the dissociative one for CO oxidation on a Au(321) surface at the experimentally relevant conditions, due to a too high activation energy for the dissociation of O_2 (~1 eV).[163]

$$O_2 * \rightarrow O * + O * \xrightarrow{+CO*} CO_2 \qquad (6.1)$$

$$CO * + O_2 * \rightarrow OCOO * \rightarrow CO_2 + O * \qquad (6.2)$$
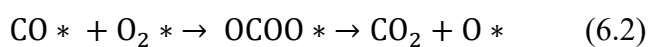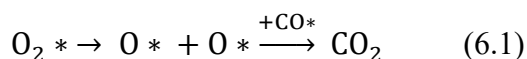
6.3.1 The dissociation mechanism

In the dissociation mechanism, O_2 first adsorbs on the gold surface, then decomposes to form the adsorbed atomic O*. Hence, we initially compared the energy barrier of O_2 dissociation on the regular Au(221) surface and on the same surface hosting a double oxygen chain with two adjacent vacancies. As shown in Figure 6.8(a), O_2 preferentially adsorbs horizontally on the regular Au(221) surface with the adsorption energy of -0.22 eV and dissociates by releasing 0.36 eV. However, the energy barrier of O_2 dissociation goes up to a rather large energy (1.84 eV). The bond length of the activated O_2 in the transition state is elongated to 2.03 Å relative to 1.31 Å in the initial state. On a surface with a defected double oxygen chain with the adjacent oxygen vacancies, O_2 can be more strongly adsorbed and activated, compared to a regular surface. The adsorption strength of O_2 adsorbed at the vacancies site in a horizontal way enhances to -0.32 eV, and the dissociation of O_2 with the O-O bond length stretching from 1.40 Å to 2.14 Å in the transition state requires 0.87 eV, which is less than half of the energy barrier on the regular Au(221) surface (see Figure 6.8(b)). This barrier lowering is attributed to the polarization of O_2 brought by the oxygen vacancies on the double oxygen chain with extra valence electrons localized at the vacancies. The formed two atomic O* tend to bind on the defect sites of the chain structure, forming a distorted double oxygen

chain, whose energy gets lowered by 1.18 eV after a relaxation to an ideal undistorted chain. The distorted double chain may also restructure by releasing one O* atom located at the crease which is loosely bound and is prone to move away, leading to the formation of one adsorbed surface O* atom and a double chain with one vacancy on the Au(221) surface. The isolated O* atom is calculated to preferentially bind at the hollow sites among the step Au atoms on the regular Au(221) surface, as discussed in section 6.1.
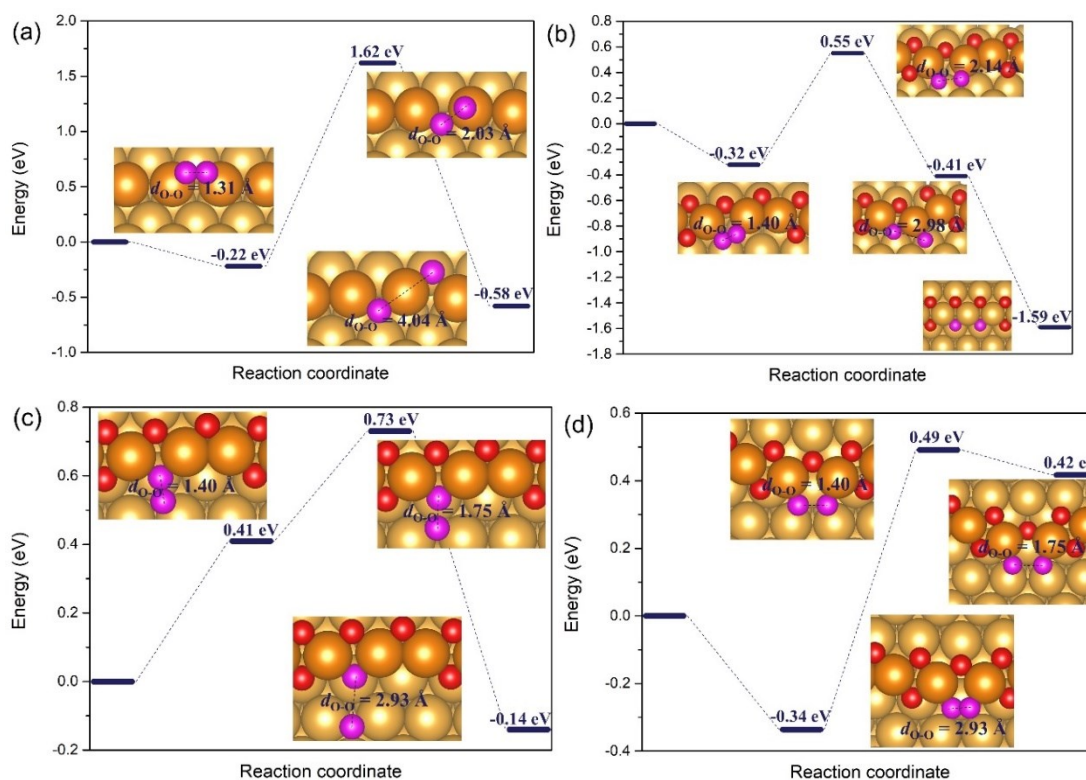
Figure 6.8. The theoretical pathways and the corresponding energy profiles for the dissociation of the O_2 molecule starting from various initial adsorption configurations: (a) horizontally adsorbed on the regular Au(221) surface, (b) horizontally adsorbed on the double oxygen chain with two adjacent O vacancies on the Au(221) surface, (c) vertically adsorbed on the O chain with two adjacent O vacancies, and (d) horizontally adsorbed on the O chain with two separate O vacancies. The zero of energy corresponds to the sum of electronic energies of the free gas-phase O_2 molecule and of the respective Au(221) surface with or without the O chain. The geometries and the O-O bond distance of the O_2* molecule are given in insets. Au atoms at the step edge are indicated by an orange color; the remaining Au atoms are shown in gold. O atoms of the chain structure are shown in red, while the O atoms of the O_2* molecule are shown in pink.

Although the vertical adsorption of O_2 is not the most favorable scenario, we also calculated the corresponding O_2^* dissociation barrier. In the initial geometry, one O atom of the O_2^* molecule adsorbs at a vacancy site of the chain while the other O atom binds to a Au atom at the terrace (Figure 6.8(c)). The adsorption energy of O_2 is positive, 0.41 eV, (indicating unfavorable adsorption) whereas the dissociation barrier reduces to 0.32 eV, lower than the dissociation of the horizontal adsorption mode of O_2^*. The dissociation is an exothermic process releasing 0.55 eV. The initial geometry of O_2^* horizontally adsorbed on the O chain with two separate vacancies shown in Figure 6.7(g) was used to elucidate another possible path for O_2^* dissociation. The calculated energy barrier for O_2^* dissociation of 0.83 eV is close to that obtained for the dissociation of O_2^* horizontally adsorbed on the adjacent O vacancies, discussed above, while the dissociation process is endothermic with a reaction energy of 0.76 eV (Figure 6.8(d)). A CO* molecule adsorbed at a terrace site could directly bind to an oxygen atom of the double chain eventually forming CO_2 and an oxygen vacancy, as shown in Figure 6.6. With one or two O vacancies formed in the chain, CO can also adsorb at a vacancy site (see Figure 6.5(c) – (e)). If we look at the dissociation path of vertically adsorbed O_2 shown in Figure 6.8 (c), we see that one of the dissociated O* atoms fills a vacancy in the chain, while the other O* atom moves away from the double oxygen chain. In general, we expect that some of the O* atoms produced by O_2^* dissociation may fill vacancies in the O chains, but some of them may end up as individually adsorbed O* atoms. Therefore, we could anticipate a possible path of CO oxidation, where one O* atom generated after O_2^* dissociation ends up adsorbed at a terrace site close to the chain, then a CO molecule adsorbs at a vacancy site on the O chain and reacts with the atomic O* adsorbed at a nearby terrace site to form CO_2. We thus constructed a new initial structure for a CO* + O* reaction with an atomic O* adsorbed at an fcc-terrace site and CO* at a vacancy site on a double O chain on the Au(221) surface. A NEB calculation was conducted to search for the transition states in the process of CO* binding to O*. The reaction profile and the adsorption geometries are shown in Figure

6.9. The adsorption energy of CO on the chain structure reaches -0.56 eV in the presence of an O* atom at an fcc terrace site of Au(221) (labeled as fcc1 in Figure 6.9(b)), and later becomes more negative, -0.60 eV, after the migration of the atomic O* to a hcp site via a diffusion barrier of 0.19 eV. The atomic O* continues to migrate to a new fcc site (labeled as fcc2 in Figure 6.9(b)) closer to the adsorbed CO* via a relatively low energy barrier of 0.08 eV. Finally, the co-adsorbed CO* and O* bind and form a CO_2* molecule by releasing a relatively high energy of 2.89 eV. It deserves to mention that the rate-limiting step is the migration of O* and not the binding of CO* and O* in this process. Throughout the formation process of CO_2, the C3-O2 bond length of the adsorbed CO* remains constant (d_{C3-O2}, 1.18 Å). With the pre-adsorbed O* atom getting closer to CO*, the C3-O1 distance (d_{C3-O1}) corresponding to the formation of the second C-O bond reduces from 3.95 Å to 1.18 Å.
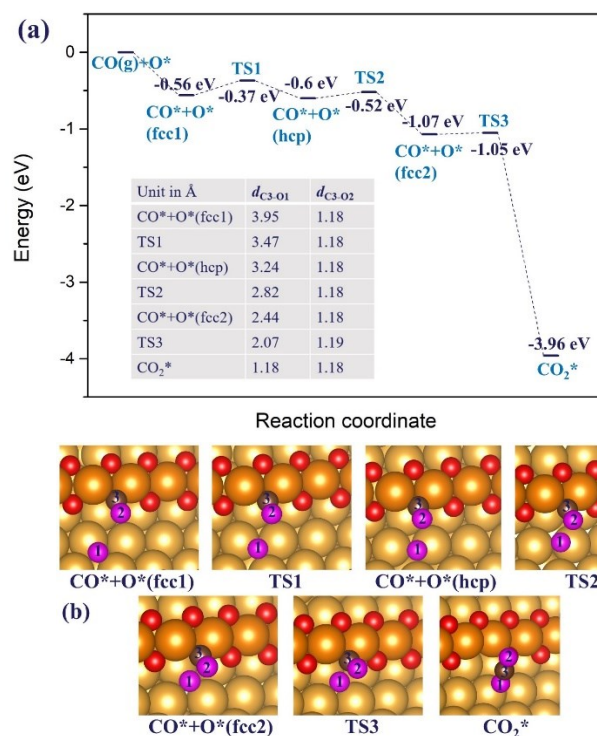
Figure 6.9. (a) The reaction energy diagram and (b) the corresponding geometries of CO* adsorbed at a vacancy site in a double O chain reacting with an O* atom adsorbed at a terrace site on a Au(221) surface. The labelled C-O bond lengths are listed in a table embedded in the energy diagram of panel (a). Au atoms at the step edge are indicated by an orange color; the remaining Au atoms are shown in gold. O atoms of the chain structure are shown in red, while O and C atoms of the CO molecule are shown in pink and black, respectively.

To summarize, in the dissociation mechanism, the dissociation of O_2* is the rate-limiting step for the CO oxidation reaction. The reaction barrier reaches up to 1.84 eV on the regular Au(221) surface. The energy barrier of O_2* dissociation could be further reduced to 0.87 eV for an O_2* molecule horizontally adsorbed on a double O chain with two adjacent oxygen vacancies, while the barrier lowers to only 0.32 eV for the vertical adsorption of O_2. However, in the latter case, the adsorption of O_2 is endothermic.

6.3.2 The association mechanism

6.3.2.1 The association mechanism on a regular Au(221) surface

In the association mechanism, O_2* directly binds to the co-adsorbed CO* without the dissociation of O_2*. A metastable OCOO* structure forms as an intermediate and then decomposes to CO_2* and an adsorbed atomic O*. We calculated the reaction paths satisfying the association mechanism on Au(221) with or without an O chain. The co-adsorption of CO and O_2 on the pristine Au(221) surface releases 0.85 eV, with the horizontal adsorption of O_2* on a bridge site and the vertical adsorption of CO* on a top site (Figure 6.10). In order to form a more stable intermediate, OCOO*, CO* must slightly turn and move toward O_2*. The energy barrier is only 0.14 eV. The distance (d_{C4-O2}) between the O_2* and CO* decreases from 3.62 Å in the initial state to 1.37 Å in the OCOO* intermediate. The formation of the OCOO* intermediate releases 0.23 eV. The intermediate further dissociates to CO_2* (with the two C-O bond lengths of 1.18 Å) and an O* atom adsorbed in a bridge mode on the step edge of the Au(221) surface. The transition state shows a structural distortion of the OCOO* intermediate and has an activation barrier of 0.33 eV. The energy barrier of the rate-limiting step in the association mechanism is much lower than that in the O_2 dissociation mechanism by 1.51 eV. This demonstrates that the association mechanism is likely to be more effective on the regular Au(221). However, the relatively low activation energy of CO oxidation on the regular Au(221) surface based on the association mechanism does not mean a high reactivity of extended gold surfaces for CO oxidation which under typical

reactor conditions will be restrained by the low concentration and low transient time of the adsorbed O_2^* arising from its weak binding strength on pure Au. A higher reaction rate could be further achieved if the adsorption strength of O_2 on pure Au is increased by introducing Ag impurities, as is the case on nanoporous gold.[164-165]
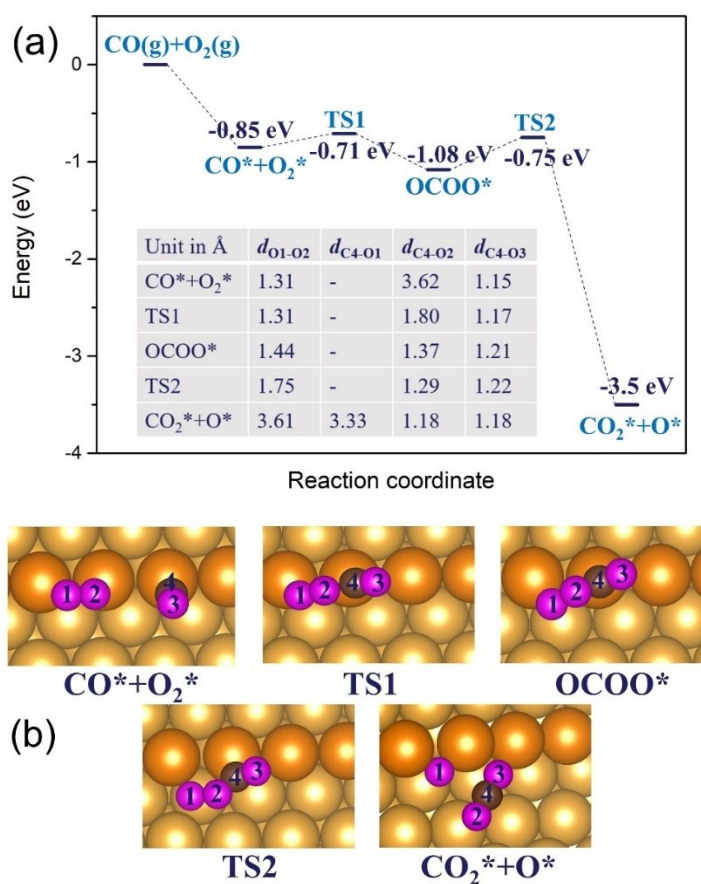
Figure 6.10. (a) The reaction energy diagram and (b) the corresponding geometries of the reaction between the co-adsorbed CO* and O_2^* molecules on the regular Au(221) surface. The labelled O-O and C-O distances are listed in a table embedded in the energy diagram in panel (a). Au atoms at the step edge are indicated by an orange color; the remaining Au atoms are shown in gold color. O and C atoms of the adsorbates shown in pink.

6.3.2.2 The association mechanism on a Au(221) surface with a double chain

Next, we calculated the reaction mechanism of CO oxidation when CO* and O_2^* co-adsorb on O vacancies of a double O chain on the Au(221) surface. The reaction mechanism depicted in Figure 6.11 was revealed by a NEB calculation. The co-

adsorption of CO* and O_2* at a double O vacancy site releases the energy of 0.92 eV and has to overcome a slight activation barrier of 0.13 eV (if a CO molecule co-adsorbs near already adsorbed O_2 at a double O vacancy site). As discussed above, separately adsorbed O_2* and CO* at a double O vacancy release 0.32 eV and 0.62 eV, respectively. The co-adsorption energy, -0.92 eV, is about equal to the sum of the two individual adsorption energies indicating that a slight deformation of the chain needed to accommodate the two adsorbates is compensated by their favorable binding at the vacancies (Figure 6.11). Next, the co-adsorption complex restructures to an even more favorable geometry in which a linear O-Au-CO oxocarbonyl complex forms (further denoted as OAuCO) via an activation barrier of 0.2 eV. This linear structure is stabilized by a strong σ-donation from CO to Au and an enhanced π-backdonation from Au to CO. The rearrangement is accompanied by a structural distortion of the Au atoms at the step edge, so that Au atoms on the step edge appear twisted, and by a rotation of the O_2* molecule in such a way that only one O atom remains bound at a vacancy site, whereas the other O atom binds to a terrace underneath the step. In the process, the O-O bond (d_{O1-O2}) in the twisted minimum shrinks to 1.30 Å from 1.38 Å in the initial co-adsorbed state (see Figure 6.11(b)). O_2* becomes less activated after the departure of one O atom (labelled as O2) from the initial adsorption site at a double O vacancy because the change in the O_2* orientation reduces the charge transfer to the π* orbital of O_2*. The bond length of 1.30 Å is typical of a superoxo (O_2^-) species. This co-adsorption geometry of O_2* and CO* herein called "twisted", forms an OCOO* intermediate after overcoming a relatively high barrier of 0.74 eV. In the transition state, the OAuCO fragment realigns its axis until CO* and O_2* get close and orient parallel to each other. The OCOO* intermediate lies energetically 0.03 eV below the "twisted" CO* + O_2* co-adsorption complex. It binds via the C4 and O1 atoms at the O vacancy site originally occupied by O_2*. Finally, the OCOO* intermediate dissociates to CO_2* and an adsorbed O* atom filling an O vacancy in a distorted chain after overcoming an activation barrier of 0.43 eV. The formed CO_2* molecule shows the C-O bond lengths

of 1.18 Å and is located 4.65 Å away from the dissociated atomic O*. The rate-limiting step in the association mechanism depicted in Figure 6.11 (associated with TS2) goes over an energy barrier (0.74 eV) of comparable height to that of the direct O_2* dissociation mechanism (0.87 eV), indicating that the two mechanisms may be competing at experimental conditions.

(a)

Unit in Å	$d_{O1\text{-}O2}$	$d_{C4\text{-}O2}$	$d_{C4\text{-}O3}$
Ads_TS	1.38	2.94	1.15
CO*+O_2*	1.38	2.88	1.15
TS1	1.33	3.11	1.15
CO*+O_2*(twist)	1.30	5.28	1.15
TS2	1.33	1.96	1.17
OCOO*	1.47	1.37	1.22
TS3	1.67	1.30	1.21
CO_2*+O*	4.65	1.18	1.18

(b)
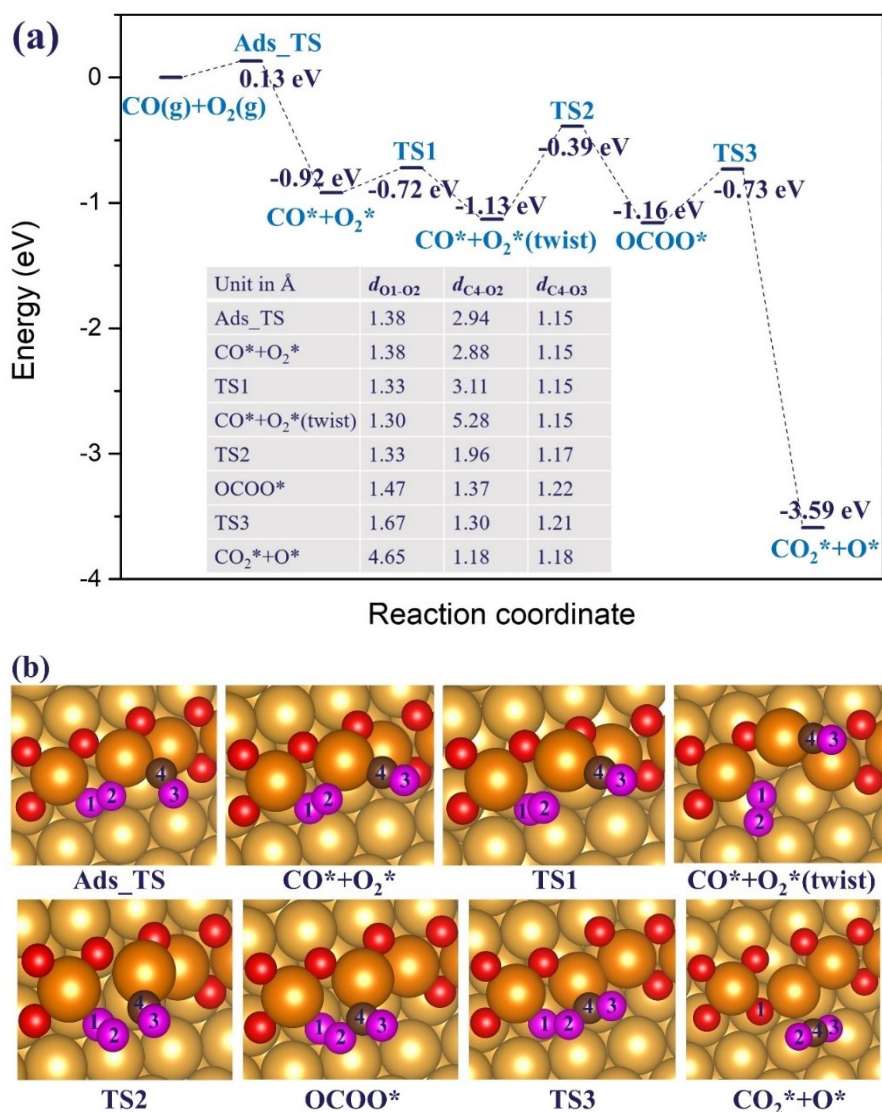
Figure 6.11. (a) The reaction energy diagram and (b) the corresponding geometries of the stationary points along the reaction path between the co-adsorbed CO* and O_2* molecules on a double O chain with two adjacent O vacancies on the Au(221) surface. The labelled O-O and C-O bond lengths are listed in a table embedded in panel (a). Au atoms at the step edge are indicated by an orange color; the remaining Au atoms are shown in gold. O atoms of the chain structure are shown in red, while O atoms of the adsorbates are shown in pink. C atoms are shown in black.

Another scenario of CO oxidation possibly involves the reactive CO* molecule adsorbed at a terrace site close to the step edge, while O_2* adsorbs at a vacancy site of the oxygen chain on the Au(221) surface. Various initial orientations of the interacting CO* and O_2* were considered to identify possible pathways. The co-adsorption energy of CO* and O_2* varies between -0.51 and -0.63 eV in the considered initial structures and the corresponding activation barriers lie between 0.10 and 0.35 eV. Especially for Case 1 shown in Figure 6.12, the co-adsorption complex of CO* and O_2* smoothly changes to the transition state of the OCOO* shape via the lowest barrier energy of 0.1 eV. The transition state shows an extended O-O bond length of 1.65 Å and a forming C-O bond length of 1.43 Å. As the OCOO* activated complex dissociates, a CO_2 molecule is formed and an O* atom fills a vacancy in the oxygen chain structure. For the other similar pathways with slightly different initial geometries of the co-adsorbed CO* and O_2*, the reaction energy barriers are also considerably lower than the barrier of 0.74 eV calculated for an analogous recombination reaction of CO* and O_2* where both CO and O_2 adsorb on the O chain with two adjacent vacancies. The higher barrier energy in the latter case is attributed to the formation of a stable OAuCO fragment, while such an intermediate is not formed if CO* adsorbed at a terrace site reacts with O_2*. Therefore, we could speculate that the oxidation of CO is more likely to follow the association mechanism in which CO* and O_2* separately adsorb, respectively, at a terrace and O chain vacancy sites rather than the associative mechanism in which CO* and O_2* initially co-adsorb on the oxygen chain with vacancies and also more likely than the dissociation mechanism.
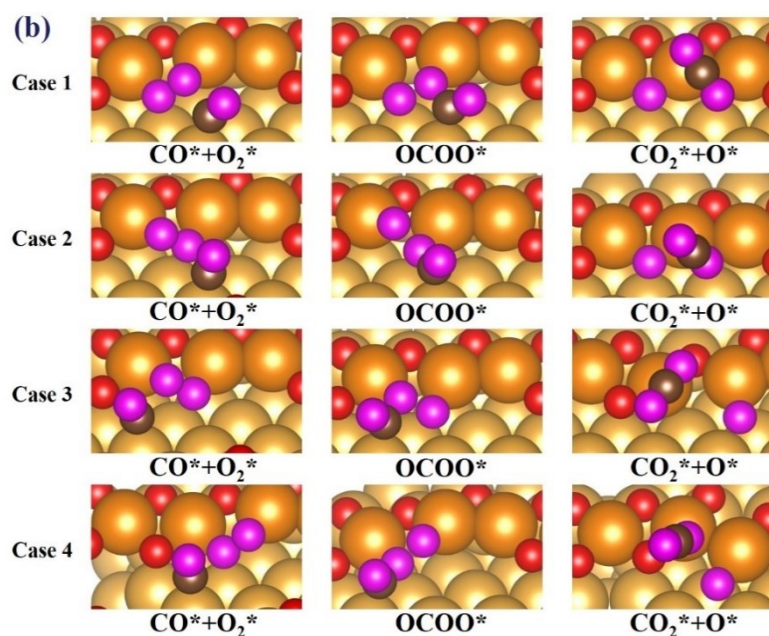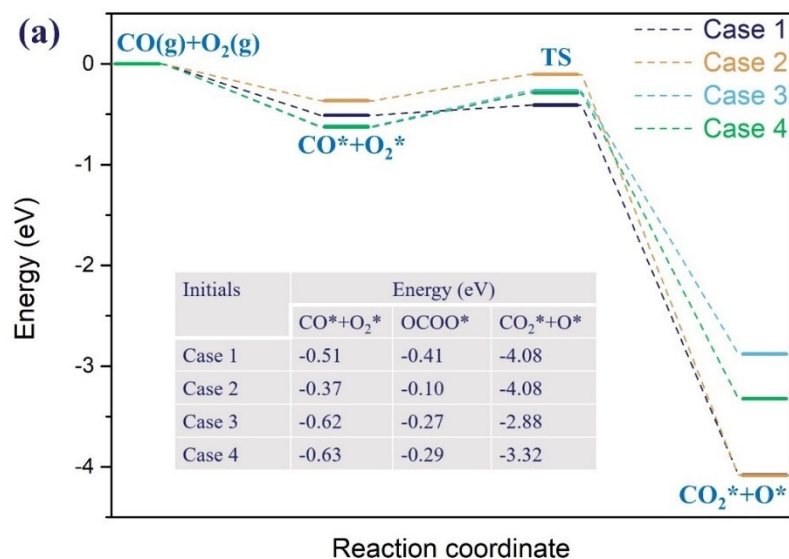
Figure 6.12. (a) The reaction energy diagram and (b) the corresponding geometries of the stationary points along the reaction path between CO* adsorbed at a terrace site and O_2* adsorbed on a double O chain with two adjacent O vacancies on the Au(221) surface. Four initial structures of co-adsorbed CO* and O_2* with slightly different orientation of CO* and O_2* were calculated and compared. Au atoms at the step edge are indicated by an orange color; the remaining Au atoms are shown in gold. O atoms of the chain structure are shown in red, while O atoms of the adsorbates are shown in pink. C atoms are shown in black.

Chapter 7 Summary and Outlook

This dissertation discusses computational results relevant to heterogeneous catalytic systems and consists of two main parts. The first part is devoted to the structure and properties of pure and doped rare earth oxide (REO) catalysts and is covered in Chapters 2-5. This part assesses the accuracy of PBE+U and HSE06 functionals in forecasting the structural parameters and thermodynamic characteristics of A-type lanthanide sesquioxides and fluorite-structure cerium dioxide, as well as the surface properties of $CeO_2(111)$ and $Nd_2O_3(0001)$. It also examines the impact of heteroatom dopants (*s*-block, *d*-block and *f*-block) partially substituting surface La atoms on the surface reducibility and Lewis acidity/basicity. This is determined using various descriptors such as oxygen vacancy formation energy, the position of the unoccupied metal $5d$-band or occupied oxygen $2p$-band center, and the adsorption energies of probe molecules (NH_3 or CO_2) on the regular or defective doped $La_2O_3(0001)$ surface. The second part (Chapter 6) focuses on the formation of a linear oxygen chain structure on the Au(221) surface and its role in the oxidation of CO. Different possible reaction pathways of CO oxidation on a regular Au(221) surface and on a Au(221) surface with adsorbed oxygen organized into a one-dimensional oxide chain structure were calculated.

In Chapter 2, we reproduce well the "lanthanide contraction" in bulk REO oxides by using the HSE06 functional. However, the lattice parameters of Ln_2O_3 are usually slightly underestimated (by less than 0.03 Å). The PBE functional was combined with a Hubbard parameter U, which represents the strength of the on-site Coulomb repulsion between $4f$ electrons. The DFT+U method is a computationally feasible approach to correct conventional DFT methods unable to properly describe strong correlation between f electrons. The best agreement with the HSE06 geometries could be reached using U values of 3-4 eV for Ho_2O_3, Tm_2O_3, and CeO_2, whereas for Eu_2O_3, Gd_2O_3 and Er_2O_3, the optimal U value lies at 7-8 eV, although low U values around 3 eV result in a relatively small error. U=1-3 eV results in the best lattice geometries for the remaining

Lu_2O_3 (Ln = La, Ce, Pr, Nd, Pm, Sm, Lu). The HSE06 functional also predicts the energetics of selected model reactions with the error of less than 1.0 eV compared to the experimental values. By fitting the PBE+U results to the values obtained with the HSE06 functional, the U values of 2-3 eV are found to be optimal for La_2O_3, Ce_2O_3, Nd_2O_3, and Ho_2O_3, as well as 1 eV for Pr_2O_3, Pm_2O_3, Eu_2O_3, Tm_2O_3 and Lu_2O_3. For Er_2O_3, a satisfactory agreement with the HSE06 results could be achieved at a broad range of U values, 2-6 eV. However, for Gd_2O_3 PBE+U is not suitable to reproduce the reaction energies with respect to the HSE06 results. The optimal range (2-4 eV) of U values of PBE+U found for CeO_2 applies not only to the proposed reference reaction, but also to a selected redox reaction involving both Ce(IV) and Ce(III). Therefore, we conclude that the U value of about 3 eV could be universally applied to most lanthanide oxides to give accurate description of their structural parameters and reaction energies. In Chapter 3, we further assessed the performance of PBE+U and HSE06 in predicting the electronic and adsorption properties of selected REO surfaces, $CeO_2(111)$, $Ce_2O_3(0001)$, and $Nd_2O_3(0001)$, as well as the applicability of the U parameter obtained for the bulk Ln_2O_3 to the surfaces. Compared to bulk Ln_2O_3, a somewhat larger U value is required for the best agreement with the HSE06 results for electron localization and the work function. U = 3-5 eV is optimal to achieve considerable localization of Ce4f and Nd4f electrons, while U values of 4-7 eV give the closest match of the work function to the HSE06 results for $Ce_2O_3(0001)$ and $Nd_2O_3(0001)$ surfaces. For the adsorption on the $CeO_2(111)$ surface, PBE performs even better than HSE06 with respect to reproducing the experimental adsorption energy for H_2O adsorption. The adsorption energies of NH_3 and CH_3 predicted by the PBE functional agree well with the HSE06 results with the error of less than 0.5 eV, while the U parameter has little effect on the molecular adsorption energies on the $CeO_2(111)$ surface.

Chapter 4 introduces the influence of selected s-block, d-block and f-block heteroatom dopants on the Lewis acidity/basicity of the irreducible $La_2O_3(0001)$ surface. After replacing a surface La atom on a regular $La_2O_3(0001)$ surface by heteroatoms and

reoptimizing the geometry, we find that the *s*-block and *d*-block heteroatoms (excluding Mo), which have smaller ionic radii relative to La and low or variable oxidation states, shift their position upward closer to the surface O atoms and away from the subsurface O atoms, while the *f*-block dopants have the least effect on the surface geometry due to their close ionic radii and preferred oxidation state to La compared to the pristine undistorted $La_2O_3(0001)$ surface. The effect of oxygen vacancy on the surface geometry mainly affects the distance of the subsurface O atoms to the dopants. We also studied a relationship between the acidity/basicity of the surface cationic/anionic sites measured by the adsorption energy of NH_3 or CO_2, and the spin-averaged band center of the unoccupied *d*-band or the occupied *p*-band on the doped $La_2O_3(0001)$ surfaces. The *d*-band center calculated for the unoccupied d_{z2} states of the dopants showed a better correlation with the adsorption energy of NH_3 on the doping site than the band center of the complete *d* band. Furthermore, the *d*- and *p*-band centers of the unoccupied or occupied states for the surface La or O atoms relative to the Fermi level captured the effect of the dopants on the maximum of the occupied states, namely on the position of the Fermi level. On a regular $La_2O_3(0001)$ surface, the high-valence dopants form narrow filled states in the $La5d$-$O2d$ band gap, shifting the Fermi level far away from the $O2p$ VBM and leading to a downward shift of the *d*-band and *p*-band centers on the doped surface. The formation of an oxygen vacancy on the undoped $La_2O_3(0001)$ surface forces the Fermi level to be near $La5d$ CBM due to the loosely bound two extra electrons located at the vacancy site. The low-valence *s*-block and *d*-block dopants form an electron-deficient site which is able to partially or fully accept the extra electrons left by the O vacancy formation, which shifts the Fermi level back toward the $O2p$ VBM, resulting in a more positive *d*-band center and a less negative *p*-band center compared to high-valent *d*-block dopants (including early-transition metals and Fe, Ru) and *f*-block dopants chemically similar to La atoms.

In Chapter 5, we calculated the oxygen vacancy formation energy to measure the surface reducibility of the doped $La_2O_3(0001)$ surface. We found that the surface

oxygen atoms become much more easily removable from the surface when the surface La atom is replaced by s-block and d-block heteroatoms (except early transition metals Ti and V) but not when f-block atoms are doped on the surface. Additionally, we observe a strongly linear relationship between the d- and p-band centers of the surface La or O atoms, and the surface reducibility, expressed in terms of the oxygen vacancy formation energy on the doped $La_2O_3(0001)$ surface. This provides us with a new way to measure the surface reducibility, and allows us to determine the role of the surface reducibility in the reactivity of metal oxide surfaces.

In Chapter 6, we found a favorable formation of a single straight chain of O atoms bound in -O-Au-O- linear structural units along the step edge on a stepped Au(221) surface with the adsorption energy of -0.33 eV per O atom, while the formation of a double oxygen chain with four O atoms coordinated to each Au atom with the adsorption energy of -0.25 eV per O atom is also possible along steps on the Au(221) surface under a sufficient oxygen supply. On the double oxygen chain, the formation of a single oxygen vacancy requires 0.81 eV of energy. When two vacancies are formed on the chain, the adjacent vacancies are more favorable than the separate ones. The O chains with O vacancies are calculated to enable much stronger adsorption of CO and O_2 at a vacancy site. A CO molecule tends to adsorb via the carbon end on the Au(221) surface, especially strongly at the step edges with or without the O chains, with the adsorption energy of more than 0.65 eV in an exothermic way. O_2 prefers to horizontally adsorb on the step edge of the Au(221) surface by releasing the energy of 0.22 - 0.34 eV, slightly stronger at a vacancy site of a double O chain.

We investigated CO oxidation on the basis of two principal types of mechanisms, the dissociation and association mechanisms. As for the dissociation mechanism, the barrier energy of the rate-limiting step for O_2 dissociation could be reduced to 0.87 eV on the oxygen chain with vacancies relative to the value (1.84 eV) computed on the regular Au(221) surface. In the association mechanism, an OCOO* intermediate is much easier to form on the regular Au(221) surface with the barrier of 0.33 eV in

comparison to the double oxygen chain with two adjacent vacancies (0.74 eV for the barrier) when CO* and O_2* co-adsorb on the steps or at a vacancy site of the double O chain. This higher barrier correlates with the stronger co-adsorption state of CO* and O_2* on the O vacancies of a chain as compared to the adsorption on the regular Au(221) surface. However, the energy barrier drops to only 0.1 eV in the case of CO* adsorbed at a terrace site close to O_2* adsorbed at a vacancy site. This is in line with the Sabatier principle which suggests that stronger adsorption of the reactants leads to a higher activation barrier, while the lack of reactivity holds for too weak adsorption; hence, some intermediate value is required for optimal performance. The promotional role of the O chains to the reaction of O_2 and CO on the Au(221) surface probably lies in the activation of O_2 or the direct binding of CO and O_2 depending on the prevailing temperature.

To sum up, this work has been instrumental in establishing the optimal approach to characterize the properties of bulk REOs and REO surfaces, establishing a relationship between Lewis acidity/basicity and the reducibility of a representative surface of REOs, the La_2O_3(0001) surface, and uncovering the reaction mechanisms of CO oxidation facilitated by O chains (1D surface oxide) on the Au(221) surface. However, only one REO and one gold surface were studied in terms of their surface properties and reactivity. Further research should focus other REOs or gold surfaces, such as reducible CeO_2 surfaces or gold surfaces containing other less noble metal impurities (e.g. Ag) to gain a better understanding of their surface properties and reactivity. Given the widespread use of metal-oxide catalysts in heterogeneous catalysis, more attention should be given to the synergetic effect of REOs and gold in a metal-oxide combined system. In addition to the CO oxidation discussed in Chapter 6, further investigation into the mechanisms behind other oxidation or coupling reactions of methane or methanol etc. catalyzed by REOs, gold, or mixed catalysts should be a focus of future research.

Chapter 8 Theoretical Methods and Details

8.1 Density Functional Theory

For describing a molecular system, the time-independent Schrödinger equation was developed as follows:

$$(-\frac{\hbar^2}{2m}\sum_{i=1}^{N}\nabla_i^2 - \frac{\hbar^2}{2m}\sum_{A=1}^{M}\nabla_A^2 - \sum_{i=1}^{N}\sum_{A=1}^{M}\frac{Z_A}{r_{iA}} + \sum_{i=1}^{N}\sum_{j>1}^{N}\frac{1}{r_{ij}} + \sum_{A=1}^{M}\sum_{B>A}^{M}\frac{Z_A Z_B}{R_{AB}})\psi = E\psi \qquad (8.1)$$

here, m is the electron mass, and $\hbar$ is reduced Plank constant, while ∇^2 is the Laplacian operator. A and B denote the M nuclei, and i and j represent the N electrons in the system. The several terms in the brackets separately represent the summation of the kinetic energy of each electron or nuclei, the attractive electrostatic interaction between the electrons and the nuclei, the repulsive interaction among the electrons or the nuclei. Since the nuclei are far heavier than the electrons, the electrons move faster and are more susceptible to the change of their surroundings. Hence, the system could be reasonably treated as two individual parts, the electrons and the nuclei. The above-mentioned time-independent Schrödinger equation is then simplified to describe the electrons.

$$(-\frac{\hbar^2}{2m}\sum_{i=1}^{N}\nabla_i^2 - \sum_{i=1}^{N}\sum_{A=1}^{M}\frac{Z_A}{r_{iA}} + \sum_{i=1}^{N}\sum_{j>1}^{N}\frac{1}{r_{ij}})\psi = E\psi \qquad (8.2)$$

Compared to the previous one, the kinetic energy of the nuclei and the nucleus-nucleus interaction terms are ignored, which is known as the *Born-Oppenheimer* approximation. The solutions of the Schrödinger equation are comprised of E, representing the energy of the electron, and ψ, denoting the electronic wave function. The repulsive interactions among the electrons form a many-body problem, which is challenging to solve mathematically.

One of the approaches for tackling many-body systems is density functional theory (DFT). To start, let us figure out the definition of the electron density. The electron

density is expressed as the square of the wave function ψ which is not physically observable, as follows:

$$n(r) = 2 \sum_i \psi_i^*(r) \psi_i(r) \qquad (8.3)$$

where $n(r)$ represents the probability of finding an electron in a specific spatial coordinate r. By using the electron density $n(r)$, the 3N-dimensional wave function of N electrons could be reduced to a three-dimensional function. Hohenberg and Kohn developed two theorems: the first one (the "Uniqueness Theorem") states that the ground-state energy of a system is a unique functional of the electron density; the second theorem (the "Exactness Theorem") states that the density that minimizes the total energy is the *exact* ground state density. The first theorem tells us that the electron density is closely related to the wave function. It implies that the wave function can also be expressed as a unique functional of the ground state electron density. In other words, there exists a one-to-one mapping between the ground-state wave function and the ground-state electron density. The second theorem shows us the clear way to define an accurate electron density, by minimizing the total energy of the system with respect to the electron density.

Given that the electron density of interacting particles can be obtained by solving a set of equations for a fictitious system of non-interacting particles, the Kohn-Sham equation, which involves only a single electron was developed to make solving the Schrödinger equation more straightforward:

$$\left(-\frac{\hbar^2}{2m}\nabla^2 + V_{eff}(r)\right)\psi_i = \varepsilon_i \psi_i \qquad (8.4)$$

where the solutions of the equation are ψ_i and ε_i representing, respectively, the single-electron wave function and the orbital energy of the corresponding ψ_i. In addition to the first term indicating the kinetic energy of the electron, the other terms from equation (8.2) are involved in the second term on the left-hand side of the equation (8.4), $V_{eff}(r)$ denotes the Koh-Sham potential.

$V_{eff}(r)$ could be further divided into three terms as follows:

$$V_{eff}(r) = V(r) + V_H(r) + V_{XC}(r) \qquad (8.5)$$

where $V(r)$ represents the external potential acting on the electron, which represents the interaction between the electron and the nuclei in the absence of the external electronic or magnetic field. $V_H(r)$ is called the Hartree potential, describing the repulsive interaction between the single electron and the whole electron density.

$$V_H(r) = e^2 \int \frac{n(r')}{|r-r'|} d^3 r' \qquad (8.6)$$

$V_H(r)$ incorporates the interaction between the single electron and itself being part of the whole electron density and includes the contribution from all of the electrons. The spurious self-interaction error is removed in the third term, $V_{XC}(r)$, namely the exchange-correlation potential, which is defined by the functional derivative of the exchange-correlation energy.

$$V_{XC}(r) = \frac{\delta E_{XC}(r)}{\delta n(r)} \qquad (8.7)$$

The exact form of the $V_{XC}(r)$ is unknown, however, an approximation to $V_{XC}(r)$ can be obtained from the exact form for the uniform electron gas. This approximation is known as the local density approximation (LDA). An improved form of this approximation, the generalized gradient approximation (GGA), takes into account both the local electron density and its gradient. Different types of GGA functionals have been developed, such as Perdew-Burke-Ernzerhof functional (PBE) and Perdew-Wang functional (PW91). Combining the LDA/GGA functional with Hartree-Fock exact exchange (see eq. 8.8) in various ratios has resulted in the development of various types of hybrid functionals, which have improved the simulation of many molecular properties.

$$E_X^{HF}(r) = -\frac{1}{2}\sum_{i,j} \iint \psi_i^*(r_1)\psi_j^*(r_2)\frac{1}{r_{12}}\psi_j(r_1)\psi_i(r_2)\, dr_1 dr_2 \qquad (8.8)$$

8.2 Plane-Wave Calculations

To be applicable to crystals with a spatial periodicity, the solutions of the Schrödinger equation can be constructed in the form of a product of a plane wave and a periodic

function, as dictated by Bloch's theorem. This theorem states that each wave function is an energy eigenstate written in the following form:

$$\varphi_k(\boldsymbol{r}) = \exp(i\boldsymbol{k} \cdot \boldsymbol{r})u_k(\boldsymbol{r}) \qquad (8.9)$$

where $u_k(\boldsymbol{r})$ has the same periodicity with the crystal structure, and $\exp(i\boldsymbol{k} \cdot \boldsymbol{r})$ is the exponential form of the plane wave function. Hence, the calculation must be conducted in reciprocal space, which is defined by the vectors $\boldsymbol{k}$. This reciprocal space also yields a primitive cell and the Brillouin zone.

In evaluating the Kohn-Sham equation in conjunction with Bloch's theorem, the integral given below in the reciprocal space is developed over the whole Brillouin zone.

$$g = \frac{V_{cell}}{(2\pi)^3} \int_{BZ} g(\boldsymbol{k}) \, d\boldsymbol{k} \qquad (8.10)$$

This integral can be approximated by a finite sum over several selected $\boldsymbol{k}$ points in the Brillouin zone. One popular method, developed by Monkhorst and Pack, is used to define the considered $\boldsymbol{k}$ in BZ. It requires the user to specify the number of $\boldsymbol{k}$ points used in each direction in the reciprocal space.

The above-mentioned integral is easy to be calculated for a continuous function. However, this calculation becomes more difficult in the presence of a discontinuity caused by the Fermi surface at the interface between occupied and unoccupied orbitals in the Brillouin zone for metals. To address this issue, two main methods have been developed: the tetrahedron method and the smearing method. The tetrahedron method involves filling the reciprocal space with a set of tetrahedra and then integrating the function over the tetrahedra using interpolation. The smearing method is using a similar function to smooth out any discontinuity. Taking the Fermi-Dirac function as an example,

$$f\left(\frac{k-k_0}{\sigma}\right) = \left[\exp\left(\frac{k-k_0}{\sigma}\right) + 1\right]^{-1} \qquad (8.11)$$

σ is the smearing parameter controlling the shape of the function, with a smaller sigma value resulting in a steeper change across the specified value of k_0.

As for the $u_k(\boldsymbol{r})$ in the real space, it can be also expressed in terms of the plane wave,

$$u_k(\boldsymbol{r}) = \sum_G c_G \exp(i\boldsymbol{G} \cdot \boldsymbol{r})u_k(\boldsymbol{r}) \qquad (8.12)$$

Then the wave function defined by Bloch's theorem can be written as

$$\varphi_k(\boldsymbol{r}) = \sum_G c_{k+G} \exp[i(\boldsymbol{k} + \boldsymbol{G})\boldsymbol{r}] \qquad (8.13)$$

where an infinite number of possible values of $\boldsymbol{G}$ needs to be considered at a single point in $\boldsymbol{k}$ space. To reduce the number of possible values of $\boldsymbol{G}$, the kinetic energy, $E = \frac{\hbar^2}{2m}|\boldsymbol{k} + \boldsymbol{G}|^2$, can be truncated by setting an energy cutoff, $E_{cut} = \frac{\hbar^2}{2m}G_{cut}^2$. This will limit the summation to values of $\boldsymbol{G}$ with kinetic energy equal to or less than the specified energy cutoff.

8.3 Electronic Band Structure

Band theory was developed to approximately describe the electronic state of a periodic solid. The density of states (DOS) is an important quantity used to study the electronic distribution on various bands or atoms, which describes the number of different states at a particular energy that the electrons are allowed to occupy. The definition of DOS is given in equation (8.14). The partial density of states (PDOS) is calculated by projecting the total density of states onto one particular atom or orbital, indicating the contribution of the considered atom or orbital to the total DOS.

$$D(E) = \frac{1}{V}\sum_{i=1}^{N} \delta\big(E - E(\boldsymbol{k}_i)\big) \qquad (8.14)$$

8.4 Computational Methods and Models

In the calculations of REOs bulks introduced in Chapter 2, a stoichiometric dioxide (CeO_2) with Ce in oxidation state (IV) and the sesquioxides (Ln_2O_3) with the metal oxidation state (III) were selected for the investigation. The sesquioxides may occur in three distinct polymorphous forms, hexagonal, monoclinic and cubic[94], separately named by A-type, B-type and C-type, respectively. A-type polymorphs of bulk sesquioxides were adopted for the consideration of consistency, of which the initial lattice parameters of the A-type Ln_2O_3 were taken from the optimization values

obtained by Bo Wu et al.[97] using the PBE method. As for the calculated LnF$_3$, the crystal structures were constructed to keep them isostructural with the YF$_3$ structure, i.e., orthorhombic trifluorides, although hexagonal structure, like that of LaF$_3$, was also found for the trifluorides of Sm, Eu, Ho and Tm.[95-96]

Referred to the calculations of REO surfaces, the La$_2$O$_3$(0001), Ce$_2$O$_3$(0001), Nd$_2$O$_3$(0001) and CeO$_2$(111) surfaces were constructed from the corresponding optimized bulks at the HSE06 level. The p(4×4) La$_2$O$_3$(0001) surface and the p(2×2) Ce$_2$O$_3$(0001) and Nd$_2$O$_3$(0001) surfaces slabs comprised two repeated units, of which only the top one was allowed to relax to the equilibrium geometry. The CeO$_2$(111) surface was modelled as a p(3×3) supercell comprising nine layers, of which the bottom three layers were constrained to the optimized bulk crystal structure. The periodically repeated slabs were separated by a vacuum spacing of 15 Å for all surface models to minimize the spurious interaction between the adjacent slabs.

The Au(221) surface studied in Chapter 6 was modelled by a p(4×1) unit cell with a slab thickness of 7.7 Å and 7.2 Å vacuum space. The atoms of the bottom half of the slab were frozen while the rest of the atoms were allowed to relax without constraints. Along the steps of the surface, double –(Au-O)- chains were constructed.

All calculations in this study were carried out with Vienna *ab initio* simulation package (VASP)[166-167] using the projector augmented wave (PAW)[168-169] method and a plane wave basis set as well as Perdew, Burke, and Ernzerhof (PBE)[170-171] functional. The Heyd-Scuseria-Ernzerhof (HSE06)[172-173] exchange-correlation hybrid functional was also utilized in Chapters 2&3. The simplified rotationally invariant LSDA+U introduced by Dudarev et al.[31] was used for the systems including lanthanide or transition-metal elements. Various k points sets were used for various systems based on Monkhorst-Pack[174] grids in order to integrate within the Brillouin zone. The optimization and single-point energy calculations of the bulk Ln$_2$O$_3$, LnF$_3$ and CeO$_2$ at the PBE+U level were conducted on the basis of (8×8×6), (5×5×8), (7×7×7) meshes, and (12×12×8), (7×7×12), (11×11×11) meshes, respectively, while (6×6×4), (4×4×6)

or (6×6×6) meshes with the grid reduction factor[175] (equal to 2) were used at the HSE06 level. The (2×2×1) and (3×3×1) k-point meshes were used for the $CeO_2(111)$ and $Ce_2O_3(0001)$, $Nd_2O_3(0001)$ surfaces, while a (1×1×1) mesh applied to $La_2O_3(0001)$ surface. The Au(221) surface was modelled on the (5×5×1) k-point mesh. Besides, VASPKIT[176] was applied to post-process the PDOS results of the surfaces. The Multiwfn package[177] was utilized to visualize of the weak interaction of adsorbates on the surfaces via IGM methodology[127].

The cutoff energy of 470 eV was used for most of the calculations of bulk REOs and surfaces, in addition to the cell optimization of bulk REO crystals adopting a large plane-wave cutoff energy up to 600 eV in order to eliminate Pulay stress[178]. For the gold surface calculations, a plane-wave cutoff energy of 415 eV and a larger kinetic energy cutoff of 645 eV were used. The Methfessel-Paxton order 1 smearing scheme[179] with a smearing parameter of 0.05 eV was applied in simulating bulk REOs and gold surface, while Gaussian smearing[179] with the smearing width of 0.01 eV was used for the calculations on the $La_2O_3(0001)$ surface. The dispersion correction using Grimme's D3 approach[125, 180] was included in the surface calculations. The structural minimizations were conducted by the conjugate gradient method until the force acting on each atom was lower than 0.02 eV/Å, accompanied by the convergence of the electronic step reaching 10^{-5} eV. The minimum energy reaction paths were determined by an improved method of the conventional nudged elastic band method (NEB)[181], the climbing-image nudged elastic band method (ci-NEB)[182], and the found transition states were further refined by the dimer[183] method.

In this dissertation, the work function was calculated by $W = -e\emptyset - E_F$, where e, $\emptyset$, and E_F indicate the charge of an electron, the electrostatic potential in the vacuum nearby the surface and the Fermi energy, respectively.[124] The adsorption energy was usually calculated as $E_{ads} = E(\text{adsorption complex}) - E(\text{surface}) - E(\text{adsorbate})$ unless otherwise stated. The band centers of the p-states (ε_p) or d-states (ε_d) are defined

as per equation (8.15).[136] The spin-averaged band centers ε_p or ε_d are defined as given in the equations (8.16).[137]

$$\varepsilon_{p/d} = \frac{\int_{-\infty}^{\infty} n_{p/d}(\varepsilon)\varepsilon d\varepsilon}{\int_{-\infty}^{\infty} n_{p/d}(\varepsilon) d\varepsilon} \qquad (8.15)$$

$$spin\ averaged\ \varepsilon_{p/d} = \sum_\sigma \frac{f_\sigma \varepsilon_{d\sigma}}{\sum_\sigma f_\sigma} \qquad (8.16)$$

where ε represents the energy and $n_{p/d}(\varepsilon)$ denotes the electron density of the p or d orbital in the DOS figures. Furthermore, and σ represents the possible spin configurations, while f_σ indicates the band filling of each spin configuration, which is calculated by integrating the density of states.

Reference

(1) Liu, J.-X.; Su, Y.; Filot, I. A. W.; Hensen, E. J. M. A linear scaling relation for CO oxidation on CeO_2-supported Pd. *J. Am. Chem. Soc.* **2018,** *140*, 4580-4587.

(2) Nie, L.; Mei, D.; Xiong, H.; Peng, B.; Ren, Z.; Hernandez, X. I. P.; DeLaRiva, A.; Wang, M.; Engelhard, M. H.; Kovarik, L. Activation of surface lattice oxygen in single-atom Pt/CeO_2 for low-temperature CO oxidation. *Science* **2017,** *358*, 1419-1423.

(3) Chen, F.; Liu, D.; Zhang, J.; Hu, P.; Gong, X.-Q.; Lu, G. A DFT+ U study of the lattice oxygen reactivity toward direct CO oxidation on the CeO_2(111) and (110) surfaces. *Phys. Chem. Chem. Phys.* **2012,** *14*, 16573-16580.

(4) Guo, Y.; Mei, S.; Yuan, K.; Wang, D.-J.; Liu, H.-C.; Yan, C.-H.; Zhang, Y.-W. Low-temperature CO_2 methanation over CeO_2-supported Ru single atoms, nanoclusters, and nanoparticles competitively tuned by strong metal–support interactions and H-spillover effect. *ACS Catal.* **2018,** *8*, 6203-6215.

(5) Galadima, A.; Muraza, O. Revisiting the oxidative coupling of methane to ethylene in the golden period of shale gas: A review. *J. Ind. Eng. Chem.* **2016,** *37*, 1-13.

(6) Schwach, P.; Pan, X.; Bao, X. Direct conversion of methane to value-added chemicals over heterogeneous catalysts: challenges and prospects. *Chem. Rev.* **2017,** *117*, 8497-8520.

(7) Horn, R.; Schlögl, R. Methane activation by heterogeneous catalysis. *Catal. Lett.* **2014,** *145*, 23-39.

(8) Hammond, C.; Conrad, S.; Hermans, I. Oxidative methane upgrading. *ChemSusChem* **2012,** *5*, 1668-86.

(9) Amenomiya, Y.; Birss, V. I.; Goledzinowski, M.; Galuszka, J.; Sanger, A. R. Conversion of methane by oxidative coupling. *Catal. Rev. - Sci. Eng.* **1990,** *32*, 163-227.

(10) Zavyalova, U.; Holena, M.; Schlögl, R.; Baerns, M. Statistical analysis of past catalytic data on oxidative methane coupling for new insights into the composition of high-performance catalysts. *ChemCatChem* **2011,** *3*, 1935-1947.

(11) Forlani, O.; Rossini, S. Rare earths as catalysts for the oxidative coupling of methane to ethylene. *Mater. Chem. Phys.* **1992,** *31*, 155-158.

(12) Otsuka, K.; Jinno, K.; Morikawa, A. Active and selective catalysts for the synthesis of C_2H_4 and C_2H_6 via oxidative coupling of methane. *J. Catal.* **1986,** *100*, 353-359.

(13) Li, B.; Metiu, H. Dissociation of methane on La_2O_3 surfaces doped with Cu, Mg, or Zn. *J. Phys. Chem. C* **2011,** *115*, 18239-18246.

(14) Li, B.; Metiu, H. DFT studies of oxygen vacancies on undoped and doped La_2O_3 surfaces. *J. Phys. Chem. C* **2010,** *114*, 12234-12244.

(15) Palmer, M. S.; Neurock, M.; Olken, M. M. Periodic density functional theory study of methane activation over La_2O_3: activity of O^{2-}, O^-, O_2^{2-}, oxygen point defect, and Sr^{2+}-doped surface sites. *J. Am. Chem. Soc.* **2002,** *124*, 8452-8461.

(16) Su, Y.-Q.; Liu, J.-X.; Filot, I. A. W.; Zhang, L.; Hensen, E. J. M. Highly active and stable CH_4 oxidation by substitution of Ce^{4+} by two Pd^{2+} ions in $CeO_2(111)$. *ACS Catal.* **2018,** *8*, 6552-6559.

(17) Su, Y.-Q.; Filot, I. A. W.; Liu, J.-X.; Hensen, E. J. M. Stable Pd-doped ceria structures for CH_4 activation and CO oxidation. *ACS Catal.* **2018,** *8*, 75-80.

(18) Mayernick, A. D.; Janik, M. J. Methane activation and oxygen vacancy formation over CeO_2 and Zr, Pd substituted CeO_2 surfaces. *J. Phys. Chem. C* **2008,** *112*, 14955-14964.

(19) Tian, D.; Li, k.; Wei, Y.; Zhu, X.; Zeng, C.; Cheng, X.; Zheng, Y.; Wang, H. DFT insight into the oxygen vacancies formation and CH_4 activation over CeO_2 surfaces modified by transition metals (Fe, Co and Ni). *Phys. Chem. Chem. Phys.* **2018,** *20*, 11912-11929.

(20) Cohen, A. J.; Mori-Sánchez, P.; Yang, W. Challenges for density functional theory. *Chem. Rev.* **2012,** *112*, 289-320.

(21) Jiang, H.; Rinke, P.; Scheffler, M. Electronic properties of lanthanide oxides from the GW perspective. *Phys. Rev. B* **2012,** *86*, 125115.

(22) Jiang, H.; Gomez-Abal, R. I.; Rinke, P.; Scheffler, M. Localized and itinerant states in lanthanide oxides united by GW@LDA+U. *Phys. Rev. Lett.* **2009,** *102*, 126403.

(23) Held, K. Electronic structure calculations using dynamical mean field theory. *Adv. Phys.* **2007,** *56*, 829-926.

(24) Kotliar, G.; Savrasov, S. Y.; Haule, K.; Oudovenko, V. S.; Parcollet, O.; Marianetti, C. Electronic structure calculations with dynamical mean-field theory. *Rev. Mod. Phys.* **2006,** *78*, 865.

(25) Anisimov, V. I.; Zaanen, J.; Andersen, O. K. Band theory and Mott insulators: Hubbard U instead of Stoner I. *Phys. Rev. B* **1991,** *44*, 943.

(26) Lu, J.-B.; Cantu, D. C.; Nguyen, M.-T.; Li, J.; Glezakou, V.-A.; Rousseau, R. Norm-conserving pseudopotentials and basis sets to explore lanthanide chemistry in complex environments. *J. Chem. Theory Comput.* **2019,** *15*, 5987-5997.

(27) Krcha, M. D.; Janik, M. J. Challenges in the use of density functional theory to examine catalysis by M-doped ceria surfaces. *Int. J. Quantum Chem.* **2014,** *114*, 8-13.

(28) Wang, C.-X.; Li, Y.; Li, Z.-F.; Liu, Z.-J.; Valeev, E. F.; Moskaleva, L. V. Combined relativistic ab initio multireference and experimental study of the electronic structure of terbium luminescent compound. *J. Phys. Chem. A* **2020,** *124*, 82-89.

(29) Brugnoli, L.; Ferrari, A. M.; Civalleri, B.; Pedone, A.; Menziani, M. C. Assessment of density functional approximations for highly correlated oxides: the case of CeO_2 and Ce_2O_3. *J. Chem. Theory Comput.* **2018,** *14*, 4914-4927.

(30) Da Silva, J. L.; Ganduglia-Pirovano, M. V.; Sauer, J.; Bayer, V.; Kresse, G. Hybrid functionals applied to rare-earth oxides: the example of ceria. *Phys. Rev. B* **2007,** *75*, 045121.

(31) Dudarev, S.; Botton, G.; Savrasov, S.; Humphreys, C.; Sutton, A. Electron-energy-loss spectra and the structural stability of nickel oxide: an LSDA+U study. *Phys. Rev. B* **1998,** *57*, 1505.

(32) Ganduglia-Pirovano, M. V.; Da Silva, J. L.; Sauer, J. Density-functional calculations of the structure of near-surface oxygen vacancies and electron localization on CeO_2(111). *Phys. Rev. Lett.* **2009,** *102*, 026101.

(33) Castleton, C.; Kullgren, J.; Hermansson, K. Tuning LDA+U for electron localization and structure at oxygen vacancies in ceria. *J. Chem. Phys.* **2007,** *127*, 244704.

(34) Castleton, C. W.; Lee, A.; Kullgren, J. Benchmarking DFT functionals for polarons in oxides: properties of CeO_2. *J. Phys. Chem. C* **2019,** *123*, 5164-5175.

(35) Murgida, G. E.; Ferrari, V.; Ganduglia-Pirovano, M. V.; Llois, A. M. Ordering of oxygen vacancies and excess charge localization in bulk ceria: a DFT+U study. *Phys. Rev. B* **2014,** *90*, 115120.

(36) Loschen, C.; Migani, A.; Bromley, S. T.; Illas, F.; Neyman, K. M. Density functional studies of model cerium oxide nanoparticles. *Phys. Chem. Chem. Phys.* **2008,** *10*, 5730-5738.

(37) Branda, M. M.; Loschen, C.; Neyman, K. M.; Illas, F. Atomic and electronic structure of cerium oxide stepped model surfaces. *J. Phys. Chem. C* **2008,** *112*, 17643-17651.

(38) Loschen, C.; Carrasco, J.; Neyman, K. M.; Illas, F. First-principles LDA+U and GGA+U study of cerium oxides: dependence on the effective U parameter. *Phys. Rev. B* **2007,** *75*, 035115.

(39) Andersson, D. A.; Simak, S. I.; Johansson, B.; Abrikosov, I. A.; Skorodumova, N. V. Modeling of CeO_2, Ce_2O_3, and CeO_{2-x} in the LDA+U formalism. *Phys. Rev. B* **2007,** *75*.

(40) Fabris, S.; de Gironcoli, S.; Baroni, S.; Vicario, G.; Balducci, G. Taming multiple valency with density functionals: a case study of defective ceria. *Phys. Rev. B* **2005,** *71*, 041102.

(41) Capdevila-Cortada, M.; Łodziana, Z.; López, N. Performance of DFT+U approaches in the study of catalytic materials. *ACS Catal.* **2016,** *6*, 8370-8379.

(42) Fabris, S.; Vicario, G.; Balducci, G.; de Gironcoli, S.; Baroni, S. Electronic and atomistic structures of clean and reduced ceria surfaces. *J. Phys. Chem. B* **2005,** *109*, 22860-22867.

(43) Cococcioni, M.; De Gironcoli, S. Linear response approach to the calculation of the effective interaction parameters in the LDA+U method. *Phys. Rev. B* **2005,** *71*, 035105.

(44) Podkolzin, S. G.; Stangland, E. E.; Jones, M. E.; Peringer, E.; Lercher, J. A. Methyl chloride production from methane over lanthanum-based catalysts. *J. Am. Chem. Soc.* **2007,** *129*, 2569-2576.

(45) Song, J.; Duan, X.; Zhang, W. Methane dry reforming over mesoporous La_2O_3 supported Ni catalyst for syngas production. *Microporous Mesoporous Mater.* **2021,** *310*, 110587.

(46) Xu, L.; Liu, W.; Zhang, X.; Tao, L.; Xia, L.; Xu, X.; Song, J.; Zhou, W.; Fang, X.; Wang, X. Ni/La$_2$O$_3$ catalysts for dry reforming of methane: insights into the factors improving the catalytic performance. *ChemCatChem* **2019,** *11*, 2887-2899.

(47) Wang, S.; Li, S.; Dixon, D. A. Mechanism of selective and complete oxidation in La$_2$O$_3$-catalyzed oxidative coupling of methane. *Catal. Sci. Technol.* **2020,** *10*, 2602-2614.

(48) Wang, Z.-Q.; Wang, D.; Gong, X.-Q. Strategies to improve the activity while maintaining the selectivity of oxidative coupling of methane at La$_2$O$_3$: a density functional theory study. *ACS Catal.* **2019,** *10*, 586-594.

(49) Gayen, P.; Saha, S.; Bhattacharyya, K.; Ramani, V. K. Oxidation state and oxygen-vacancy-induced work function controls bifunctional oxygen electrocatalytic activity. *ACS Catal.* **2020,** *10*, 7734-7746.

(50) Yang, J.; Hu, S.; Fang, Y.; Hoang, S.; Li, L.; Yang, W.; Liang, Z.; Wu, J.; Hu, J.; Xiao, W.; Pan, C.; Luo, Z.; Ding, J.; Zhang, L.; Guo, Y. Oxygen vacancy promoted O$_2$ activation over perovskite oxide for low-temperature CO oxidation. *ACS Catal.* **2019,** *9*, 9751-9763.

(51) Liu, B.; Li, C.; Zhang, G.; Yao, X.; Chuang, S. S. C.; Li, Z. Oxygen vacancy promoting dimethyl carbonate synthesis from CO$_2$ and methanol over Zr-doped CeO$_2$ nanorods. *ACS Catal.* **2018,** *8*, 10446-10456.

(52) Younis, A.; Shirsath, S. E.; Shabbir, B.; Li, S. Controllable dynamics of oxygen vacancies through extrinsic doping for superior catalytic activities. *Nanoscale* **2018,** *10*, 18576-18585.

(53) Wang, H.; Yong, D.; Chen, S.; Jiang, S.; Zhang, X.; Shao, W.; Zhang, Q.; Yan, W.; Pan, B.; Xie, Y. Oxygen-vacancy-mediated exciton dissociation in BiOBr for boosting charge-carrier-involved molecular oxygen activation. *J. Am. Chem. Soc.* **2018,** *140*, 1760-1766.

(54) Choudhary, V. R.; Rane, V. H. Acidity/basicity of rare-earth oxides and their catalytic activity in oxidative coupling of methane to C2-hydrocarbons. *J. Catal.* **1991,** *130*, 411-422.

(55) Maitra, A.; Campbell, I.; Tyler, R. Influence of basicity on the catalytic activity for oxidative coupling of methane. *Appl. Catal. A* **1992,** *85*, 27-46.

(56) Kuś, S.; Otremba, M.; Taniewski, M. The catalytic performance in oxidative coupling of methane and the surface basicity of La$_2$O$_3$, Nd$_2$O$_3$, ZrO2 and Nb2O5☆. *Fuel* **2003,** *82*, 1331-1338.

(57) Chu, C.; Zhao, Y.; Li, S.; Sun, Y. Correlation between the acid-base properties of the La$_2$O$_3$ catalyst and its methane reactivity. *Phys. Chem. Chem. Phys.* **2016,** *18*, 16509-16517.

(58) Chu, C.; Zhao, Y.; Li, S.; Sun, Y. CO$_2$ chemisorption and its effect on methane activation in La$_2$O$_3$-catalyzed oxidative coupling of methane. *J. Phys. Chem. C* **2016,** *120*, 2737-2746.

(59) Chrétien, S.; Metiu, H. Hydrogen dissociative adsorption on lanthana: polaron formation and the role of acid–base interactions. *J. Phys. Chem. C* **2015,** *119*, 19876-19882.

(60) Chrétien, S.; Metiu, H. Acid–base interaction and its role in alkane dissociative chemisorption on oxide surfaces. *J. Phys. Chem. C* **2014,** *118*, 27336-27342.

(61) Metiu, H.; Chrétien, S.; Hu, Z.; Li, B.; Sun, X. Chemistry of Lewis acid–base pairs on oxide surfaces. *J. Phys. Chem. C* **2012,** *116*, 10439-10450.

(62) Li, B.; Metiu, H. Does halogen adsorption activate the oxygen atom on an oxide surface? I. A study of Br_2 and HBr adsorption on La_2O_3 and La_2O_3 doped with Mg or Zr. *J. Phys. Chem. C* **2012,** *116*, 4137-4148.

(63) Venezia, A. M.; Pantaleo, G.; Longo, A.; Di Carlo, G.; Casaletto, M. P.; Liotta, F. L.; Deganello, G. Relationship between structure and CO oxidation activity of ceria-supported gold catalysts. *J. Phys. Chem. B* **2005,** *109*, 2821-2827.

(64) Wang, Y.-G.; Mei, D.; Glezakou, V.-A.; Li, J.; Rousseau, R. Dynamic formation of single-atom catalytic active sites on ceria-supported gold nanoparticles. *Nat. Commun.* **2015,** *6*, 6511.

(65) Kim, H. Y.; Henkelman, G. CO oxidation at the interface of Au nanoclusters and the stepped-CeO_2(111) surface by the Mars–van Krevelen mechanism. *J. Phys. Chem. Lett.* **2013,** *4*, 216-221.

(66) Li, Y.; Li, S.; Bäumer, M.; Moskaleva, L. V. Transient Au–CO complexes promote the activity of an inverse ceria/gold catalyst: an insight from ab initio molecular dynamics. *J. Phys. Chem. C* **2021,** *125*, 26406-26417.

(67) Yang, F.; Graciani, J.; Evans, J.; Liu, P.; Hrbek, J.; Sanz, J. F.; Rodriguez, J. A. CO oxidation on inverse CeO_x/Cu(111) catalysts: high catalytic activity and ceria-promoted dissociation of O_2. *J. Am. Chem. Soc.* **2011,** *133*, 3444-3451.

(68) Wittstock, A.; Zielasek, V.; Biener, J.; Friend, C. M.; Bäumer, M. Nanoporous gold catalysts for selective gas-phase oxidative coupling of methanol at low temperature. *Science* **2010,** *327*, 319-322.

(69) Kosuda, K. M.; Wittstock, A.; Friend, C. M.; Bäumer, M. Oxygen-mediated coupling of alcohols over nanoporous gold catalysts at ambient pressures. *Angew. Chem. Int. Ed.* **2012,** *51*, 1698-1701.

(70) Zhang, A.; Chen, Y.; Yang, Z.; Ma, S.; Huang, Y.; Richter, G.; Schützendübe, P.; Zhong, C.; Wang, Z. Enhanced electrocatalytic activities toward the ethanol oxidation of nanoporous gold prepared via solid-phase reaction. *ACS Appl. Energy Mater.* **2020,** *3*, 336-343.

(71) Barakat, T.; Rooke, J. C.; Genty, E.; Cousin, R.; Siffert, S.; Su, B.-L. Gold catalysts in environmental remediation and water-gas shift technologies. *Energy Environ. Sci.* **2013,** *6*, 371-391.

(72) Rodriguez, J. A.; Senanayake, S. D.; Stacchiola, D.; Liu, P.; Hrbek, J. The activation of gold and the water–gas shift reaction: Insights from studies with model catalysts. *Acc. Chem. Res.* **2014,** *47*, 773-782.

(73) Zielasek, V.; Jürgens, B.; Schulz, C.; Biener, J.; Biener, M. M.; Hamza, A. V.; Bäumer, M. Gold catalysts: nanoporous gold foams. *Angew. Chem. Int. Ed.* **2006,** *45*, 8241-8244.

(74) Xu, C.; Su, J.; Xu, X.; Liu, P.; Zhao, H.; Tian, F.; Ding, Y. Low temperature CO oxidation over unsupported nanoporous gold. *J. Am. Chem. Soc.* **2007,** *129*, 42-43.

(75) Qiao, B.; Liang, J.-X.; Wang, A.; Liu, J.; Zhang, T. Single atom gold catalysts for low-temperature CO oxidation. *Chinese J. Catal.* **2016,** *37*, 1580-1586.

(76) Gottfried, J. M.; Schmidt, K. J.; Schroeder, S. L. M.; Christmann, K. Spontaneous and electron-induced adsorption of oxygen on Au(110)-(1×2). *Surf. Sci.* **2002,** *511*, 65-82.

(77) Xu, Y.; Mavrikakis, M. Adsorption and dissociation of O_2 on gold surfaces: effect of steps and strain. *J. Phys. Chem. B* **2003,** *107*, 9298-9307.

(78) Pal, R.; Wang, L.-M.; Pei, Y.; Wang, L.-S.; Zeng, X. C. Unraveling the mechanisms of O_2 activation by size-selected gold clusters: Transition from superoxo to peroxo chemisorption. *J. Am. Chem. Soc.* **2012,** *134*, 9438-9445.

(79) Tomaschun, G.; Dononelli, W.; Li, Y.; Bäumer, M.; Klüner, T.; Moskaleva, L. V. Methanol oxidation on the Au(310) surface: a theoretical study. *J. Catal.* **2018,** *364*, 216-227.

(80) Fajín, J. L. C.; Cordeiro, M. N. D. S.; Gomes, J. R. B. Adsorption of atomic and molecular oxygen on the Au(321) surface: DFT study. *J. Phys. Chem. C* **2007,** *111*, 17311-17321.

(81) Fajín, J. L. C.; Cordeiro, M. N. D. S.; Gomes, J. R. B. On the theoretical understanding of the unexpected O_2 activation by nanoporous gold. *Chem. Commun.* **2011,** *47*, 8403-8405.

(82) Moskaleva, L. V.; Röhe, S.; Wittstock, A.; Zielasek, V.; Klüner, T.; Neyman, K. M.; Bäumer, M. Silver residues as a possible key to a remarkable oxidative catalytic activity of nanoporous gold. *Phys. Chem. Chem. Phys.* **2011,** *13*, 4529-4539.

(83) Sun, K.; Kohyama, M.; Tanaka, S.; Takeda, S. Theoretical study of atomic oxygen on gold surface by Hückel theory and DFT calculations. *J. Phys. Chem. A* **2012,** *116*, 9568-9573.

(84) Li, Y.; Dononelli, W.; Moreira, R.; Risse, T.; Bäumer, M.; Klüner, T.; Moskaleva, L. V. Oxygen-driven surface evolution of nanoporous gold: insights from ab initio molecular dynamics and auger electron spectroscopy. *J. Phys. Chem. C* **2017,** *122*, 5349-5357.

(85) Hiebel, F.; Montemore, M. M.; Kaxiras, E.; Friend, C. M. Direct visualization of quasi-ordered oxygen chain structures on Au(110)-(1×2). *Surf. Sci.* **2016,** *650*, 5-10.

(86) Masatake, H.; Tetsuhiko, K.; Hiroshi, S.; Nobumasa, Y. Novel gold catalysts for the oxidation of carbon monoxide at a temperature far below 0 °C. *Chem. Lett.* **1987,** *16*, 405-408.

(87) Haruta, M.; Yamada, N.; Kobayashi, T.; Iijima, S. Gold catalysts prepared by coprecipitation for low-temperature oxidation of hydrogen and of carbon monoxide. *J. Catal.* **1989,** *115*, 301-309.

(88) Moskaleva, L. V.; Zielasek, V.; Klüner, T.; Neyman, K. M.; Bäumer, M. CO oxidation by co-adsorbed atomic O on the Au(321) surface with Ag impurities: A mechanistic study from first-principles calculations. *Chem. Phys. Lett.* **2012,** *525-526*, 87-91.

(89) Dononelli, W.; Moskaleva, L. V.; Klüner, T. CO oxidation over unsupported group 11 metal catalysts: new mechanistic insight from first-principles. *J. Phys. Chem. C* **2019,** *123*, 7818-7830.

(90) Liu, Z.-P.; Hu, P.; Alavi, A. Catalytic role of gold in gold-based catalysts: a density functional theory study on the CO oxidation on gold. *J. Am. Chem. Soc.* **2002,** *124*, 14770-14779.

(91) Fajin, J. L.; Cordeiro, M. N. D.; Gomes, J. R. DFT study of the CO oxidation on the Au(321) surface. *J. Phys. Chem. C* **2008,** *112*, 17291-17302.

(92) Deng, X.; Min, B. K.; Guloy, A.; Friend, C. M. Enhancement of O_2 dissociation on Au(111) by adsorbed oxygen: Implications for oxidation catalysis. *J. Am. Chem. Soc.* **2005,** *127*, 9267-9270.

(93) Baker, T. A.; Friend, C. M.; Kaxiras, E. Local bonding effects in the oxidation of CO on oxygen-covered Au(111) from ab initio molecular dynamics simulations. *J. Chem. Theory Comput.* **2010,** *6*, 279-287.

(94) Goldschmidt, V. M.; Ulrich, F.; Barth, T. Skrifter Norske Videnskaps-Akad. Oslo,. *I. Mat. Nat. Kl* **1926,** *8*.

(95) Flotow, H. E.; O'Hare, P. A. G. Thermodynamics of the lanthanide trifluorides. IV. The heat capacities of gadolinium trifluoride GdF_3, lutetium trifluoride LuF_3, and yttrium trifluoride YF_3 from 5 to 350 °K. *J. Chem. Phys.* **1981,** *74*, 3046-3055.

(96) Zalkin, A.; Templeton, D. The crystal structures of YF_3 and related compounds. *J. Am. Chem. Soc.* **1953,** *75*, 2453-2458.

(97) Wu, B.; Zinkevich, M.; Aldinger, F.; Wen, D.; Chen, L. Ab initio study on structure and phase transition of A- and B-type rare-earth sesquioxides Ln_2O_3 (Ln=La–Lu, Y, and Sc) based on density function theory. *J. Solid State Chem.* **2007,** *180*, 3280-3287.

(98) Hirosaki, N.; Ogata, S.; Kocer, C. Ab initio calculation of the crystal structure of the lanthanide Ln_2O_3 sesquioxides. *J. Alloys Compd.* **2003,** *351*, 31-34.

(99) Palmer, M. S.; Neurock, M.; Olken, M. M. Periodic density functional theory study of the dissociative adsorption of molecular oxygen over La_2O_3. *J. Phys. Chem. B* **2002,** *106*, 6543-6547.

(100) Faucher, M.; Pannetier, J.; Charreire, Y.; Caro, P. Refinement of the Nd_2O_3 and Nd_2O_2S structures at 4 K. *Acta Crystallogr. B* **1982,** *38*, 344-346.

(101) Greis, O.; Ziel, R.; Breidenstein, B.; Haase, A.; Petzel, T. The crystal structure of the low-temperature A-type modification of Pr_2O_3 from X-ray powder and electron single crystal diffraction. *J. Alloys Compd.* **1995,** *216*, 255-258.

(102) Hay, P. J.; Martin, R. L.; Uddin, J.; Scuseria, G. E. Theoretical study of CeO_2 and Ce_2O_3 using a screened hybrid density functional. *J. Chem. Phys.* **2006,** *125*, 034712.

(103)   Bärnighausen, H.; Schiller, G. The crystal structure of A-Ce_2O_3. *J. Less Common Met.* **1985,** *110*, 385-390.

(104)   Pinto, H.; Mintz, M.; Melamud, M.; Shaked, H. Neutron diffraction study of Ce_2O_3. *Phys. Lett. A* **1982,** *88*, 81-83.

(105)   Birch, F. Finite elastic strain of cubic crystals. *Phys. Rev.* **1947,** *71*, 809.

(106)   Birch, F. The effect of pressure upon the elastic parameters of isotropic solids, according to Murnaghan's theory of finite strain. *J. Appl. Phys.* **1938,** *9*, 279-288.

(107)   Rossignol, S.; Gérard, F.; Mesnard, D.; Kappenstein, C.; Duprez, D. Structural changes of Ce–Pr–O oxides in hydrogen: a study by in situ X-ray diffraction and Raman spectroscopy. *J. Mater. Chem.* **2003,** *13*, 3017-3020.

(108)   Duclos, S. J.; Vohra, Y. K.; Ruoff, A. L.; Jayaraman, A.; Espinosa, G. High-pressure x-ray diffraction study of CeO_2 to 70 GPa and pressure-induced phase transformation from the fluorite structure. *Phys. Rev. B* **1988,** *38*, 7755.

(109)   Gerward, L.; Olsen, J. S. Powder diffraction analysis of cerium dioxide at high pressure. *Powder Diffr.* **1993,** *8*, 127-129.

(110)   Dronskowski, R.; Blöchl, P. E. Crystal orbital Hamilton populations (COHP): energy-resolved visualization of chemical bonding in solids based on density-functional calculations. *J. Phys. Chem.* **1993,** *97*, 8617-8624.

(111)   Maintz, S.; Deringer, V. L.; Tchougréeff, A. L.; Dronskowski, R. Analytic projection from plane-wave and PAW wavefunctions and application to chemical-bonding analysis in solids. *J. Comput. Chem.* **2013,** *34*, 2557-2567.

(112)   Maintz, S.; Deringer, V. L.; Tchougréeff, A. L.; Dronskowski, R. LOBSTER: A tool to extract chemical bonding from plane-wave based DFT. *J. Comput. Chem.* **2016,** *37*, 1030-1035.

(113)   Konings, R. J.; Beneš, O.; Kovács, A.; Manara, D.; Sedmidubský, D.; Gorokhov, L.; Iorish, V. S.; Yungman, V.; Shenyavskaya, E.; Osina, E. The thermodynamic properties of the *f*-elements and their compounds. Part 2. The lanthanide and actinide oxides. *J. Phys. Chem. Ref. Data* **2014,** *43*, 013101.

(114)   Johnson, G. K.; Pennell, R. G.; Kim, K.-Y.; Hubbard, W. N. Thermochemistry of rare-earth trifluorides I. Fluorine bomb calorimetric determination of the enthalpies of formation of LaF_3, PrF_3, NdF_3, GdF_3, DyF_3, HoF_3, and ErF_3. *J. Chem. Thermodyn.* **1980,** *12*, 125-136.

(115)   Chase, M. W., NIST-JANAF thermochemical tables. American Institute of Physics for the National Institute of Standards and Technology: New York, USA, 1998.

(116)   Du, D.; Wolf, M. J.; Hermansson, K.; Broqvist, P. Screened hybrid functionals applied to ceria: effect of Fock exchange. *Phys. Rev. B* **2018,** *97*, 235203.

(117)   Lutfalla, S.; Shapovalov, V.; Bell, A. T. Calibration of the DFT/GGA+U method for determination of reduction energies for transition and rare earth metal oxides of Ti, V, Mo, and Ce. *J. Chem. Theory Comput.* **2011,** *7*, 2218-2223.

(118)   Bader, R. F. W., *Atoms in molecules - a quantum theory*. Oxford University Press: Oxford, 1990.

(119) Yu, M.; Trinkle, D. R. Accurate and efficient algorithm for Bader charge integration. *J. Chem. Phys.* **2011,** *134*, 064111.

(120) Tang, W.; Sanville, E.; Henkelman, G. A grid-based Bader analysis algorithm without lattice bias. *J. Phys.: Condens. Matter* **2009,** *21*, 084204.

(121) Sanville, E.; Kenny, S. D.; Smith, R.; Henkelman, G. Improved grid-based algorithm for Bader charge allocation. *J. Comput. Chem.* **2007,** *28*, 899-908.

(122) Henkelman, G.; Arnaldsson, A.; Jónsson, H. A fast and robust algorithm for Bader decomposition of charge density. *Comput. Mater. Sci.* **2006,** *36*, 354-360.

(123) Kozlov, S. M.; Neyman, K. M. O vacancies on steps on the CeO_2(111) surface. *Phys. Chem. Chem. Phys.* **2014,** *16*, 7823-7829.

(124) Kittel, C.; McEuen, P.; McEuen, P., *Introduction to solid state physics*. Wiley: New York, 1996; Vol. 8.

(125) Grimme, S.; Antony, J.; Ehrlich, S.; Krieg, H. A consistent and accurate ab initio parametrization of density functional dispersion correction (DFT-D) for the 94 elements H-Pu. *J. Chem. Phys.* **2010,** *132*, 154104.

(126) Fernández-Torre, D.; Kośmider, K.; Carrasco, J.; Ganduglia-Pirovano, M. V.; Pérez, R. Insight into the adsorption of water on the clean CeO_2(111) surface with van der Waals and hybrid density functionals. *J. Phys. Chem. C* **2012,** *116*, 13584-13593.

(127) Lefebvre, C.; Rubez, G.; Khartabil, H.; Boisson, J.-C.; Contreras-García, J.; Hénon, E. Accurately extracting the signature of intermolecular interactions present in the NCI plot of the reduced density gradient versus electron density. *Phys. Chem. Chem. Phys.* **2017,** *19*, 17928-17936.

(128) Finazzi, E.; Di Valentin, C.; Pacchioni, G.; Selloni, A. Excess electron states in reduced bulk anatase TiO_2: comparison of standard GGA, GGA+ U, and hybrid DFT calculations. *J. Chem. Phys.* **2008,** *129*, 154113.

(129) Krcha, M. D.; Janik, M. J. Examination of oxygen vacancy formation in Mn-doped CeO_2(111) using DFT+U and the hybrid functional HSE06. *Langmuir* **2013,** *29*, 10120-10131.

(130) Franchini, C.; Podloucky, R.; Paier, J.; Marsman, M.; Kresse, G. Ground-state properties of multivalent manganese oxides: density functional and hybrid density functional calculations. *Phys. Rev. B* **2007,** *75*, 195128.

(131) Rollmann, G.; Entel, P.; Rohrbach, A.; Hafner, J. High-pressure characteristics of α-Fe_2O_3 using DFT+ U. *Phase Transit.* **2005,** *78*, 251-258.

(132) Wang, L.; Maxisch, T.; Ceder, G. Oxidation energies of transition metal oxides within the GGA+ U framework. *Phys. Rev. B* **2006,** *73*, 195107.

(133) Jia, Y. Q. Crystal radii and effective ionic radii of the rare earth ions. *J. Solid State Chem.* **1991,** *95*, 184-187.

(134) Shannon, R. Revised effective ionic radii and systematic studies of interatomic distances in halides and chalcogenides. *Acta Crystallographica Section A* **1976,** *32*, 751-767.

(135)   Kiani, D.; Sourav, S.; Baltrusaitis, J.; Wachs, I. E. Oxidative coupling of methane (OCM) by SiO_2-supported tungsten oxide catalysts promoted with Mn and Na. *ACS Catal.* **2019,** *9*, 5912-5928.

(136)   Ruban, A.; Hammer, B.; Stoltze, P.; Skriver, H. L.; Nørskov, J. K. Surface electronic structure and reactivity of transition and noble metals. *J. Mol. Catal. A: Chem.* **1997,** *115*, 421-429.

(137)   Bhattacharjee, S.; Waghmare, U. V.; Lee, S.-C. An improved *d*-band model of the catalytic activity of magnetic transition metal surfaces. *Sci. Rep.* **2016,** *6*, 35916.

(138)   Nørskov, J. K.; Abild-Pedersen, F.; Studt, F.; Bligaard, T. Density functional theory in surface chemistry and catalysis. *Proc. Natl. Acad. Sci. U. S. A.* **2011,** *108*, 937-943.

(139)   Nørskov, J. K.; Bligaard, T.; Rossmeisl, J.; Christensen, C. H. Towards the computational design of solid catalysts. *Nat. Chem.* **2009,** *1*, 37-46.

(140)   Calle-Vallejo, F.; Inoglu, N. G.; Su, H.-Y.; Martínez, J. I.; Man, I. C.; Koper, M. T. M.; Kitchin, J. R.; Rossmeisl, J. Number of outer electrons as descriptor for adsorption processes on transition metals and their oxides. *Chem. Sci.* **2013,** *4*, 1245-1249.

(141)   Xu, Z.; Kitchin, J. R. Relationships between the surface electronic and chemical properties of doped 4*d* and 5*d* late transition metal dioxides. *J. Chem. Phys.* **2015,** *142*, 104703.

(142)   Grimaud, A.; Hong, W. T.; Shao-Horn, Y.; Tarascon, J. M. Anionic redox processes for electrochemical devices. *Nat. Mater.* **2016,** *15*, 121-126.

(143)   Grimaud, A.; May, K. J.; Carlton, C. E.; Lee, Y.-L.; Risch, M.; Hong, W. T.; Zhou, J.; Shao-Horn, Y. Double perovskites as a family of highly active catalysts for oxygen evolution in alkaline solution. *Nat. Commun.* **2013,** *4*, 2439.

(144)   Jacobs, R.; Hwang, J.; Shao-Horn, Y.; Morgan, D. Assessing correlations of perovskite catalytic performance with electronic structure descriptors. *Chem. Mater.* **2019,** *31*, 785-797.

(145)   Dickens, C. F.; Montoya, J. H.; Kulkarni, A. R.; Bajdich, M.; Nørskov, J. K. An electronic structure descriptor for oxygen reactivity at metal and metal-oxide surfaces. *Surf. Sci.* **2019,** *681*, 122-129.

(146)   Elkins, T. W.; Roberts, S. J.; Hagelin-Weaver, H. E. Effects of alkali and alkaline-earth metal dopants on magnesium oxide supported rare-earth oxide catalysts in the oxidative coupling of methane. *Appl. Catal. A* **2016,** *528*, 175-190.

(147)   Elkins, T. W.; Neumann, B.; Baeumer, M.; Hagelin-Weaver, H. E. Effects of Li doping on MgO-supported Sm_2O_3 and TbO_x catalysts in the oxidative coupling of methane. *ACS Catal.* **2014,** *4*, 1972-1990.

(148)   Gong, J.; Mullins, C. B. Surface science investigations of oxidative chemistry on gold. *Acc. Chem. Res.* **2009,** *42*, 1063-1073.

(149)   Pan, M.; Gong, J.; Dong, G.; Mullins, C. B. Model studies with gold: a versatile oxidation and hydrogenation catalyst. *Acc. Chem. Res.* **2014,** *47*, 750-760.

(150)   Wang, L.-C.; Personick, M. L.; Karakalos, S.; Fushimi, R.; Friend, C. M.; Madix, R. J. Active sites for methanol partial oxidation on nanoporous gold catalysts. *J. Catal.* **2016,** *344*, 778-783.

(151)   Hiebel, F.; Karakalos, S.; Xu, Y.; Friend, C. M.; Madix, R. J. Structural differentiation of the reactivity of alcohols with active oxygen on Au(110). *Top. Catal.* **2018,** *61*, 299-307.

(152)   Xu, F.; Montemore, M. M.; O'Connor, C. R.; Muramoto, E.; van Spronsen, M. A.; Madix, R. J.; Friend, C. M. Oxygen adsorption on spontaneously reconstructed Au(511). *Surf. Sci.* **2019,** *679*, 296-303.

(153)   Feldt, C. D.; Gimm, T.; Moreira, R.; Riedel, W.; Risse, T. Methanol oxidation on Au(332): an isothermal pulsed molecular beam study. *Phys. Chem. Chem. Phys.* **2021,** *23*, 21599-21605.

(154)   Feldt, C. D.; Kirschbaum, T.; Low, J. L.; Riedel, W.; Risse, T. Methanol oxidation on Au(332): methyl formate selectivity and surface deactivation under isothermal conditions. *Catal. Sci. Technol.* **2022,** *12*, 1418-1428.

(155)   Landmann, M.; Rauls, E.; Schmidt, W. G. Chainlike Au−O structures on Au(110)-(1 × r) surfaces calculated from first principles. *J. Phys. Chem. C* **2009,** *113*, 5690-5699.

(156)   Montemore, M. M.; Madix, R. J.; Kaxiras, E. How does nanoporous gold dissociate molecular oxygen? *J. Phys. Chem. C* **2016,** *120*, 16636-16640.

(157)   Li, Y.; Li, S.; Bäumer, M.; Ivanova-Shor, E. A.; Moskaleva, L. V. What changes on the inverse catalyst? Insights from CO oxidation on Au-supported ceria nanoparticles using ab initio molecular dynamics. *ACS Catal.* **2020,** *10*, 3164-3174.

(158)   Green, I. X.; Tang, W.; Neurock, M.; Yates Jr, J. T. Spectroscopic observation of dual catalytic sites during oxidation of CO on a Au/TiO_2 catalyst. *Science* **2011,** *333*, 736-739.

(159)   Rodriguez, J. A.; Ma, S.; Liu, P.; Hrbek, J.; Evans, J.; Perez, M. Activity of CeO_x and TiO_x nanoparticles grown on Au(111) in the water-gas shift reaction. *Science* **2007,** *318*, 1757-1760.

(160)   Gómez, E. d. V.; Burgos Paci, M. A.; Amaya-Roncancio, S.; Avalle, L. a. B.; Cecilia Gimenez, M. Adsorption and diffusion of O atoms on metallic (100) surfaces. Cluster and periodic slab approaches. *Comput. Theor. Chem.* **2022,** *1208*, 113556.

(161)   Blyholder, G. Molecular orbital view of chemisorbed carbon monoxide. *J. Phys. Chem.* **1964,** *68*, 2772-2777.

(162)   Fang, L.; Chen, T.; Meng, Y.; Zhang, L.; Zhou, X.; Pan, G.; Ni, Z.; Xia, S. Size effect of CO_2 adsorption onto Au cluster-functionalized monolayer ZnAl layered double hydroxides: Insights from first-principles computations. *Appl. Surf. Sci.* **2020,** *525*, 146612.

(163)   Dononelli, W.; Tomaschun, G.; Klüner, T.; Moskaleva, L. V. Understanding oxygen activation on nanoporous gold. *ACS Catal.* **2019,** *9*, 5204-5216.

(164)   Lee, J. D.; Miller, J. B.; Shneidman, A. V.; Sun, L.; Weaver, J. F.; Aizenberg, J.; Biener, J.; Boscoboinik, J. A.; Foucher, A. C.; Frenkel, A. I.; van der Hoeven, J. E.

S.; Kozinsky, B.; Marcella, N.; Montemore, M. M.; Ngan, H. T.; O'Connor, C. R.; Owen, C. J.; Stacchiola, D. J.; Stach, E. A.; Madix, R. J.; Sautet, P.; Friend, C. M. Dilute alloys based on Au, Ag, or Cu for efficient catalysis: from synthesis to active sites. *Chem. Rev.* **2022,** *122*, 8758-8808.

(165)   Biener, J.; Biener, M. M.; Madix, R. J.; Friend, C. M. Nanoporous gold: understanding the origin of the reactivity of a 21st century catalyst made by pre-Columbian technology. *ACS Catal.* **2015,** *5*, 6263-6270.

(166)   Kresse, G.; Furthmüller, J. Efficiency of ab-initio total energy calculations for metals and semiconductors using a plane-wave basis set. *Comput. Mater. Sci.* **1996,** *6*, 15-50.

(167)   Kresse, G.; Furthmüller, J. Efficient iterative schemes for ab initio total-energy calculations using a plane-wave basis set. *Phys. Rev. B* **1996,** *54*, 11169.

(168)   Kresse, G.; Joubert, D. From ultrasoft pseudopotentials to the projector augmented-wave method. *Phys. Rev. B* **1999,** *59*, 1758.

(169)   Blöchl, P. E. Projector augmented-wave method. *Phys. Rev. B* **1994,** *50*, 17953.

(170)   Perdew, J. P.; Burke, K.; Ernzerhof, M. Generalized gradient approximation made simple. *Phys. Rev. Lett.* **1996,** *77*, 3865.

(171)   Perdew, J. P. Density-functional approximation for the correlation energy of the inhomogeneous electron gas. *Phys. Rev. B* **1986,** *33*, 8822.

(172)   Krukau, A. V.; Vydrov, O. A.; Izmaylov, A. F.; Scuseria, G. E. Influence of the exchange screening parameter on the performance of screened hybrid functionals. *J. Chem. Phys.* **2006,** *125*, 224106.

(173)   Heyd, J.; Scuseria, G. E.; Ernzerhof, M. Hybrid functionals based on a screened Coulomb potential. *J. Chem. Phys.* **2003,** *118*, 8207-8215.

(174)   Monkhorst, H. J.; Pack, J. D. Special points for Brillouin-zone integrations. *Phys. Rev. B* **1976,** *13*, 5188.

(175)   Paier, J.; Marsman, M.; Hummer, K.; Kresse, G.; Gerber, I. C.; Ángyán, J. G. Screened hybrid density functionals applied to solids. *J. Chem. Phys.* **2006,** *124*, 154709.

(176)   Wang, V.; Xu, N.; Liu, J.-C.; Tang, G.; Geng, W.-T. VASPKIT: A user-friendly interface facilitating high-throughput computing and analysis using VASP code. *Comput. Phys. Commun.* **2021,** *267*, 108033.

(177)   Lu, T.; Chen, F. Multiwfn: a multifunctional wavefunction analyzer. *J. Comput. Chem.* **2012,** *33*, 580-592.

(178)   Francis, G.; Payne, M. Finite basis set corrections to total energy pseudopotential calculations. *J. Phys.: Condens. Matter* **1990,** *2*, 4395.

(179)   Methfessel, M.; Paxton, A. High-precision sampling for Brillouin-zone integration in metals. *Phys. Rev. B* **1989,** *40*, 3616.

(180)   Grimme, S.; Ehrlich, S.; Goerigk, L. Effect of the damping function in dispersion corrected density functional theory. *J. Comput. Chem.* **2011,** *32*, 1456-1465.

(181)   Mills, G.; Jónsson, H.; Schenter, G. K. Reversible work transition state theory: application to dissociative adsorption of hydrogen. *Surf. Sci.* **1995,** *324*, 305-337.

(182)   Henkelman, G.; Uberuaga, B. P.; Jónsson, H. A climbing image nudged elastic band method for finding saddle points and minimum energy paths. *J. Chem. Phys.* **2000,** *113*, 9901-9904.

(183)   Henkelman, G.; Jónsson, H. A dimer method for finding saddle points on high dimensional potential surfaces using only first derivatives. *J. Chem. Phys.* **1999,** *111*, 7010-7022.

Curriculum Vitae

Personal data:

Name:	Shikun Li
Born:	12.12.1992 in Shandong (China)
Address:	Institute of Applied and Physical Chemistry, University of Bremen, Leobener Str. UFT, 28359 Bremen, Germany
Email:	shikunli@hotmail.com

Education:

2017-2023	**PhD (Chemistry)**, University of Bremen, Germany PhD thesis under the supervision of Prof. Dr. Marcus Bäumer and Dr. Lyudmila V. Moskaleva
2014-2017	**Master of Engineering (Industrial Catalysis)**, Dalian University of Technology, China Master thesis in the group of Prof. Dr. Weiping Zhang
2010-2014	**Bachelor of Engineering (Chemical Engineering and Technology)**, Liaocheng University, China

Research Interests:

Density functional theory, Rare earth oxides catalysis, Gold catalysis, Methane activation, Oxygen dissociation

Publications:

- Shikun Li, Okikiola Olaniyan, Lenard L. Carroll, Marcus Bäumer, Lyudmila V. Moskaleva. Catalytic Activity of 1D Chains of Gold Oxide on a Stepped Gold Surface from Density Functional Theory. *Phys. Chem. Chem. Phys*. **2022**, 24, 28853-28863.

- Shikun Li, Yong Li, Marcus Bäumer, Lyudmila V. Moskaleva, Assessment of PBE+ U and HSE06 Methods and Determination of Optimal Parameter U for the Structural and Energetic Properties of Rare Earth Oxides. *J. Chem. Phys*. **2020**, 153, 164710.

- Shikun Li, Zhenchao Zhao, Rongrong Zhao, Danhong Zhou, Weiping Zhang, Aluminum Location and Acid Strength in an Aluminum-Rich Beta Zeolite Catalyst: A Combined Density Functional Theory and Solid-State NMR Study, *ChemCatChem*, **2017**, 9(8), 1494-1502.

- Rongrong Zhao, Shikun Li, Lixin Bi, Qiang Fu, Hong-Zi Tan, Ming Wang, Hongyou Cui, Enhancement of p-Xylene Selectivity in the Reaction between 2,5-Dimethylfuran and Ethanol over Ammonium Fluoride Modified ZSM-5 Zeolite. *Catal. Sci. Technol*., **2022**, 12, 2248-2256.

- Jiexin Zhu, Shikun Li, Zechao Zhuang, Shan Gao, Xufeng Hong, Xuelei Pan, Ruohan Yu, Liang Zhou, Lyudmila V. Moskaleva, and Liqiang Mai, Ultrathin Metal Silicate Hydroxide Nanosheets with Moderate Metal–Oxygen Covalency Enables Efficient Oxygen Evolution. *Energy Environ. Mater*., **2022**, 5, 231-237.

- Yong Li, Shikun Li, Marcus Bäumer, Lyudmila V. Moskaleva, Transient Au–CO Complexes Promote the Activity of an Inverse Ceria/Gold Catalyst: An Insight from Ab Initio Molecular Dynamics. *J. Phys. Chem. C*, **2021**, 125(48), 26406-26417.

- Shihan Li, Zhenchao Zhao, Shikun Li, Youdong Xing, Weiping Zhang, Aluminum Distribution and Bronsted Acidity of Al-Rich SSZ-13 Zeolite: A

Combined DFT Calculation and Solid-State NMR Study. *Acta Physico-Chimica Sinica,* **2020**, 36(4), 1903021

- Yong Li, <u>Shikun Li</u>, Marcus Bäumer, Elena A. Ivanova-Shor, and Lyudmila V. Moskaleva, What Changes on the Inverse Catalyst? Insights from Co Oxidation on Au-Supported Ceria Nanoparticles using Ab Initio Molecular Dynamics. *ACS Catal.*, **2020**, 10, 3164-74.

- Zhiquan Lang, Zechao Zhuang, <u>Shikun Li</u>, Lixue Xia, Yan Zhao, Yunlong Zhao, Chunhua Han, and Liang Zhou, Mxene Surface Terminations Enable Strong Metal–Support Interactions for Efficient Methanol Oxidation on Palladium. *ACS Appl. Mater. Interfaces*, **2020**, 12, 2400-06.

- Min Wang, Zhuqing Wang, Xiaohong Zhou, <u>Shikun Li</u>, Efficient Removal of Heavy Metal Ions in Wastewater by Using a Novel Alginate-EDTA Hybrid Aerogel, *Appl. Sci.*, **2019**, 9(3), 547.

- Rongrong Zhao, Zhenchao Zhao, <u>Shikun Li</u>, Andrei-Nicolae Parvulescu, Ulrich Müller, and Weiping Zhang, Excellent Performances of Dealuminated H-Beta Zeolites from Organotemplate-Free Synthesis in Conversion of Biomass-Derived 2,5-Dimethylfuran to Renewable P-Xylene. *ChemSusChem*, **2018**, 11, 3803-11.

- Laxman Kankate, Thorben Hamann, <u>Shikun Li</u>, Lyudmila V. Moskaleva, Armin Gölzhäuser, Andrey Turchanin, Petra Swiderek, Tracking Down the Origin of Peculiar Vibrational Spectra of Aromatic Self-Assembled Thiolate Monolayers, *Phys. Chem. Chem. Phys.*, **2018**, 20(47), 29918-29930.

- Rongrong Zhao, Zhenchao Zhao, <u>Shikun Li</u>, Weiping Zhang, Insights into the Correlation of Aluminum Distribution and Brönsted Acidity in H-Beta Zeolites from Solid-State NMR Spectroscopy and DFT Calculations, *J. Phys. Chem. Lett.*, **2017**, 2323-2327.

Presentations:

|	
September 2019	**BIG DATA SUMMER-A summer school of the BiGmax Network**, Platja d'Aro, Spain, poster presentation
February 2019	**CECAM Workshop - Correlated electron physics beyond the Hubbard-model**, Bremen, Germany, poster presentation
June 2018	**16th International Congress of Quantum Chemistry**, Menton, France, poster presentation
August 2016	**19th Chinese National Conference on Spectroscopy**, Lanzhou, China, poster presentation
July 2016	**16th International Congress on Catalysis**, Beijing, China, poster presentation

Publication I

Assessment of PBE+U and HSE06 methods and determination of optimal parameter U

for the structural and energetic properties of rare earth oxides

Shikun Li, Yong Li, Marcus Bäumer, Lyudmila V. Moskaleva

J. Chem. Phys. **2020**, 153, 164710
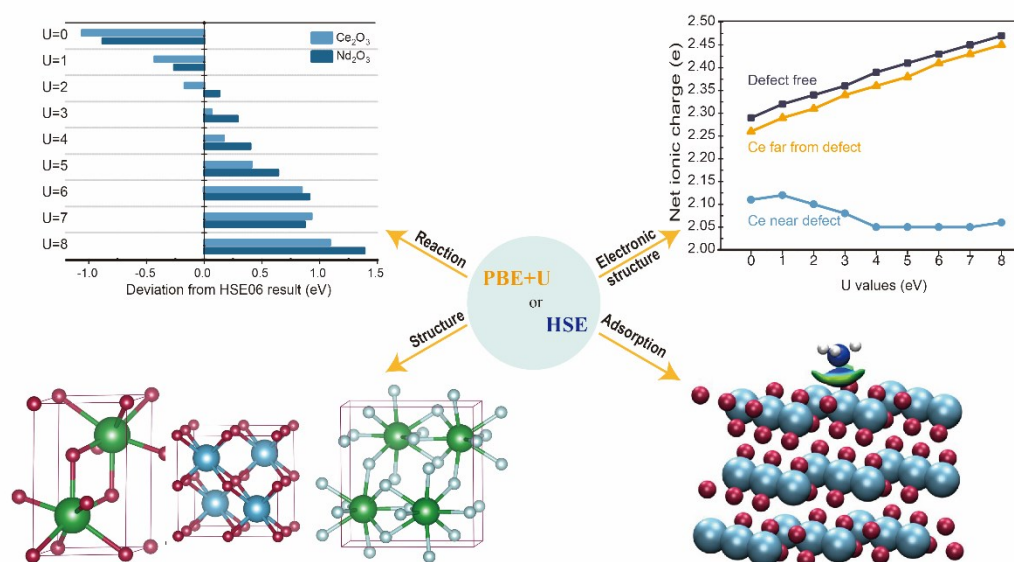
The pdf-document of this publication is not embedded for copyright reasons.
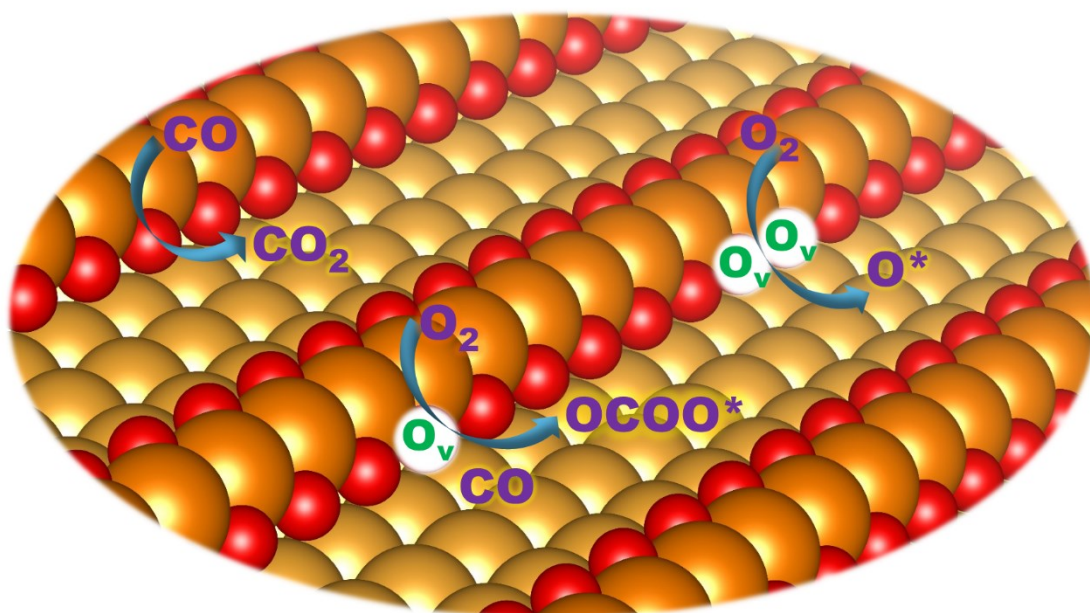
The publication can be accessed via the link:

Publication II

Catalytic activity of 1D chains of gold oxide on a stepped gold surface from density functional theory

Shikun Li, Okikiola Olaniyan, Lenard L. Carroll, Marcus Bäumer, Lyudmila V. Moskaleva

The pdf-document of this publication is not embedded for copyright reasons.

The publication can be accessed via the link:

Publication III

The impact of electronic structure modification on Lewis acidity-basicity and reducibility of doped La_2O_3

Shikun Li, Marcus Bäumer, Lyudmila V. Moskaleva

In preparation